INVESTIGATION OF CRITICAL ISSUES

IN THERMAL BARRIER COATING DURABILITY

DISSERTATION

Presented in Partial Fulfillment of the Requirements for

the Degree Doctor of Philosophy in the Graduate

School of The Ohio State University

By

Hyungjun Kim, M.S.

* * * * *

The Ohio State University
2005

Approved by

Dissertation Committee:

Professor M.E. Walter, Adviser

Professor A. Gilat

Professor B. Harper

_____
Adviser

Department of Mechanical Engineering

ABSTRACT

To more fully understand microstructural evolution and the development of damage in thermal barrier coating (TBC) systems, thermocyclic experiments were conducted on TBC specimens with and without top coats. The degradation of a PtAl (platinum modified aluminide) bond coat and a CMSX superalloy substrate were investigated for cyclic and quasi-isothermal heating to 1200 ºC. To accelerate the oxidation of the specimens, the thermally grown oxide (TGO) was removed at 10 hour intervals. Scanning electron microscopy (SEM) and instrumented indentation were employed to investigate microstructural evolution and material property changes of the bond coat. The microstructural evolution of a PtAl bond coat is strongly affected by the type of thermal exposure and the presence of TGO. The differences between cyclic and quasi-isothermal heating indicate that stresses associated with cooling and heating significantly alter microstructural evolution.

Damage to TBC specimens with EB-PVD (electron beam physical vapor deposition) processed YSZ (yttria stabilized zirconia) top coats, PtAl bond coats, and René N5 superalloy substrates was assessed during thermal cycling to 1200 °C. Acoustic emission (AE) techniques were used to temporally identify damage to the TBC. For automated, continuous, and high temperature AE detection, a custom made experimental setup with either a nickel-chrome alloy wire wave guide or an alumina wave guide was

used. It was found that there are four distinct regions of AE activity during the life of a TBC. Throughout the cooling cycles, images of the top coat were collected with darkfield-type lighting. These images showed how undulations developed in the top coat. In addition, digital image correlation (DIC) was used to identify regions with interfacial damage. Finally, the images were used to analyze the spallation of the top coat. Cycling of an additional specimen was interrupted periodically for analysis with profilometry and SEM. The profilometry and SEM images were used to further investigate the failure mechanisms in TBCs.

The experiments and analysis performed in this dissertation work have elucidated how various failure mechanisms develop during the life of TBCs. This work has improved the scientific understanding of TBCs and could aid in the development of improved life prediction models.

DEDICATION

Dedicated to my parents
for their love and support throughout my life

ACKNOWLEDGMENTS

I would like to express my sincere gratitude to my adviser, Dr. Mark Walter for his support, patience, and enthusiasm that made this work possible. I would like to thank Dr. June Kee Lee for his generosity and guidance. I would also like to acknowledge Dr. Jong-Tae Jinn for his academic and spiritual advice. I would like to give special thanks to Dr. Amos Gilat and Dr. Brain Harper for taking time out to participate on my dissertation committee. I also would like to thank to Howmet and GE for providing specimens. Finally, I would like to thank my family especially my mom and dad whose continuous love and support made it possible for me to study abroad and to finish this dissertation.

VITA

July 3, 1969……Born - Seoul, Korea

1997……B.S. Mechanical Engineering,
The Ohio State University
Columbus, OH USA

2000……M.S. Mechanical Engineering,
The Ohio State University
Columbus, OH USA

2000 – Present……Graduate Research Associate
The Ohio State University
Columbus, OH USA

JOURNAL PUBLICATIONS

1. H. J. Kim and M. E. Walter, "Characterization of the Degraded Microstructures of a Platinum Aluminide Coating," *Materials Science and Engineering A*, 360(1-2): 7-17, 2003.

2. H. J. Kim, J. S. Kim, M. E. Walter and J. K. Lee, "The Thermo-Mechanical Stress-Strain Response of Intumescent Mat Materials through Experiments and Strain Decomposition," *Journal of Strain Analysis,* 37(3): 187-199, 2002.

FIELDS OF STUDY

Major Fields: Mechanical Engineering, Experimental Mechanics

TABLE OF CONTENTS

LIST OF TABLES

LIST OF FIGURES

CHAPTER 1

INTRODUCTION

1. SIGNIFICANCE OF THE PROBLEM

Engine failure is one of the most common reasons for commercial and military aircraft accidents. Since a commercial airplane crash usually involves significant financial and human life losses, the impact of one commercial airplane crash on society is overwhelming. The National Transportation Safety Board's former chairman Jim Hall estimated that the direct cost of one fatal commercial aviation accident totals more than $300 million [1]. Naturally, the Chairman was also concerned about the enormity of the human tragedy involved. In the military, there is serious concern over aging aircraft that have higher chances of fatal crashes and astronomical maintenance costs. A recent report said that 45% of the airlift/tanker/trainer engine fleet is over 30 years old and 54% of the fighter engine fleet is 21 to 30 years old. Innovative engine failure prevention/prediction

techniques are needed to stem the soaring costs associated with engine failure and maintenance.

Aircraft turbine engines fail at blades, vanes, disks, ducts, gearboxes, stationary structures, bearings, *etc*. Since the failure of only one blade on an engine with 200 to 400 blades could be catastrophic, blade failure is one of the leading cause of engine related aircraft accidents [1]. Aircraft turbine engines use superalloy blades that are designed for high temperature applications. Good mechanical and thermal properties as well as resistance to environmental attack are base requirements for these superalloys. Higher turbine inlet temperature is an overarching goal of turbine engine design since higher turbine inlet temperature improves aircraft engine thrust and fuel efficiency. To protect superalloy components from high temperature and corrosive combustion gases (*e.g.,* sulfur), thermal barrier coatings (TBCs) have been used since the mid-1970s. The use of TBCs lowers the temperatures seen by the superalloy substrate by up to 170 °C [2].

Application of TBCs can be an expensive endeavor. However, the added expense is offset by the increased performance of the engine and/or lower maintenance costs. A more significant trade-off for using TBCs for corrosion and high temperature

protection is the introduction of a coating whose durability is not predictable. In other words, the TBCs are not "prime reliant." The worst-case scenario for durability loss is spallation of the TBC, which exposes the superalloy to higher temperatures and to aggressive combustion gases. This event accelerates the degradation of the superalloy and may cause structural failure. To prevent catastrophic engine failure and to reduce maintenance costs, comprehensive research into the mechanisms associated with TBC durability loss must be performed.

2. LITERATURE REVIEW

2.1 TBC SYSTEMS AND ROLE OF EACH LAYER

State of the art TBC systems consist of a top coat, thermally grown oxide (TGO), bond coat, and substrate. These different layers form a "system." The substrate is included in the system because it is an integral part of the coating, and it is not possible to reproduce the coating without the substrate. Although authors often use the term "TBC" to refer only to the top coat, in this dissertation TBC is used to refer to the complete system. The top coat is a thermally insulating, strain tolerant oxide. Under the insulative ceramic top coat there is a bond coat that forms an oxidation/environmental

barrier. A TGO layer is put between the top coat and bond coat. The TGO layer grows during service.

Figure 1.1 shows a scanning electron microscopy (SEM) cross-section of a TBC specimen used in this research. This particular specimen has a 3 mm thick René N5 nickel base superalloy substrate. The ceramic top coat, which is around 120 μm thick, has a columnar structure. The TGO layer typically grows to a thickness of around 6-7 μm by the end of life [3, 4]. The bond coat has a thickness of 50 μm. These specimens were provided by General Electric Aircraft Engines (www.geae.com).

Low thermal conductivity and strain tolerance are two major requirements for the ceramic top coat. Strain tolerance is important to avoid vertical cracks that would then propagate along the interface and cause instantaneous delamination. Two processes have been used to deposit strain tolerant ceramic top coats. Air plasma sprayed (APS) deposition was first introduced, and during the 1990s the physical vapor deposition (PVD) process was successfully brought into commercial service [5]. APS deposition which has a lower cost than PVD generates porosity and a network of crack-like voids to provide some strain tolerance [6]. The unique columnar grain structure and porosity containing ceramic top coats produced by PVD processes such as sputtering give better

strain tolerance [7]. Higher deposition rates are achieved by electron beam physical vapor deposition (EB-PVD), which provides up to 7 μm/min deposition rates on blades [8]. The economics and the better strain tolerance make EB-PVD the process of choice for TBCs on blades. TBCs for larger structures such as combustor liners and rocket nozzles are typically produced with thermal spray technology.

Yttria stabilized zirconia (YSZ or ZrO_2 with 7% Y_2O_3), which has low thermal conductivity (~1 W/m^2K) with minimum temperature sensitivity is a preferred material for the top coat. Yttria stabilizes zirconia into cubic and tetragonal forms [6]. YSZ has a relatively high coefficient of thermal expansion (CTE), phase stability to 1400 °C, and good corrosion resistance. Through the resulting columnar grain structure and porosity, EB-PVD processing lowers the thermal conductivity of the YSZ top coat to 0.5 W/m^2K [6].

While APS deposited ceramic top coats adhere to the bond coat primarily through mechanical interlocking from semi-plastic particle deformation, PVD coatings have chemical bonding adhesion mechanisms [9]. During the deposition process, TGO grows between the top coat and bond coat. In the as-deposited state, the TGO is around

0.5 μm thick [3]. Since the ceramic top coat is transparent to oxygen, TGO continues to grow during subsequent high temperature exposure.

Due to its low oxygen diffusivity, structural stability, density, and superior adherence [6], α-alumina (α-Al_2O_3) is the preferred TGO. Oxygen passes through the ceramic top coat and combines with aluminum that diffuses from the bond coat to form additional TGO during service. The TGO layer acts as the source of chemical bonding between the top coat and bond coat. By greatly retarding the oxygen transport rate, the TGO layer also reduces the rate of bond coat oxidation [10, 11]. Thus this TGO layer also protects the *substrate* from high temperature corrosion and oxidation.

The bond coat is designed as a bonding layer and a local aluminum reservoir. The bond coat is crucial because its chemistry and microstructure influence the TGO layer. Because of its stable and slow growing TGO, platinum modified aluminide (PtAl) coatings are one of the most popular types of bond coats for TBC systems. PtAl is typically fabricated by electroplating a thin layer of Pt onto the substrate and then aluminizing by pack cementation [6]. The pack cementation is an *in situ* chemical vapor deposition process and is used to apply high temperature oxidation and corrosion protective coatings on metal surfaces [12]. Pt additions were initially intended to prevent

or retard inter-diffusion of aluminum from the bond coating into the substrate [13]. However, the complete role of Pt has not been fully established.

Embrittlement between the TGO and bond coat interface can be caused by sulfur diffusing from the substrate and from combustion gases during thermal exposure. It is important for bond coats to control sulfur mobility. Another type of bond coat, NiCoCrAlY has yttria as a getter element for sulfur. The PtAl bond coat does not contain any getter element for sulfur [6]. Monceau *et al*. [14] have experimentally investigated several bond coat systems including PtAl and NiCoCrAlY with different surface treatments and under different thermal conditions, and it was found that the PtAl bond coat resulted in the best TGO adherence and longest life.

2.2 TBC DURABILITY LOSS ISSUES

During turbine engine operation, TBCs experience large numbers of high temperature thermal cycles that lead to TBC failure. Stiger *et al.* [15] categorized four leading causes for TBC failure: ceramic top coat cracking, sintering of zirconia, particle erosion, and TGO interface cracking. Horizontal and vertical cracks in the ceramic top coat are a major source of TBC failure, and sintering of zirconia is one of the reasons for top coat cracks. Particle erosion is another significant cause of TBC failure [16].

Foreign object damage that is caused by particle impact is one example of particle erosion. Foreign object damage leaves the top coat locally compressed and results in a hot spot in the bond coat [6, 17]. This damage contributes to TBC failure. Propagation of cracks within the TGO interface is blamed for most TBC failure in EB-PVD and APS processed TBCs [2]. TGO interface cracking causes spallation or macroscopic failure of TBCs. These TGO interface cracks have been investigated intensively [4, 15, 18-20]. The TGO interface cracking location (*i.e.,* between the top coat and the TGO layer versus between the TGO layer and the bond coat) depends on the top coat deposition process and the type of bond coat [21]. In APS deposited top coats, cracking occurs at the top coat - TGO interface [22]. In EB-PVD TBCs, cracking usually occurs at the bond coat - TGO interface with NiCoCrAlY bond coats [23] and at the top coat - TGO interface with PtAl bond coats [3].

Regardless of the cracking location, TGO interface cracking is the result of the combined effect of various stress generation and microstructural degradation factors. Stresses generated on the TGO interface are affected by TBC degradation such as phase change in the bond coat [24-26], TGO growth [4, 27-29], and sintering of the top coat [30]. Gell *et al.* [22] said there are dozens of materials and processing variables that must

be controlled to provide TBCs with long-term durability. Failure mechanisms in TBCs are very complex and are not completely described by simple models.

Gell *et al.* [22] tried to sum up all failure parameters and focused on two TBC system variables to explain TBC failure: the bond stress and bond strength in the vicinity of the TGO. The bond stress is the out-of-plane (normal to the interface) tensile stress on the TGO interface. Gell *et al.* [22] explained that as thermal cycling progresses, the bond strength decreases and the bond stress increases. From this point of view, TBC degradation can be regarded as an evolutionary process that decreases the bond strength and simultaneously increases the bond stress.

2.3 TBC DEGRADATION

It is ironic that the TGO layer provides adhesion between the top coat and bond coat, protects the bond coat/substrate from high temperature corrosion and oxidation, and at the same time, growth of the TGO layer and its interfaces is blamed for TBC failure. TGO degradation plays an integral role in the ultimate failure of the TBC system. The TGO quality is significantly degraded by the diffusion of hafnium from the substrate [31] and the presence of sulfur in the coating or the substrate [14], and this TGO degradation leads to bond strength decrease. Since there is mechanical and chemical

interaction between the TGO and the bond coat, it is essential to study TGO degradation together with bond coat degradation. In earlier work, thermo-mechanical cycling of an aluminide coating on a superalloy was investigated and the formation of oxide, onset of oxide scalloping, and fracture of the coating was studied [32]. For evaluating the quality of the oxide scale formation, the microstructure of different bond coat systems was described in detail [14, 31].

The formation of interfacial waviness is the most critical bond coat issue related to the TGO layer. TGO waviness has been associated with initial processing defects [23] and the undulation amplitude of the TGO may be increasing through plastic ratcheting of the bond coat [33]. Phase changes from β-(Ni,Pt)Al to γ'-(Ni_3Al) are thought to cause resistance to downward displacement of the TGO [3] because phase changes result in a volume reduction. Phase changes may also enhance waviness [20]. Transformation of β-(Ni,Pt)Al phase to γ'-(Ni_3Al) phase is presumed to be driven by depletion of aluminum [13].

More recently, martensitic transformation of bond coat microstructure has received significant attention [24-26, 34]. While the transformation from martensite to β-(Ni,Pt)Al during heating cycles accompanies the volume expansion of the bond coat, the

transformation from β-(Ni,Pt)Al to martensite during cooling cycles accompanies the volume shrinkage of the bond coat [34]. Therefore, the bond coat martensitic phase transformation plays an important role in the stress and strain formation in TBCs by enhancing the CTE misfit strains during thermal cycling [34]. The bond coat martensitic transformation along with CTE misfit may thus promote TGO waviness growth [35].

Grain boundary ridges are another critical bond coat issue related to the TGO layer [21]. It has been found that voids under the TGO begin with ridges associated with bond coat grain boundaries [36]. Preferential oxidation along the near-surface bond coat grain boundaries occurs because TGO integrity is diminished near grain boundary ridges. It has been reported that when ridges on the PtAl bond coat layer were removed, spallation life increased by three times [22]. The oxidized grain boundaries cause cyclic plasticity in the bond coat and void growth during thermal cycling. More recently it has been postulated that pre-existing grain boundary ridges play an important role in initiating and widening the top coat vertical cracks as the TGO layer thickens [37].

Sintering of zirconia is one of the most critical top coat degradation mechanisms. Since the in-plane Young's modulus of the YSZ is dependent on the degree of contact between each column, sintering of zirconia increases the in-plane modulus

[38]. The increase in the modulus results in an increase in residual stress and the strain tolerance of the top coat decreases [30]. Sintering of zirconia also increases thermal conductivity significantly [39]. Leyens *et al.* [38] reported that sintering effects were observed for all different YSZ microstructures after 100 one hour cycles at 1150 °C. Sintering also is observed in 1100 °C cycles, but compared to 1150 °C cycles, it is less significant even after 1000 cycles and is more YSZ microstructure dependent [38]. It was also reported that extensive sintering had occurred after only 50 hours of 1200 °C isothermal heating [40, 41].

2.4 CRACKING, BOND STRESSES, AND SPALLATION

A fracture mechanics orientated and TGO interface cracking based TBC failure model has been suggested by Evans and co-workers [3, 23, 42]. Figure 1.2 shows the TGO interface failure model by Mumm *et al.* [3, 42]. In the first step, initial imperfections are sites for displacement instabilities. TGO undulation or rumpling causes stress concentrations and sub-critical interface cracks nucleate in the YSZ top coat. The sizes of the sub-critical interface cracks which form during the first 34% of cyclic life are about 10-50 μm long [6]. The bond coat evolution due to inward and outward diffusion plays an important role in TGO waviness. Downward displacement of the TGO induces

tensile stresses and sub-critical interface cracks nucleate in the top coat due to Mode I fracture loading [43]. Out-of-plane tensile stresses around initial imperfections with downward TGO displacement are closely related to in-plane (parallel to the interface) compressive stresses in the TGO layer. Undulations and sub-critical interface cracks continue to grow and coalesce [23, 44]. Crack extension to around 100 μm long happens by around 76% of the cyclic life [6]. These 10-100 μm cracks are called short cracks, and their formation is governed by mode I fracture toughness [6]. Mode I fracture toughness of the YSZ top coat is in the range from 0.1 to 1 $MPa \cdot m^{1/2}$ [6]. Just outside of the TGO downward displacement region, the TGO is displaced upward and compressive stresses occur in the top coat. This region is governed by Mode II fracture loading [43].

Compared to the short cracks, long cracks with lengths greater than 1 mm are governed by mode II fracture toughness. These cracks are usually observed emanating from free edges [6]. Mode II fracture toughness of the YSZ top coat ranges from 3 to 5 $MPa \cdot m^{1/2}$ [6].

Under sufficiently high thermal gradients, YSZ top coat cracks can form and propagate either parallel or vertical to the TGO interface [45, 46]. These types of cracks were observed in specimens under thermal shock produced by high energy laser heating

[46]. No EB-PVD YSZ top coat crack induced failures were observed in specimens within a furnace or a burner rig [45]. Hutchinson *et al.* [45] categorized YSZ top coat cracks into "isolated cracks" and "shrinkage cracks" [45]. Isolated cracks, which are parallel to the TGO interface, are due to thermal gradients. Shrinkage cracks which are vertical to the TGO interface are generated because of deficit strains caused by sintering of the zirconia columnar structure [46].

In the presence of in-plane compressive stresses on the TGO layer, the waviness of the TGO layer with downward TGO displacement generates the out-of-plane tensile stresses on the TGO interface. PtAl bond coat phase change due to inter-diffusion is blamed for rumpling which significantly increases the bond stresses [20, 33]. The TGO layer in-plane compressive stresses are caused mainly by CTE misfit and TGO swelling [6]. The CTE of the substrate and TGO varies from 14.8 to 18.0 $\times 10^{-6}$/°C and from 8.0 to 9.6 $\times 10^{-6}$/°C at 20 °C and 1100 °C, respectively [47]. Therefore, the TGO layer develops large, in-plane compressive stresses (3-6 GPa) as the TBC cools to ambient temperature [18]. TGO formation is a volumetric expansion process that also generates in-plane compressive stresses in the TGO layer [48]. However, it is believed that smaller stresses (less than 1 GPa) are arise from TGO formation [6].

Sub-critical interface cracks are the intermediate step towards TBC failure, and spallation is the final step in TBC failure. TBC spallation results from buckling of the ceramic top coat [48]. When the ceramic top coat becomes sufficiently debonded by the interface cracks, buckling is caused by in-plane compressive stresses on the ceramic top coat which are due to CTE misfits between the top coat and substrate. Sintering of zirconia increases the in-plane compressive stresses on the top coat [30].

Observations indicate that TBC spallation is a buckling phenomenon [48]. Figure 1.3 shows a TBC specimen with a buckled top coat. It has been reported that buckling of the ceramic top is possible when the interface crack size is at least 16 times the ceramic top thickness [49]. Therefore, for the current specimens, when the interface crack becomes more than 1.5 mm, spallation of the top coat could occur.

2.5 TBC LIFE PREDICTION

Existing TBC life prediction models are primarily empirically based and are driven by fitting model parameters to data generated under burner-rig tests [50]. The earliest life prediction modeling work tried to correlate the spallation life with exposure time, temperature, and number of cycles [51]. Meier *et al*. [52] suggested a life prediction model based on maximum in-plane TGO layer tensile strain and TGO

formation for both EB-PVD and APS TBCs. However, this model seems to be flawed since the TGO layer is always under compressive strain. Chan *et al*. [53] developed a life prediction model for EB-PVD TBCs based on coating degradation mechanisms including oxidation, spallation, and aluminum depletion in the bond coat.

Since there are so many factors which influence the life of TBCs, it is not an easy task to predict TBC failure. For example, the maximum temperature is a critical factor for TBC life. Yanar *et al.* [54] showed that TBC failure for 45 minute cyclic heating at 1100 °C and 1200 °C will occur after 1200 cycles and 120 cycles, respectively. Therefore, the life prediction model should be sensitive enough to predict TBC failure for different maximum temperatures. Naturally, the cycle time will also play a major role in the time to failure.

Another obstacle for accurate life prediction is the scatter of TBC life even among identically processed specimens. It seems that this variability comes from initial processing defects and microstructural variability. The YSZ top coat has inherent randomly distributed flaws. The observed scatter in fracture strength may be caused by the severity and location of these flaws [55]. Another example of this variability is provided by Gell and co-workers [22]. They observed that for one hour cycles to 1121

°C, EB-PVD YSZ top coat PtAl bond coat specimens survived anywhere from 200 to 1900 cycles [22].

3. SCOPE AND OBJECTIVE OF THE RESEARCH

As explained above, because of different deposition processes, materials, and service scenarios, there are several types of TBC failure mechanisms. In this research, only TBC systems with EB-PVD processed YSZ top coats and PtAl bond coats processed by pack cementation will be studied.

Since microstructural degradation affects the bond strength and the bond stress, analyzing the TBC degradation quantitatively as well as qualitatively will be beneficial to better understanding of TBC failure mechanisms. The first part of this work will concern itself with microstructural evolution of the PtAl bond coat under high temperature thermal loading. Phase transformation of the bond coat will be the focus in this study. Effects of thermal cycling and (quasi)-isothermal holding on bond coat microstructural evolution will be investigated with extensive SEM.

Phase changes of the bond coat will alter the mechanical properties of the bond coat. Phase changes can be analyzed by measuring the elastic modulus changes of the bond coat. Since instrumented indentation can be used to probe elastic properties [56,

57] and needs only small volumes of material, the instrumented indentation technique can be used for measuring bond coat elastic modulus. Bond coat evolution will be quantitatively analyzed by measuring elastic modulus change of the bond coat with instrumented indentation.

If it is known how much damage a TBC can sustain, by tracking damage formation and growth, the remaining life can be predicted. Top coat cracking, sub-critical interface crack nucleation/propagation/coalescence, and spallation by buckling are the basic damage mechanisms in TBCs. Therefore, the detection of sub-critical interface cracks, which eventually link together to create macroscopic spallation [23], is crucial information for TBC failure and life prediction modeling.

In the case of sub-critical crack based TBC modeling, the difficulty comes from detecting the actual cracks. At 34% of the cyclic life the size of short cracks is only around 10-50 μm [6]. The location of these cracks also makes it difficult to detect them. For *in situ* and especially non-destructive crack detection, new methods must be developed.

Internal damage in ceramics has been successfully detected by using infrared thermal images of the ceramic top surface during application of heat to the bottom

surface [58, 59]. This method was applied to TBCs and the results showed that thermal cycling resulted in an average surface temperature drop on the top coat surface due to debonding [60]. A similar method also showed changes in infrared images of the top coat surface as thermal cycles increased [61]. However, most of these tests did not have enough spatial resolution to enable quantitative analysis of sub-critical interface cracks. More importantly, until cracks grow large enough sizes, internal damage could not be identified by these methods. Therefore, detailed cracking information especially during earlier stage of TBC life is not available from these methods.

Acoustic emission (AE) is a name for mechanical waves produced by rapid strain energy release [62]. AE is produced by various types of microstructural changes and is commonly used to monitor crack formation. Therefore, it is expected that AE can be used to detect damage accumulation in TBCs. Generally, phase transformation [63], crack formation [64], and crack propagation [64] produce AE. AE techniques have been used to detect damage in TBC specimens during indentation and scratching [65], top coat cracking under four point bending loading [66], and other cracking activities in TBC specimens [67, 68]. AE techniques have also been applied to monitored thermal fatigue failure of TBC specimens [69].

AE which originates from TBC damage formation will be detected and analyzed during the second phase of this research. Based primarily on the rate of accumulation of events, distinct regions in which different damage mechanisms are active will be identified. In this way, TBC degradation through damage accumulation under high temperature thermal cycling will be traced throughout the TBC life.

When a thin coating is bonded to a substrate and has residual stresses, the substrate develops curvature to compensate for the coating stresses [70]. Measuring the curvature of the coating-substrate system enables calculation of the residual stress stored in the coating [71]. The significant CTE mismatch between the substrate and TGO/top coat places the TGO under compressive stress. Stresses are equilibrated by the development of convex curvature.

A profilometer will be used to measure the curvature change of the TBC at regular intervals. Thus it will be reported how TGO layer stresses evolve during the TBC life. The profilometer will also be used to quantify the change in top coat waviness. For specimens that will be investigated with the profilometer, the TBC top coat will be carefully polished because profilometry requires smooth surfaces.

Intact interface and top coat-TGO separation can generate waviness on the top coat surface [72]. Because of compressive residual stresses on the top coat, intact interfaces will form valleys and separated interface will be form hills on the top coat surface. Therefore, the distribution of valleys and hills on the top coat surface can be related to interface cracking/delamination. By using a charge coupled device (CCD) camera with a microscope, top coat surface images will be taken, and the top coat's change in waviness will be traced during the TBC life.

Top surface images will be used to locate interface delamination and determine top coat thermal contraction behavior using digital image correlation (DIC) calculations. DIC is a method for calculating displacements and displacement gradients by comparing two digital images [73-78]. Since DIC has *in situ* and non-contact capability, DIC can be used to monitor thermal contraction behavior of the TBC specimens during cooling. If delaminations exist, one would expect the thermal contraction to become non-uniform near the delamination. In this way, delamination can be monitored. Top surface images also will be used to study TBC spallation process due to buckling of the top coat. SEM micrographs of the top coat surface will aid to identify the vertical crack formation and will supply additional information regarding top coat damage. For specimens that will be

investigated with SEM, the TBC top coat will be carefully polished to remove pre-existing top coat columnar gaps. By removing top coat pre-existing columnar gaps, vertical cracking will be clearly distinguished. SEM also will be used to investigate he failed interfaces of the spalled TBC specimens.

Through the work outlined above, a better understanding of the TBC failure process will be obtained. With non-destructive techniques, damage mechanisms for each stage of TBC life will be identified. These results have important ramifications for life prediction modeling. The following summarizes the five main areas of investigation in this research:

I. Instrumented indentation
   - Machine compliance correction and calibration of the instrument
   - Elastic modulus measurements

II. Bond coat degradation analysis
   - Microstructural evolution and differences between cyclic and isothermal heating
   - Accelerated aluminum depletion effects on microstructural evolution
   - Elastic modulus estimation of degraded bond coat material
   - Rule of mixture analysis for a multi phase bond coat material

III. Temporal TBC damage assessment during thermal cycling of TBCs

- *In situ* damage detection with AE techniques
- Dividing TBC life into regions with different dominant damage mechanisms

IV. TGO residual stress, top coat roughness, and delamination assessment

- Curvature change measurement with profilometry
- TGO layer stress evolution obtained from curvature measurements
- Top coat surface roughness evolution
- Investigation of the delamination which causes spallation

V. Top coat vertical cracking, delamination propagation, spallation, and DIC

- Top coat vertical cracking analysis by SEM
- Imaging of delamination propagation: the development of spallation
- Post spallation observation
- Interface delamination detection and thermal contraction change of the top coat using DIC

4. EXPECTED CONTRIBUTIONS

Experimental results from this research will advance the scientific understanding of TBC failure. Better understanding of TBC failure will be helpful for designing more durable TBCs to improve engine efficiencies and reduce maintenance costs. Moreover, this research will help to save lives and money by predicting/preventing catastrophic turbine engine failure. The following summarizes the expected contributions

of this research in two areas: TBC degradation information and temporal and spatial damage accumulation analysis.

For bond coat phase transformation analysis, an accelerated aluminum depletion test will be conducted for faster and clearer observation and will provide solid evidence of microstructural evolution by cyclically induced stresses. Phase transformation will be quantified by modulus measurements and SEM micrograph image analysis.

Damage accumulation will be analyzed for both temporal and spatial aspects by applying AE, CCD camera imaging, DIC, profilometry, and SEM techniques. AE techniques will map damage accumulation under high temperature thermal loading throughout the TBC life. Interface crack characterization methods will be developed by CCD camera images and DIC techniques. It will be shown that the DIC calculation provides a non-destructive test method for interface crack detection. The profilometry will be shown to provide a simple way to measure TGO layer residual stresses and to quantify the change in top coat waviness. Polishing enables the use of SEM to detect vertical crack formation. Imaging of delamination propagation by CCD camera images enables detailed analysis of the spallation process.

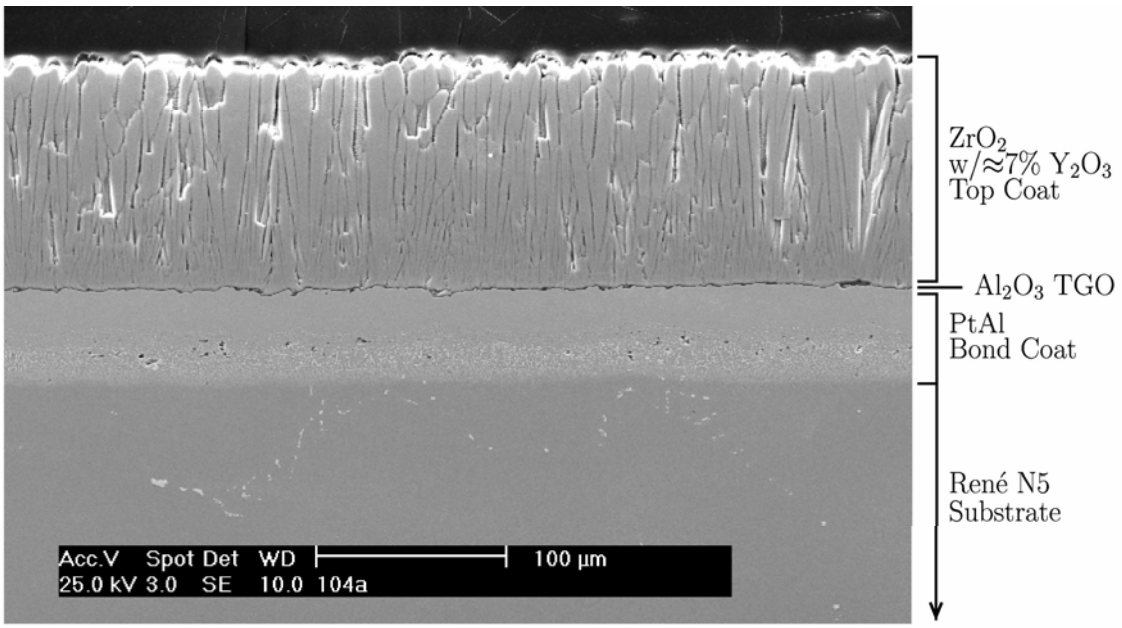

Figure 1.1: The section view of the TBC system used in this research.

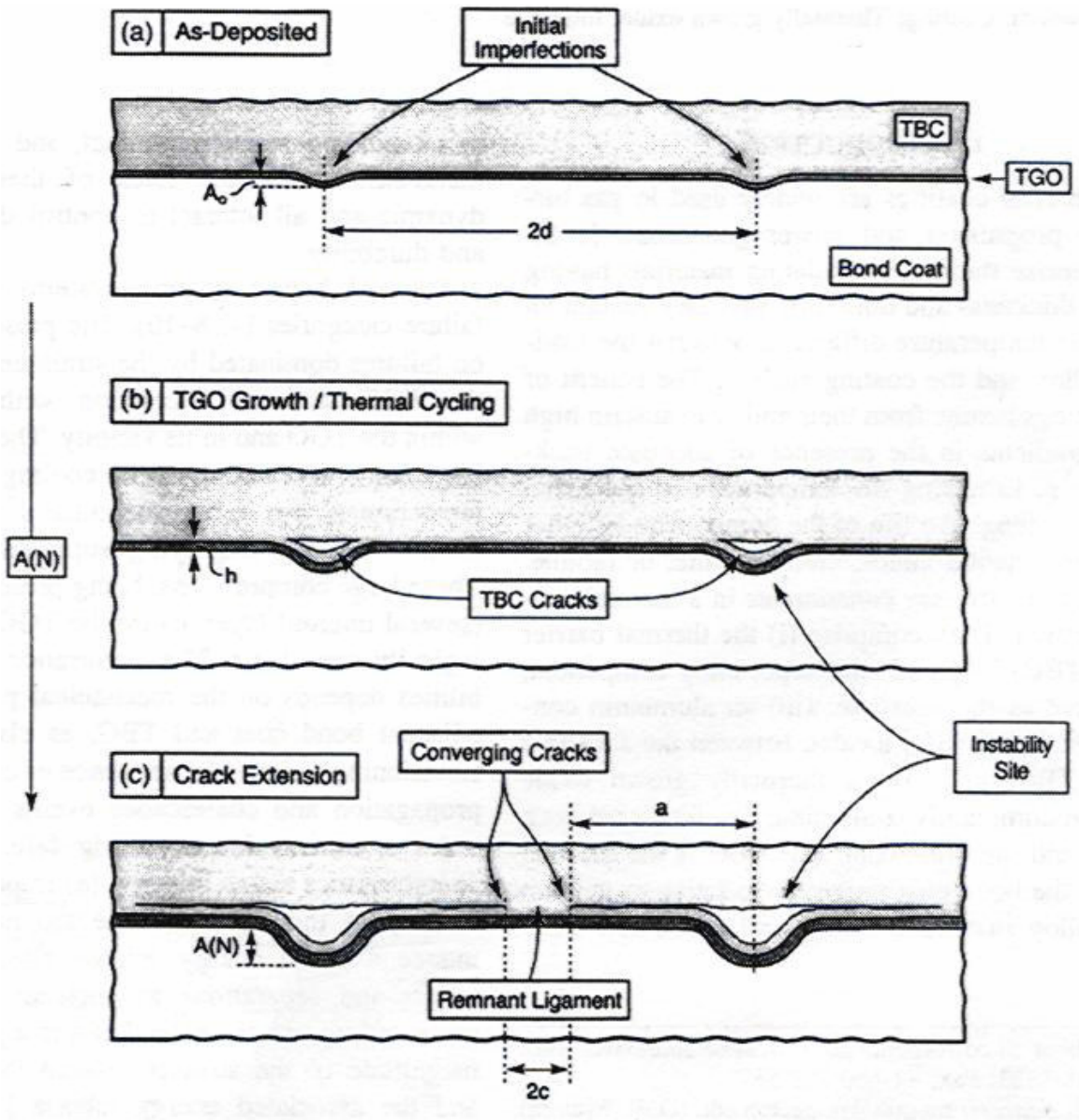

Figure 1.2: Illustration of the three main steps in the Mumm *et al.* [3] TBC failure model.

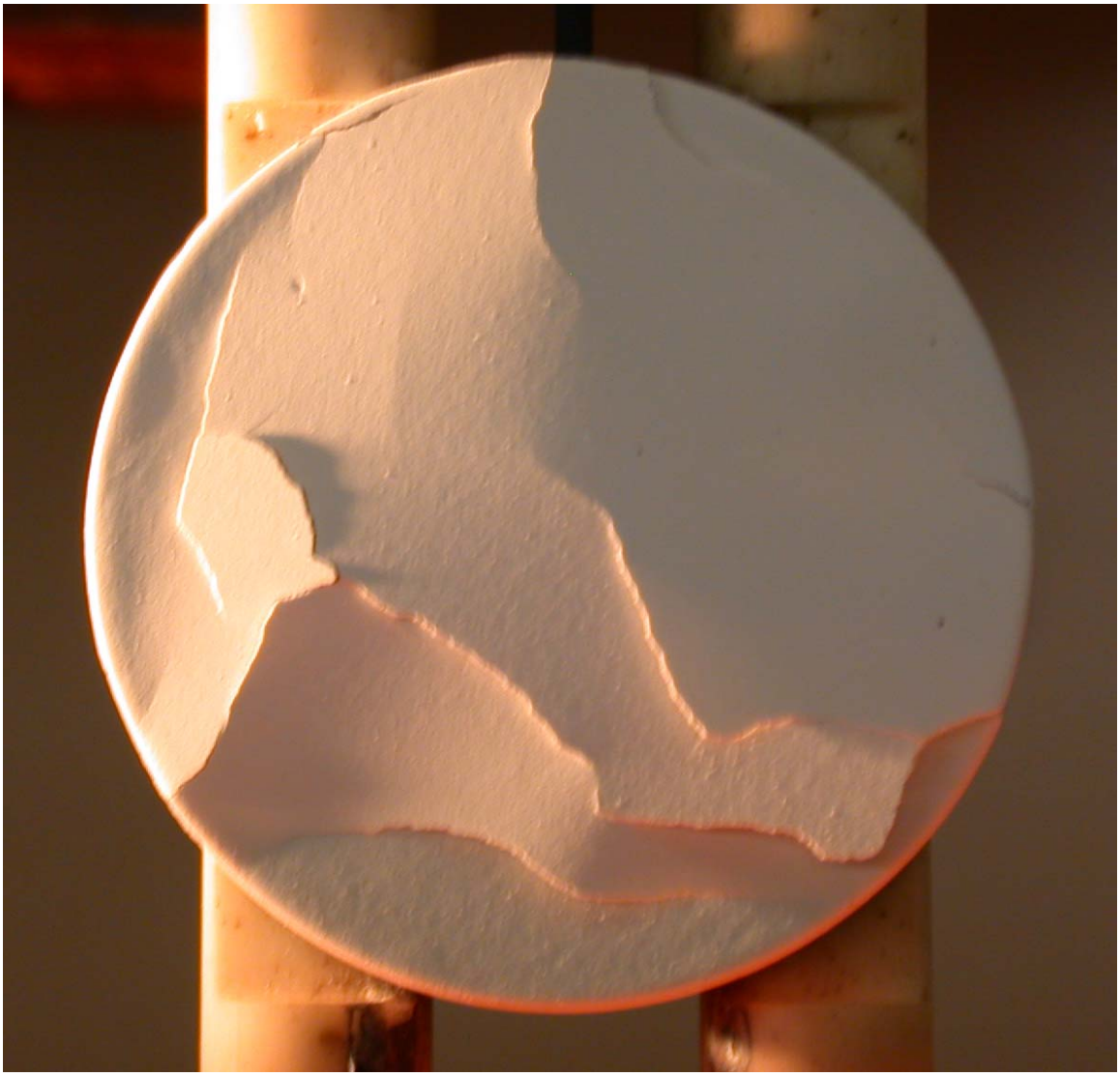

Figure 1.3: TBC spallation due to buckling after thermal cycling.

CHAPTER 2

INSTRUMENTED INDENTATION

Note: This chapter describes what is involved in making accurate modulus measurements using instrumented indenters. This background information supports the results provided in Chapter 3.

1. INTRODUCTION

Instrumented indentation is an indentation experiment with continuous measurement of the load and displacement. Since instrumented indentation needs only small volumes of material, this technique is suitable for determining localized materials properties and is especially useful in probing thin coating properties. Instrumented indentation has been used to probe elastic properties [56, 57], yield stress and strain hardening [79, 80], and residual stresses [81]. General elasto-plastic properties extraction procedures from instrumented indentation experiments have been suggested [82, 83]. The interfacial properties of thin films have also been studied by indentation [84, 85].

The elastic modulus is usually determined from the empirical methods given by Pharr *et al.* [57] and is usually based on the assumption of elastic recovery during unloading. The reduced elastic modulus, E_r which is a function of the specimen modulus and indenter modulus is defined by

$$\frac{1}{E_r} = \frac{1-\nu^2}{E} + \frac{1-\nu_i^2}{E_i}, \qquad \text{(Eq. 2.1)}$$

where ν and E and ν_i and E_i are the Poisson's ratio and elastic modulus for the test material and indenter, respectively. The reduced elastic modulus is derived from

$$E_r = \frac{\sqrt{\pi}}{2\beta}\frac{S}{\sqrt{A}}, \qquad \text{(Eq. 2.2)}$$

where S is contact stiffness (slope of the unloading curve) and A is the projected contact area. β is a constant that depends on the geometry of the indenter. For a spherical indenter β =1. S is determined from a curve fit of the upper 20 to 50% of the unloading data. The contact area, A, is calculated by determining the contact depth, h_c, and using an area function as follows:

$$h_c = h_{Max} - \varepsilon\frac{P_{Max}}{S} \quad \text{and} \quad A = \pi h_c(D - h_c), \qquad \text{(Eq. 2.3)}$$

where h_{Max} and P_{Max} are maximum indentation penetration and maximum applied load, respectively. From elastic contact analysis, for a spherical indenter, the constant $\varepsilon = 0.75$. D is the diameter of the spherical indenter.

Figure 2.1 shows a typical instrumented spherical indentation curve with maximum load of 300 N. Fig. 2.1 illustrates how contact stiffness and contact depth can be found from the unloading portion of the indentation curve.

2. APPARATUS

A Quad Group (www.quadgroupinc.com) Alexandra instrumented indenter machine was used in this project. Figure 2.2 shows the indenter machine with a steel specimen, the spherical indenter tip, and a custom-made clamping device. The indenter machine has a load cell with an 850 N capacity and a linear variable differential transformer (LVDT) with maximum travel of 635 μm. The resolution for the load cell and the LVDT are 0.25 N and 0.15875 μm, respectively. The indenter loading rate can be controlled from 0.5 N/s to 50 N/s. The spherical indenter tip has a 1.5 mm diameter. The tip is made of tungsten carbide and is held in a stainless steel body. The modulus for tungsten carbide is 630 GPa and the Poisson's ratio is 0.21.

3. CALIBRATION

A wide range of indentation loads were applied to check how the estimate of modulus depends on indentation load. Figure 2.3 shows a steel specimen's elastic modulus estimates for 50 N to 700 N indentations. The specimen was not clamped for these measurements. Since the modulus should be approximately 200 GPa, Fig. 2.3 shows that the modulus is underestimated for all indentation loads. This underestimate can be corrected by including machine compliance in the calculation. In general higher indentation loads give lower modulus estimates. Fig. 2.3 shows that the load range of 200 N to 400 N generated the most consistent modulus estimate. Consistency can be improved through clamping of the specimen.

As indicated above, a reason why the modulus estimate falls short is related to the fact that the displacements measured in the indenter test include machine compliance. Therefore, without a machine compliance correction, the indentation results underestimate the modulus. The true displacement, h, of the tip into the material is defined by

$$h = h_t - C_m P, \qquad \text{(Eq. 2.4)}$$

where h_t is the total measured displacement and C_m is the machine compliance. P is the load for the corresponding measured displacement. C_m is defined through

$$C_t = C_s + C_m , \qquad \text{(Eq. 2.5)}$$

where C_t is the total measured compliance and C_s is the elastic compliance of the indenter-specimen contact. C_m is determined by using the following relation:

$$C_t = \frac{\sqrt{\pi}}{2\beta E_r}\frac{1}{\sqrt{A}} + C_m . \qquad \text{(Eq. 2.7)}$$

The intercept from a plot of C_t versus $A^{-1/2}$ provides C_m. The slope of the plot is proportional to E_r^{-1}. Alumina was used since it is elastic over a wide range of loads. Fourteen indentations were done and the plot of C_t versus $A^{-1/2}$ was obtained. By extrapolating the plot, the intercept, C_m was found. Figure 2.4 shows the calibration results. The intercept value found from Fig. 2.4 is C_m =1.1601E-8 m/N with standard deviation of 3.4501E-9.

Clamping of the specimen minimizes micro motion of the specimen. This is critical for modulus estimation since it reduces a large percentage of total displacement and gives stability during unloading. A 300 N indentation on a steel specimen will have

approximately 42 μm of total travel when unclamped. Clamping reduced the total displacement by an average of 6 μm. However, clamping also reduced the unloading slope by around 5%. Therefore, since total displacement and unloading slope effects cancel each other out, for higher loads the effects of clamping are less significant than anticipated for calculating elastic modulus. From the comparison of unclamped and clamped test results for 50 N steel indentation, clamping did give apparent increases in modulus estimates. Unlike for 300 N indentations, clamping for 50 N indentations reduced the total penetration and increased the unloading slope. Those combined results contributed to increased modulus estimates. It can be concluded that clamping is critical, especially for lower load indentations.

To ensure the consistency and accuracy of modulus estimations, fine polishing of top and bottom surfaces of indentation specimens is as important as compliance correction and clamping. By polishing specimen surfaces, specimen movement during the indentation and surface roughness effects are minimized. For smaller indentation tips and lower maximum indentation loads, finer polishing is required.

Three different materials with a range of moduli were used to calibrate the instrumented indentation machine. Table 2.1 shows the three materials and their

mechanical properties. For accuracy and consistency of the modulus estimates, all of the specimens were polished on both surfaces and clamping during each indentation run was used.

Figure 2.5 shows the elastic modulus estimates and standard deviations for each of the materials given in Table 2.1. Indentation loads of 50 N and 300 N were applied to surface polished and clamped specimens with 1 N/s and 10 N/s loading rates, respectively. Circle symbols and diamond symbols represent maximum indentation loads of 50 N and 300 N, respectively. Open symbols represent elastic modulus calculations from h_t, the total measured displacement (no compliance correction). Filled symbols represent elastic modulus calculations with corrected total displacements by using C_m = 1.2E-08 m/N. Fig. 2.5 shows that before machine compliance corrections, the moduli from the 50 N maximum indentation load experiments were higher than those from the 300 N indentations. However, after compliance correction, higher and more accurate modulus estimates for alumina and steel specimens resulted from 300 N indentations. For softer material like brass, compliance corrected 50 N indentations resulted in more accurate modulus estimates. Generally speaking, the compliance correction worsened the *consistency* of the elastic modulus estimations for both 50 N and 300 N indentations.

In conclusion, for harder materials like alumina and steel, 300 N indentation with a C_m = 1.2E-08 m/N correction will give accurate modulus estimates. For softer materials like brass, 50 N indentations with a C_m = 1.2E-08 m/N correction should be used to determine the modulus more accurately.

4. DISCUSSION AND CONCLUSIONS

From the results presented above, it has been shown that modulus calculations using the Quad Group Alexandra instrumented indenter are dependent on the clamping of the specimen to the indenter base, the machine compliance correction, polishing of the specimen surfaces, and the specimen material. Naturally, repeatability and accuracy of the indention process and its results is a critical issue.

Clamping can have a significant effect on the indentation of specimens. Clamping will reduce the effects of any gaps that may be present between the specimen and the base indenter table. For all load ranges, clamping of specimens reduced the total depth of penetration. For higher loads, the reduction in penetration depth was a small percentage of the total penetration. However, at small loads, the percentage was much higher. In addition, for smaller loads clamping resulted in much more consistent results.

Machine compliance was calculated using an alumina specimen. Alumina, steel, and brass specimens were then indented. When machine compliance corrections were applied to 50 N indentation data, except for the alumina specimens, the resulting moduli were close to the book-value moduli. However, for 300 N indentation, only the indentations on the steel and alumina specimens yielded reasonably accurate moduli. The brass specimens indented at 300 N gave moduli that were significantly lower than the book-values. For higher loads the data that had not been corrected for machine compliance is relatively consistent. Correcting for machine compliance magnifies small differences in the data and results in large scatter in the final results.

Depending on specimen material properties (*i.e.*, the hardening exponent), the applied load has significant effects on plastic flow. For simple tension tests, more consistent unloading slopes are observed after the specimen is deforming in a fully plastic manner. It seems that this higher consistency can be obtained in an analogous manner for spherical indentation modulus determinations. The development of fully plastic flow is measured using Pm, the mean pressure over the circle of contact and Y, the yield stress in simple tension and compression. When Pm/Y reaches 1.1, yielding is initiated in a localized region. Throughout the range $Pm/Y = 1.1$ to $Pm/Y = 3.0$, the indentation is

elastic and plastic. When *Pm/Y* reaches 3.0, fully plastic flow is developed. For instance, steel 1018 specimens with a yield stress of 386 MPa has *Pm/Y=5.5* for a 100 N indention. Therefore, it can be concluded that after 100 N, fully plastic flow is generated. It seems that this full plasticity contributes to the consistency of moduli estimates for the higher load range (100 N-700 N). It is not known if there should be certain "degree of plasticity" guidelines which relate the equations used (and machine compliances) for each material and each load range.

For accurate and consistent modulus estimates, accurate depth measurement and consistent unloading slopes are essential. The loading profiles often show a few microns of initial displacement without corresponding loading. This indicates that when the indenter moves down and stops after finding initial contact with the specimen surface, there is still a gap between the indenter tip and the specimen surface. This yields incorrect total displacement. The other more critical problem is inconsistency of the unloading profile, especially for harder materials. It is not uncommon for two tests that have almost identical loading profiles to have very different unloading profiles. These differences easily generate around 25% discrepancy in modulus estimate. The unloading slopes for brass material indentation tests are very consistent compared to those for the

steel indentation tests. It seems that during the unloading process, the stability of the system becomes worse for harder materials.

Chapter 3 will describe how PtAl bond coat specimens were degraded with thermal cycling and how the modulus was measured with room temperature indentation at regular intervals. The modulus of the as-coated bond coat is similar to a steel 1018 specimen. Therefore, 300 N maximum load indentations were used to ensure fully plastic indentation. Compliance correction with C_m = 1.2E-08 m/N was used to obtain more accurate modulus estimates.

Specimen	Alumina	Steel	Brass
E (GPa)	350-370	190-210	96-110
ν	0.25	0.27-0.3	0.33

Table 2.1: Calibration specimens with their book-value elastic moduli and Poisson's ratios.

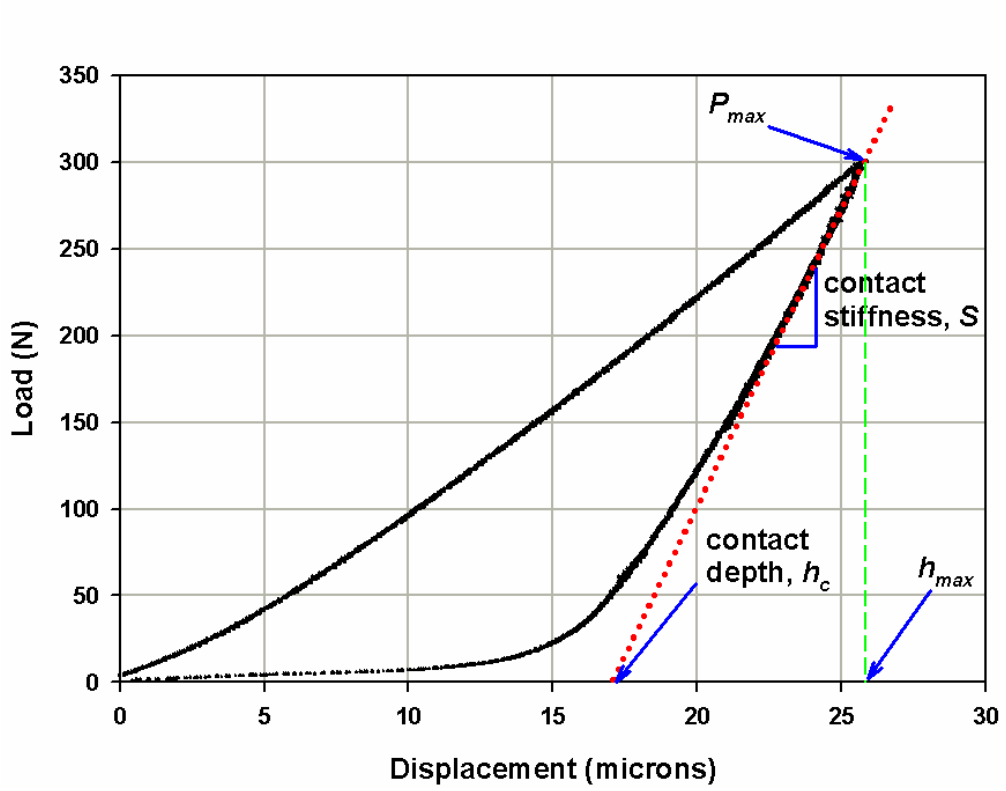

Figure 2.1: A typical loading/unloading curve from instrumented indentation with a spherical indenter.

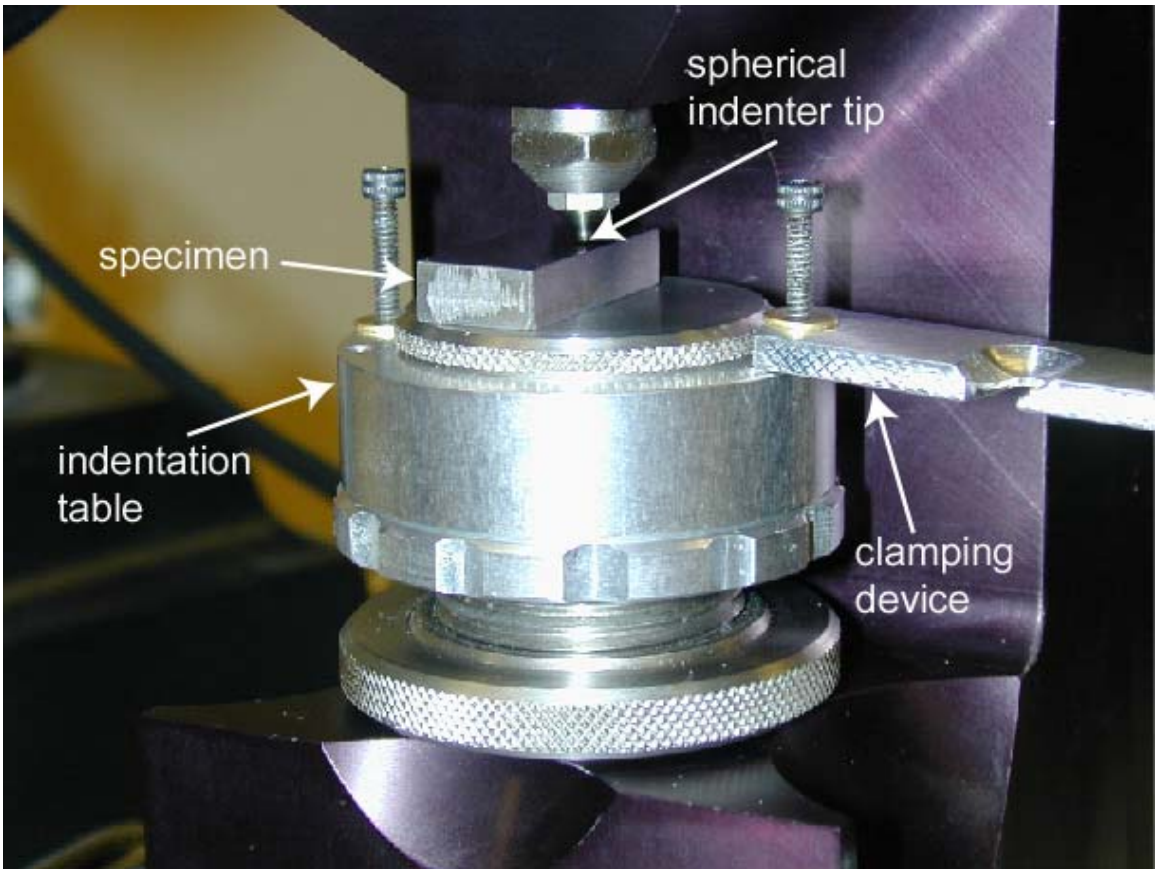

Figure 2.2: Quad Group Alexandra instrumented indenter machine with a spherical indenter and showing a custom-made clamping device.

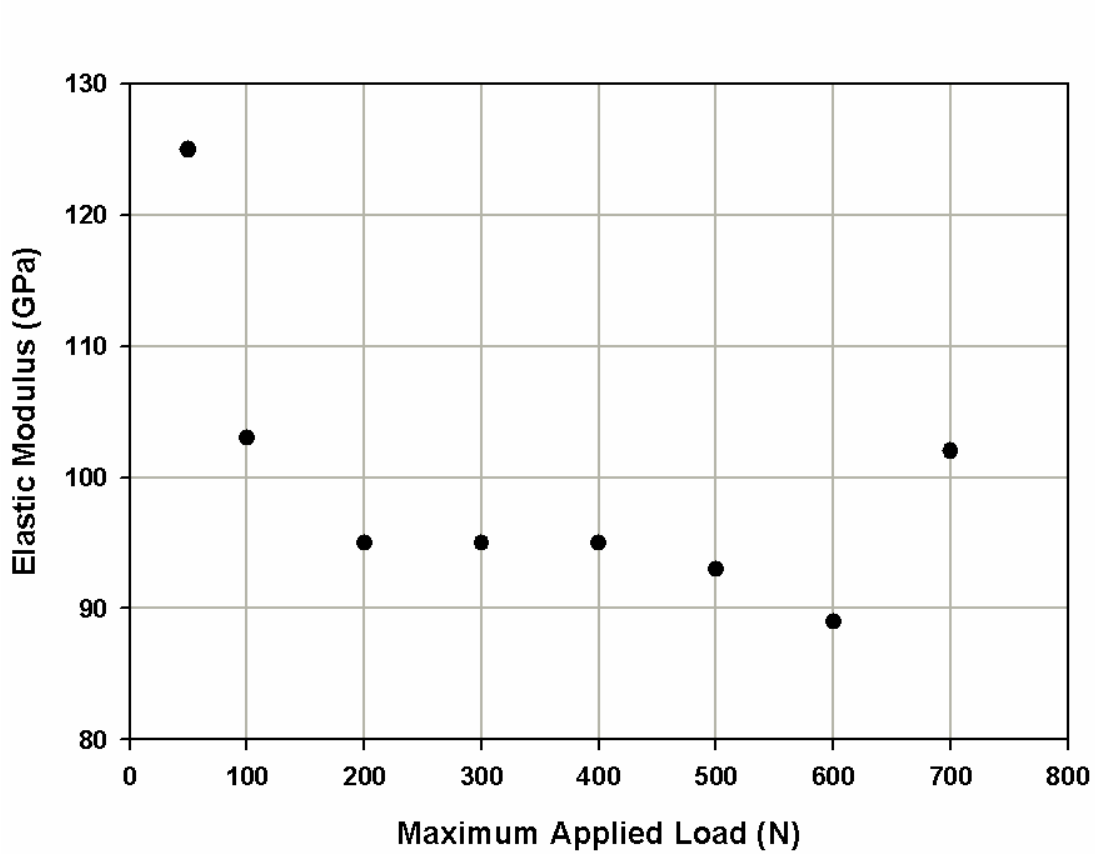

Figure 2.3: Measurements of the modulus for a steel specimen modulus for 50 N to 700 N indentation tests.

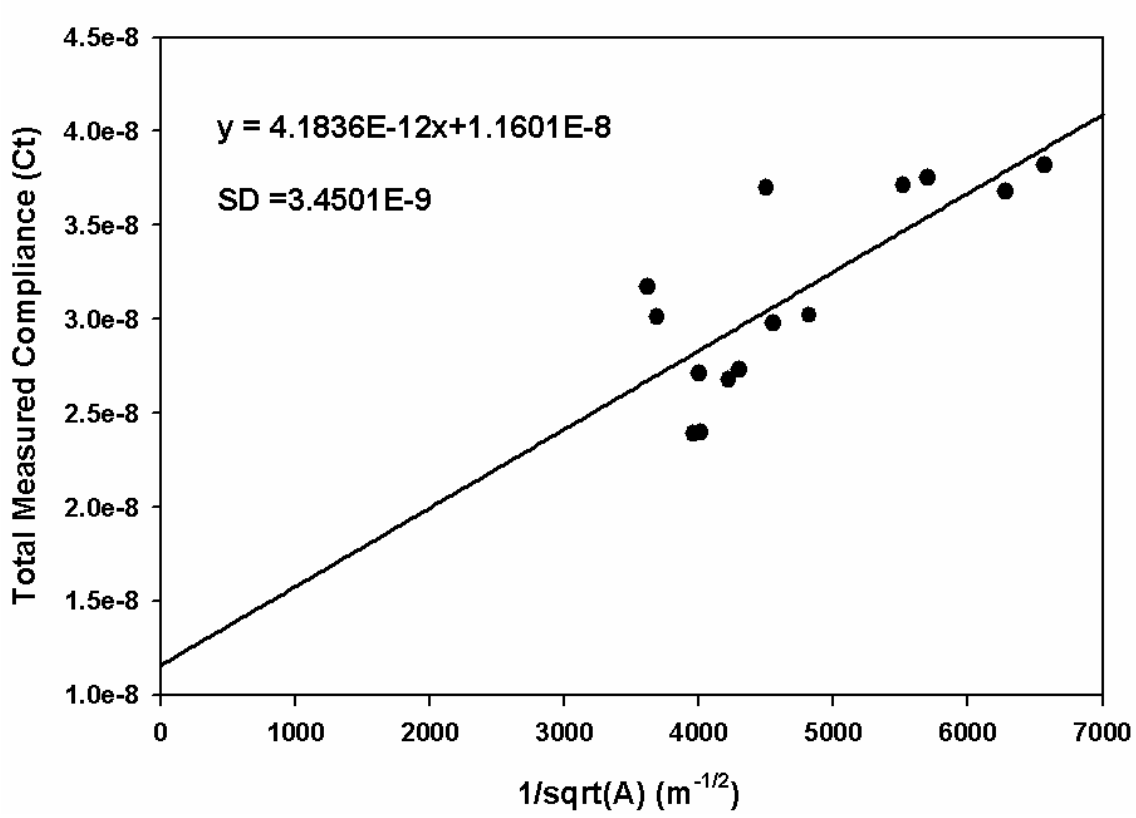

Figure 2.4: A plot of C_t versus $1/A^{1/2}$ for an alumina specimen.

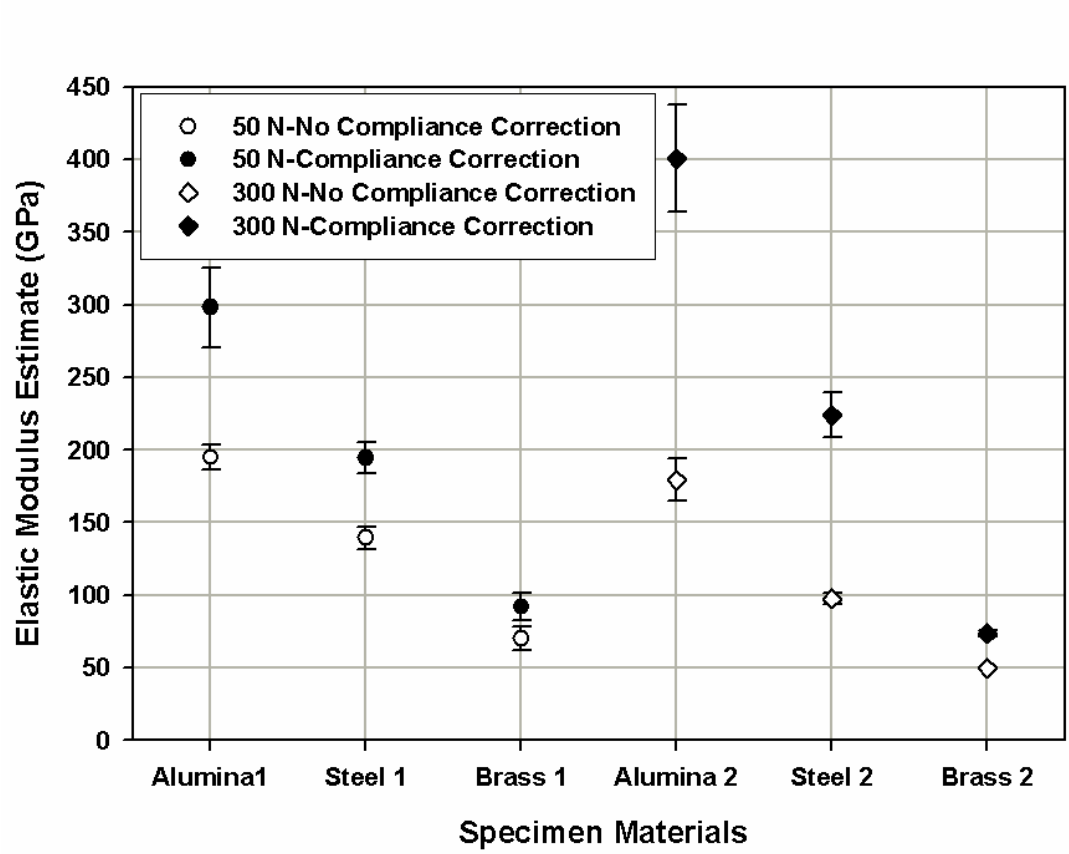

Figure 2.5: Modulus estimates of various materials before and after compliance correction for 50 N and 300 N indentations with *Cm* = 1.2E-08 m/N.

CHAPTER 3

CHARACTERIZATION OF THE DEGRADED MICROSTRUCTURES OF A PLATINUM ALUMINIDE COATING

Note: The first four sections of this chapter are essentially the same as the corresponding sections of a published journal article with the following citation: Kim HJ, Walter ME, "Characterization of the degraded microstructures of a platinum aluminide coating," MATERIALS SCIENCE AND ENGINEERING A-STRUCTURAL MATERIALS PROPERTIES MICROSTRUCTURE AND PROCESSING 360 (1-2): 7-17 NOV 15 2003.

1. INTRODUCTION

Thermal barrier coating (TBC) systems are typically applied to nickel-based superalloys used in hot-sections of gas turbine engines. The TBC system's insulating ceramic top coat lowers the temperature seen by the superalloy substrates. To further protect the substrate from oxidation and hot corrosion and to improve adhesion of the ceramic top coat, a bond coat is applied between the top coat and the substrate. During high temperature exposure, a thermally grown oxide (TGO) grows between the top coat

and the bond coat. Due in large part to its stable, slow growing TGO layer, platinum modified aluminide (PtAl) coatings are one of the most popular types of bond coats for TBC systems.

Spallation of the ceramic top coat exposes the bond coat and the substrate to higher temperatures and to aggressive combustion gases. This situation must be avoided for safe, low maintenance (low cost) operation. Recently, Evans *et al.* [18] have postulated a sequence of events that could lead to top coat spallation, and it is seen that TGO growth and bond coat evolution play an integral role in the ultimate failure of the TBC system. In particular, it is thought that defects coupled with the stresses associated with TGO waviness are the main reason why small cracks develop and propagate at the TGO interface. Eventually the cracks link together and cause macroscopic spallation of the ceramic top coat [23].

Much of the recent research aimed at understanding and improving TBCs focuses on the development of the TGO layer as it relates to the bond coat. Monceau *et al.* [14] have investigated several bond coat systems, with different surface treatments and under different thermal conditions. It was found that Pt alloying resulted in the best TGO adherence. The diffusion of hafnium from the substrate [31] and the presence of

sulfur in the coating or the substrate [14] significantly degraded the TGO quality. Others have also found that voids under the TGO begin with ridges associated with bond coat grain boundaries [36]. In the vicinity of grain boundary ridges TGO integrity is diminished, and therefore preferential oxidation along the near-surface bond coat grain boundaries occurs. With thermal cycling the oxidized grain boundaries cause cyclic plasticity in the bond coat and void growth results. TGO waviness has also been associated with initial processing defects [23]. Furthermore, the undulation amplitude of the TGO may be increasing through plastic ratcheting of the bond coat [33]. Phase changes from β-(Ni,Pt)Al to γ'-(Ni_3Al) are thought to cause resistance to downward displacement of the TGO [3] and may also enhance waviness since the phase change results in a volume reduction [20].

TBC technology will be greatly enhanced by better understanding of how the thermal environment affects microstructural evolution of the bond coat and by measuring bond coat properties as a function of the thermal exposure. There have been a number of studies of bond coat phase evolution. Transformation of β-(Ni,Pt)Al phase to γ'-(Ni_3Al) phase has been observed for 1100 ºC isothermal exposure and is presumed to be driven by depletion of aluminum [13]. Thermo-mechanical cycling of an aluminide coating on a

superalloy was also investigated, and the formation of oxide, onset of oxide scalloping, and fracture of the coating were described in detail [32]. More recently, for study of the quality of the oxide scale formation, the microstructure of different bond coat systems was described [14, 31]. The evolution of the inter-diffusion layer and outer, near-coating superalloy material has also received attention [32, 86]. In light of the recent modeling efforts in this area [18], it is important to consider mechanical property changes and to quantitatively analyze microstructural evolution in bond coat systems experiencing different thermal exposures.

2. MATERIAL SYSTEM AND EXPERIMENTS

The Howmet Corporation provided unactivated pack cementation (inward diffusing) PtAl bond coats (LDC-2E) completely covering CMSX-4 superalloy buttons. The resulting coating is very brittle, and before further processing or being put into service, PtAl bond coats are subjected to a stabilizing heat treatment. The buttons were therefore held in a vacuum furnace for 4 hours at 1080 ºC.

Experiments were performed with quadrants of the 25.4 mm diameter by 3.2 mm thick buttons. One quadrant was heated quasi-isothermally by placing it in a box furnace already at 1200 ºC for 10 hour intervals. After 10 hours, the specimen was

cooled slowly to room temperature, and the TGO was removed with 600 to 2000 grit sand paper. By observing the surface of the specimen with optical microscopy, it was relatively easy to tell when the TGO was completely removed. Removal of the TGO was expected to alter the oxidations kinetics and accelerate aluminum depletion in the bond coat. Therefore, throughout this chapter experiments for which TGO was periodically removed are called "accelerated aluminum depletion" experiments. In addition, it is necessary to polish both specimen surfaces for accurate indentation results. Before returning the sample to the furnace, indentation measurements were made and a small piece of the specimen was removed. For comparison to this quasi-isothermal heating, an 80 hour, true-isothermal sample was also prepared. Another quadrant was thermally cycled from room temperature with a heating rate of 170 ºC/minute, a 10 minute hold at 1200 ºC, and an average cooling rate of 480 ºC/minute. This heating profile was achieved with a stepper motor system to bring the sample in and out of a box furnace's hot zone and with compressed air cooling. As with the quasi-isothermal specimens, cyclic experiments were stopped every 10 hours for polishing, indentation, and sectioning. The small pieces removed from the quadrants were mounted in epoxy such that the button's edge with no TGO removal and the top and bottom button surfaces with

TGO removal were all visible. The molded specimens were polished down to 0.25 μm diamond paste and then placed in a vibratory polisher with 0.05 μm colloidal silica for 12 hours.

3. RESULTS AND DISCUSSION

3.1 BOND COAT EVOLUTION

Figure 3.1 shows a backscatter SEM micrograph of the as-coated PtAl bond coat system. From energy dispersive spectroscopy (EDS), the as-coated sample has a 66 μm region of approximately 50% Ni and 50% Al with some bright white precipitate particles. Chemical analysis and other literature [87] indicate that these white precipitates in the bond coat are either α-Cr or α-W precipitates. The Ni and Al percentages indicate that the upper 66 μm is mostly β-(Ni,Pt)Al, and the backscatter imaging in Fig. 3.1 shows distinct grains in this region. The contrast between grains could be the result of elemental or orientational differences. Phase identification on different grains was performed with electron beam scatter patterning (EBSP), but despite careful specimen preparation, very few EBSP patterns matched β-NiAl exactly. This may be a result of distortion from Pt-phases, however, it is also possible that very small

γ'-(Ni_3Al) particles exist throughout the β-NiAl phase. This paper will continue to refer to the "β-(Ni,Pt)Al region" even though it is not pure β-NiAl. As seen in Fig. 3.1, entrapped alumina particles (black color) are scattered throughout the top 17 μm of the β-(Ni,Pt)Al region. Under the β-(Ni,Pt)Al region, an approximately 42 μm thick inter-diffusion layer exists with larger white colored precipitate particles. These precipitates have been identified as μ-phase precipitates [88].

Figures 3.2a and 3.2b show nominal chemical compositions for an as-coated specimen and a 20 hour cyclic non-accelerated aluminum depletion specimen. The compositions were determined with EDS line scans parallel to the coating surface and at regular depth increments. Fig. 3.2a shows that for both specimens, the Ni content is nearly constant in the bond coat and inter-diffusion layer and increases in the substrate. The Al content is decreasing for both specimens as the distance from the outer surface increases. After 20 hours of cyclic heating, the Al content has decreased in the bond coat region, is unchanged in the inter-diffusion region, and has increased in the substrate. These nominal changes are the result of Al diffusion toward the outer surface to form the TGO layer and Al diffusion toward the substrate. After 20 hours of cyclic heating, the Ni content change shows the opposite trend compared to Al content. Fig. 3.2b shows that in

the as-coated specimen, Pt content reaches more than 10% at the top portion of the bond coat region and rapidly decreases to 0% in the inter-diffusion layer and the substrate. After 20 hours of cyclic heating, the Pt content is nearly constant at 3% in the bond coat and inter-diffusion regions. The Cr content of the as-coated specimen increases with coating depth. After heating, the Cr content is more or less constant in the bond coat and inter-diffusion region. The W content is initially highest in the inter-diffusion region. After heating, there is noticeably more W in the substrate. The W content in the upper portion of the bond coat does not change. These compositional changes indicate how elements diffuse during cyclic heating of the bond coat system.

SEM micrographs show that bond coat microstructural evolution is dependant on the heating method and the presence of the TGO layer. Figures 3.3a and 3.3b show 20 hour cyclic and quasi-isothermal non-accelerated aluminum depletion samples. There is no indication of γ'-(Ni_3Al) phase development in either Figures 3.3a or 3.3b. However, as compared to the quasi-isothermal case, the cyclic case has more precipitates throughout the entire bond coat, inter-diffusion layer, and substrate. The differences in precipitate distribution provide evidence that cyclic heating alters diffusion kinetics.

Figures 3.3c and 3.3d show 20 hour cyclic and quasi-isothermal accelerated aluminum depletion samples. The backscatter electron images show distinct (bright grey) phases which, from EDS element percentages, are found to be γ'-(Ni_3Al) phase. The series of micrographs in Fig. 3.3 clearly show that TGO removal significantly increases the formation of γ'-(Ni_3Al) phase. The γ'-(Ni_3Al) phases are predominantly located along the grain boundaries, the bond coat top surface, and the interface between the inter-diffusion layer and bond coat. Although the location of γ'-(Ni_3Al) formation in the 20 hour quasi-isothermal accelerated aluminum depletion sample (Fig. 3.3d) is similar to the 20 hour cyclic accelerated aluminum depletion sample (Fig. 3.3c), it is clear that the cyclic specimen has more γ'-(Ni_3Al) phase. To quantify the phase percentages an image analysis program (Clemex Vision; www.clemex.com) was employed. For each micrograph, threshold grey-levels were set to distinguish among precipitates, γ'-(Ni_3Al), and the "background" (β-(Ni,Pt)Al). For calibrating this analysis, typical precipitate particles and β-(Ni,Pt)Al phase particles were chosen, and the threshold grey-levels were set according to these particles for the higher and lower threshold limits, respectively. Although re-calibrations were done for each micrograph, the threshold values did not change much. Results are shown in Fig. 3.4, and it is seen that the 20 hour cyclic

accelerated aluminum depletion sample has approximately twice the amount of γ'-(Ni_3Al) phase compared to the 20 hour quasi-isothermal accelerated aluminum depletion sample. It is also observed that there are differences in morphology between γ'-(Ni_3Al) phases from cyclic and quasi-isothermal heating; cyclic γ'-(Ni_3Al) phases show sharp edges and quasi-isothermal γ'-(Ni_3Al) phases show rounded edges.

Figures 3.5a and 3.5b are higher magnification views from within Fig. 3.3c, and new, needle shape microstructural features are visible. The needle shape features appear only on cyclic accelerated aluminum depletion samples after 10 hours of heating. In addition, these needle shape features are most prominent in the 20 hour cases and are no longer found after 50 hours. Figures 3.5a and 3.5b also show that there are more of these features where larger γ'-(Ni_3Al) phases are absent. It is believed that these features are part of a transition from β-(Ni,Pt)Al to γ'-(Ni_3Al). Since these microstructural features do not appear in the quasi-isothermal samples, this is an indication that the formation of γ'-(Ni_3Al) phase is mechanistically very different for quasi-isothermal and cyclic heating. The different γ'-(Ni_3Al) phase shapes for different heating types also support this observation.

The narrow bands indicated by arrows in Fig. 3.5b appear at various stages in the β-(Ni,Pt)Al phase of all samples. It is not known if the bands are from plastic slip or if they represent compositional or crystallographic variations in individual grains. The β-(Ni,Pt)Al phase will not readily deform plastically at low temperature, and at higher temperatures β-(Ni,Pt)Al deforms through dislocation climb [89]. It is possible that a martensitic phase of β-(Ni,Pt)Al would show band-like features. In any case, the bands are broken up by γ'-(Ni_3Al) phases.

Starting after 60 hours of heating, cyclic and quasi-isothermal accelerated aluminum depletion samples show even more significant differences in microstructural evolution. When comparing 70 hour cyclic and quasi-isothermal samples in Figures 3.6a and 3.6b, it is seen that the cyclic sample has much more γ'-(Ni_3Al) phase distributed throughout the coating. In fact, as shown in Fig. 3.4, the 70 hour cyclic sample coating is composed of nearly 50% γ'-(Ni_3Al) phase. In comparing the 70 hour cyclic and 20 hour cyclic samples in Figures 3.6a and 3.3c, respectively, it is seen that for the 70 hour case, grain boundaries have become very distinct and the γ'-(Ni_3Al) phases have become larger with more rounded edges. On the other hand, with only increased sizes of the γ'-(Ni_3Al)

phases, the differences between the 70 hour quasi-isothermal (Fig. 3.6b) and 20 hour quasi-isothermal (Fig. 3.3d) are less significant.

Figures 3.7a-3.7c show 80 hour cyclic, quasi-isothermal, and true-isothermal non-accelerated aluminum depletion samples, respectively. All the 80 hour samples show very distinct γ'-(Ni_3Al) phases and grain boundaries. In addition, the precipitates are much larger than those in the 20 hour samples. As seen in Fig. 3.7c, the true-isothermal sample shows small, slender features which are believed to be γ'-(Ni_3Al) phase distributed throughout the bond coat. On the other hand, the microstructures observed in the cyclic specimens (10 minute cycles) and quasi-isothermal specimens (10 hour cycles) are relatively similar. Thus, observations indicate that for non-accelerated samples with long times at temperature, the period for cyclic heating is relatively unimportant for *bulk* microstructural evolution.

The surface morphology does depend significantly on the period of the heating cycle. As seen in Figures 3.7a-3.7c, the surface undulation amplitude decreases and the sharpness of the undulations increases as the periods of the cycles decrease (*i.e.*, for longer isothermal hold). Furthermore, differences between the waviness of the boundary between the bond coat and the top of the inter-diffusion layer are also observed, and short

period cyclic heating (10 minute cycles) has the most waviness associated with this boundary. The inter-diffusion layer waviness is most likely related to the plastic deformation in the bond coat that is driven by thermal cycling [20].

3.2 SUBSTRATE EVOLUTION

Figures 3.8a-3.8c show the inter-diffusion layer and substrate region of the as-coated, 10 hour cyclic non-accelerated aluminum depletion, and 10 hour isothermal non-accelerated aluminum depletion samples, respectively. The substrate shows a superalloy microstructure with web and plate-like features. The web-like features are γ-(Ni) phases and the plate-like features are γ'-(Ni_3Al) phases [90]. While the as-coated sample shows finger-like features between the substrate and the inter-diffusion layer, the 10 hour cyclic and isothermal non-accelerated aluminum depletion samples show smoothened substrate/inter-diffusion layer interfaces. Comparisons of the inter-diffusion layers before and after heating indicate that the inter-diffusion layer has advanced into the substrate.

In Fig. 3.8b, a 10 hour cyclic sample shows precipitates oriented at ± 45º to the coating interface. These precipitates disrupt the γ-(Ni) phase web and are reported to be σ-phase, which is rich in chromium and other refectory elements [88]. The precipitate

orientation is typical for single crystal substrates having a surface normal coinciding with the <100> direction [32]. Due to thermal expansion mismatches between different regions of the sample, during the 1200 ºC cyclic heating, the substrate near the diffusion boundary may undergo compression and/or tension cycling. As seen in Fig. 3.8c, 10 hour isothermal non-accelerated aluminum depletion samples have only very small, round σ-phase precipitates forming in the substrate. The distinct differences between the size and morphology of σ-phase precipitates forming in the superalloy indicate that the stresses caused by cyclic heating accelerate the growth of σ-phase precipitates.

For longer heating times, σ-phase precipitates in the substrates of both the quasi-isothermal and cyclic samples are larger and occur deeper into the substrate. Figures 3.7a-3.7c illustrate that after 80 hour exposures, the quantities and shapes of the σ-phases in the substrate are very different for the different types of heating. Cyclic specimens show rounded precipitates, quasi-isothermal specimens have elongated precipitates, and true-isothermal specimens have irregularly spaced and shaped precipitates. As mentioned previously, the average inter-diffusion layer thickness for the as-coated sample was 42 μm. In the 80 hour sample cases, the average inter-diffusion layer elongated by approximately 12 μm in the substrate direction. Due to the inward

diffusion of Al and the outward diffusion of Ni, the γ/γ' substrate adjacent to the bond coat boundary transforms into a mixture of γ'-phase, β-phase, and μ-phase precipitates [88]. The μ-phase precipitates extend across the bond coat/substrate interface through grain boundary segregation of surrounding β-phase, and for longer heating times, the β-phase transforms into γ'-phase [88].

Near the substrate interface, the cyclic and isothermal 10 hour non-accelerated samples show rafting of the γ/γ' microstructure parallel to the substrate and bond coat boundary. Since it alters dislocation motion (plasticity) in the γ–channels, rafting lowers creep resistance [91] and is an important area of research for superalloy materials. For uncoated superalloys, in uniaxial tension rafting occurs perpendicular to the tensile loading direction, and under shear loading rafting occurs at 45º to the shear loading direction [91]. Under compressive loading, rafts are parallel to the loading direction [92]. For a superalloy substrate with an aluminide coating, Bressers *et al.* [86] show that the formation of a monolithic γ'-phase near the bond coat/substrate interface results in biaxial compressive stresses that cause rafting parallel to the interface. As a result of stress-altered diffusion, the monolithic γ'-phase was found to be thickest and therefore the most rafting was observed when compressive thermo-mechanical cycling was performed. For

the present investigation, although there was no direct mechanical loading of the specimen and it is not clear to what degree a monolithic γ'-phase is formed, there are lattice mismatches, thermal expansion mismatches, and diffusion gradients which can all contribute to rafting. For all types of heating, the rafted region of the substrate expands with longer heating times. When comparing the degree of rafting between the cyclic and isothermal 10 hour non-accelerated aluminum depletion samples, the isothermal samples show significantly more rafting.

3.3 SCHEMATIC REPRESENTATION OF THE MICROSTRUCTURAL EVOLUTION

To summarize the microstructural evolution observations, Figures 3.9a-3.9d schematically show the significant microstructural features and changes to both the bond coat and substrate after 80 hours of heating for four situations: cyclic heating with TGO, quasi-isothermal heating with TGO, cyclic heating without TGO, and quasi-isothermal heating without TGO. Cyclic samples show more γ'-(Ni_3Al) phase and more distinct grain boundaries as compared to quasi-isothermal samples. Also, cyclic samples show more waviness of the inter-diffusion layer and the top surface. Therefore, it is evident that cyclically induced stresses disturb the top surface and inter-diffusion layer

boundaries, and alter diffusion processes in the coating. As seen in Figures 3.9a-3.9d, accelerating aluminum depletion by periodic removal of TGO hastens the formation of γ'-(Ni_3Al) and accentuates differences between cyclic and quasi-isothermal exposure. Microstructural evolution in the substrate was also very dependent on the type of heating. Initially, compared to isothermal samples, cyclically exposed substrates had more significant precipitate growth. At later stages, precipitates in cyclic samples were generally round, whereas precipitates in isothermal samples had high aspect ratios.

4. MECHANICAL CHARACTERIZATION OF THE COATING

To evaluate the evolution of bond coat mechanical properties, instrumented indentation to 300 N was performed after every 10 hours of heating. To probe coating properties, a 1.5 mm diameter spherical indenter tip was used in the instrumented indenter shown in Fig. 2.2. At these large indentation loads, the indenter is sampling a relatively large area of the coating and averaging over many grains. Since the indentation depths are approximately 23 μm, substrate properties have minimal influence on the indentation results. As was discussed in Chapter 2, for accurate, repeatable indentation results, polished surfaces are required. Furthermore, a clamping device for the indenter is also needed to add additional consistency to the results. Results were repeatable to

within ± 2 GPa. As presented in Chapter 2, the modulus was determined from the unloading slope of the indentation curve using the methods of Pharr *et al.* [57]. Figure 3.10 shows indentation results for an as-received substrate, an as-coated sample, and cyclic and quasi-isothermal accelerated aluminum depletion samples. For 10 to 50 hours of heating, the moduli of the cyclic and quasi-isothermal samples are relatively constant. It was observed that removing the TGO layer for the cyclic samples required very little sanding. For quasi-isothermal samples, the TGO layer was much more adherent. Since removal of the bond coat itself was to be avoided, often times, a thin grey layer was left on the quasi-isothermal samples. SEM established that the grey layer was a relatively porous TGO. This porous layer led to a slight decrease in the modulus of the quasi-isothermal samples. After approximately 60 hours of quasi-isothermal heating, the TGO was easier to remove.

After 50 hours of heating, the modulus of the cyclic sample rose rapidly. The quasi-isothermal sample's modulus increased very slowly after 60 hours. The prevalence of γ'-(Ni_3Al) phase near the top of the bond coat has been observed in cyclically heated samples from as early as 20 hours of heating. The increase was more apparent after 40 hours, and, as seen in Fig. 3.11, the 60 hour cyclic accelerated aluminum depletion

sample's top surface is mostly γ'-(Ni_3Al). It has been postulated that the γ'-(Ni_3Al) phase is more resistant to downward displacement [3], and it is believed that this increased rigidity also causes the increase in modulus observed in the current experiments.

5. INDENTATION MODELING: RULE OF MIXTURES

PtAl bond coats transform into β-(Ni,Pt)Al and γ'-(Ni_3Al) after thermal loading. As seen in Fig. 3.11, compared to quasi-isothermal specimens, the cyclic specimens showed more γ'-(Ni_3Al) phase. The quantification of phases was discussed in Sec. 3.1. Fig. 3.4 shows that the 70 hour cyclic accelerated aluminum depletion sample had approximately 44% γ'-(Ni_3Al) and the 70 hour quasi-isothermal accelerated aluminum depletion sample had only 15.5% γ'-(Ni_3Al).

Since the indentation described in Sec. 4 averages over a large number of grains and phases, this indentation gives a composite material modulus. If the *area* fractions of γ'-(Ni_3Al) are assumed to be *volume* fractions of the reinforcement, f and if β-(Ni,Pt)Al is regarded as the matrix of the composite, the modulus of composite, E_c can be modeled by a Voigt model (rule of mixtures),

$$E_c = f\,E_r + (1-f)\,E_m, \qquad \text{(Eq. 3.1)}$$

where E_r and E_m are moduli of γ'-(Ni_3Al) and β-(Ni,Pt)Al, respectively. Since the Cr and W content and distribution in the bond coat does not change significantly after heating, these precipitates are regarded as inclusions in the β-(Ni,Pt)Al matrix. The modulus of the matrix can be approximated by the modulus of the as-coated specimen where no significant γ'-(Ni_3Al) is present and therefore E_m = 161.4 GPa. Using Eq. 3.1 with known values for volume fraction and measured composite modulus results in Fig. 3.10, for the 70 hour cyclic and quasi-isothermal cases, the γ'-(Ni_3Al) modulus turned out to be 187.7 GPa and 205.4 GPa, respectively. The modulus for the 70 hour cyclic case is comparable to the book value for the modulus of single crystal γ'-(Ni_3Al). The relatively high γ'-(Ni_3Al) phase modulus estimate in the quasi-isothermal cases seemed to come from the underestimate of the area fractions of the γ'-(Ni_3Al) phase. A high magnification SEM micrograph which had small field of view was used to estimate the area fractions of γ'-(Ni_3Al). This micrograph most likely fails to provide a representative image of the average 70 hour quasi-isothermal specimen for γ'-(Ni_3Al) and β-(Ni,Pt)Al phase area fractions determination.

It has been observed that the transformation from β-(Ni,Pt)Al to martensite happens during cooling cycles [34]. Since martensitic transformation is volume

shrinkage process, martensite is brittle and hard. So, the higher modulus of γ'-(Ni_3Al) seems to result from martensitic transformation of the bond coat during thermal cycling.

6. CONCLUSION

The degradation of a platinum modified aluminide coating and a CMSX-4 superalloy substrate were investigated for cyclic and quasi-isothermal heating to 1200 ºC. To accelerate oxidation of the specimens, the thermally grown oxide was removed at 10 hour intervals. For up to 80 hours of exposure, comparisons of specimens with periodic oxide removal and those without oxide removal were made. Microstructural evolution was quantified through backscatter scanning electron microcopy and image analysis. The following summarizes the main results found in this chapter:

The microstructural evolution of a PtAl *bond coat* is significantly influenced by the type of thermal exposure and the presence of TGO. Specimens have been characterized for exposure up to 80 hours at 1200 ºC, and the thermal loading and TGO presence were found to have the greatest impact on γ'-(Ni_3Al) phase transformation, the formation of needle shape features in β-(NiAl), and bond coat surface undulation.

The microstructural evolution of the superalloy *substrate* associated with a PtAl bond coat is also influenced by the type of thermal exposure. The extent of rafting of the γ/γ'

microstructure and the formation of σ-phase precipitates depends on whether the system is exposed isothermally or cyclically. The differences between cyclic and quasi-isothermal heating indicate that stresses associated with cooling and heating significantly alter microstructural evolution.

Indentation results on cyclic and quasi-isothermal accelerated aluminum depletion samples show increasing trends in modulus as heating time increases. It was observed that after 60 hours of heating, higher γ'-(Ni_3Al) phase contents were measured. After 60 hours of heating, the modulus of the samples rose significantly. This higher modulus seems to confirm that γ'-(Ni_3Al) phases are more resistant to downward displacement.

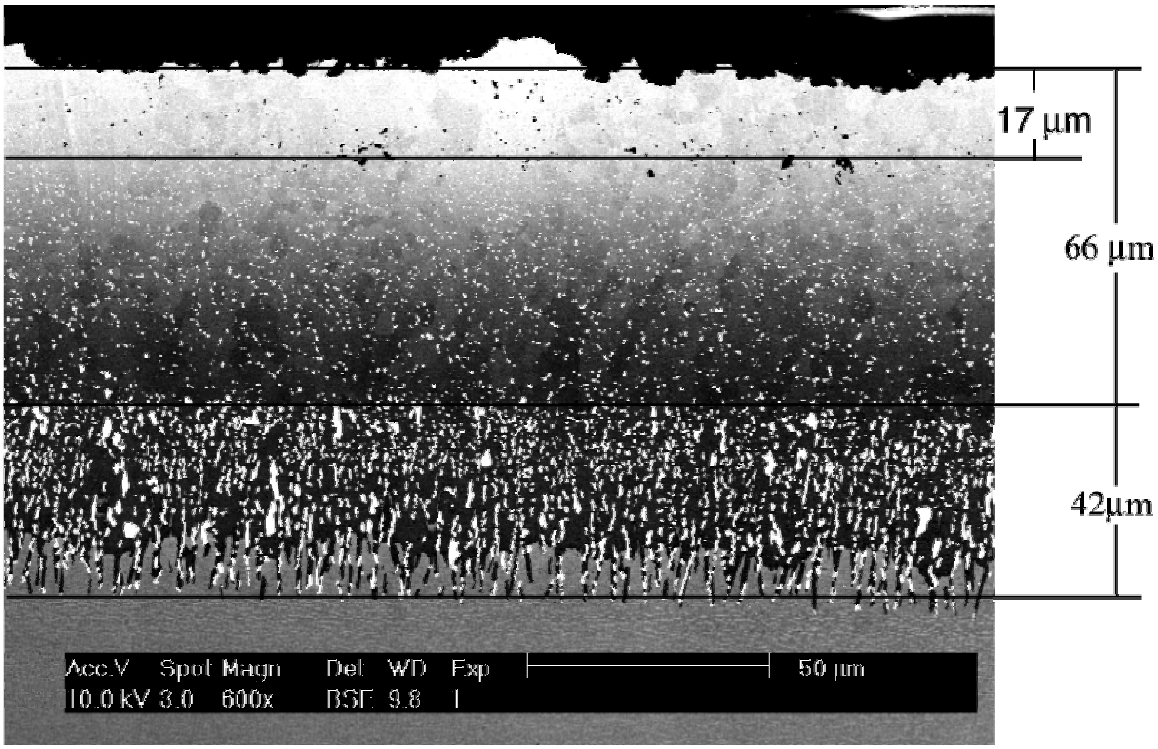

Figure 3.1: The as-coated PtAl bond coat system after a stabilizing vacuum heat treatment and without polishing of the outer surface.

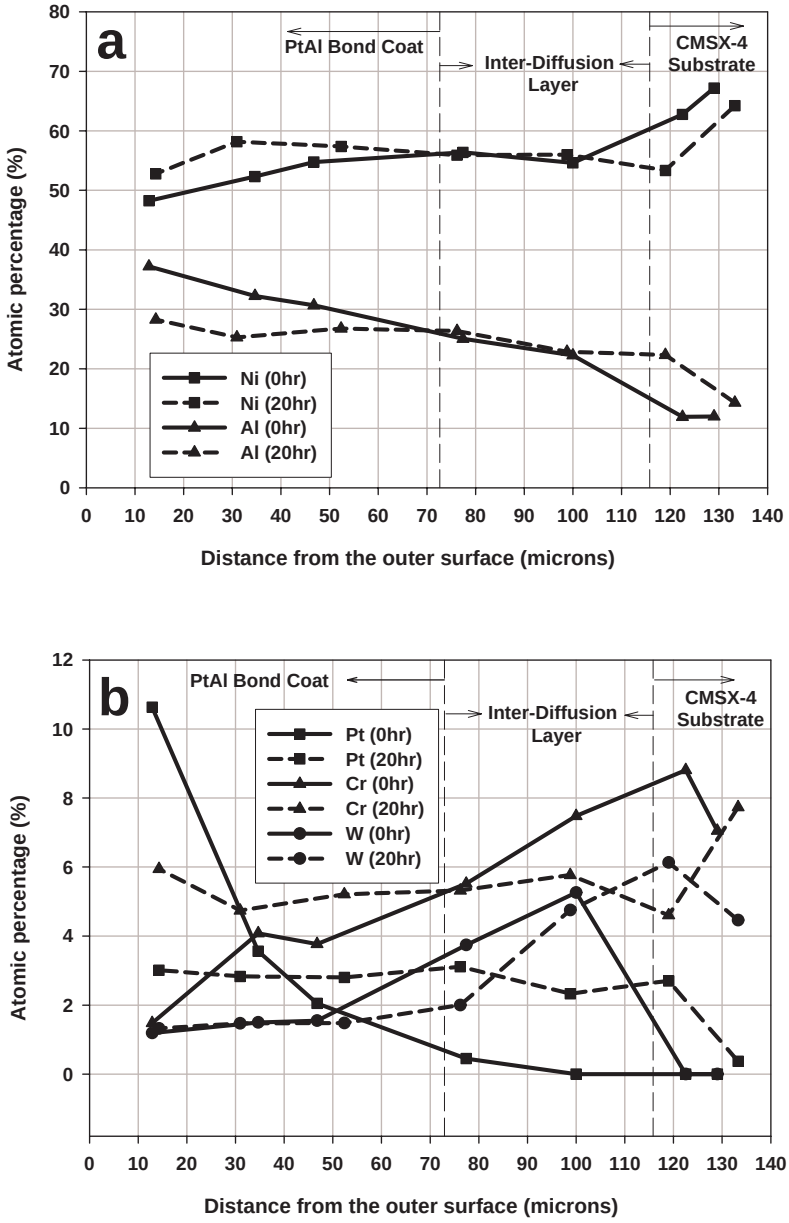

Figure 3.2: Nominal chemical compositions of an as-coated specimen and a 20 hour cyclic non-accelerated aluminum depletion specimen measured by energy dispersive spectroscopy line scans at increasing depths: (a) Ni and Al and (b) Pt, Cr, and W.

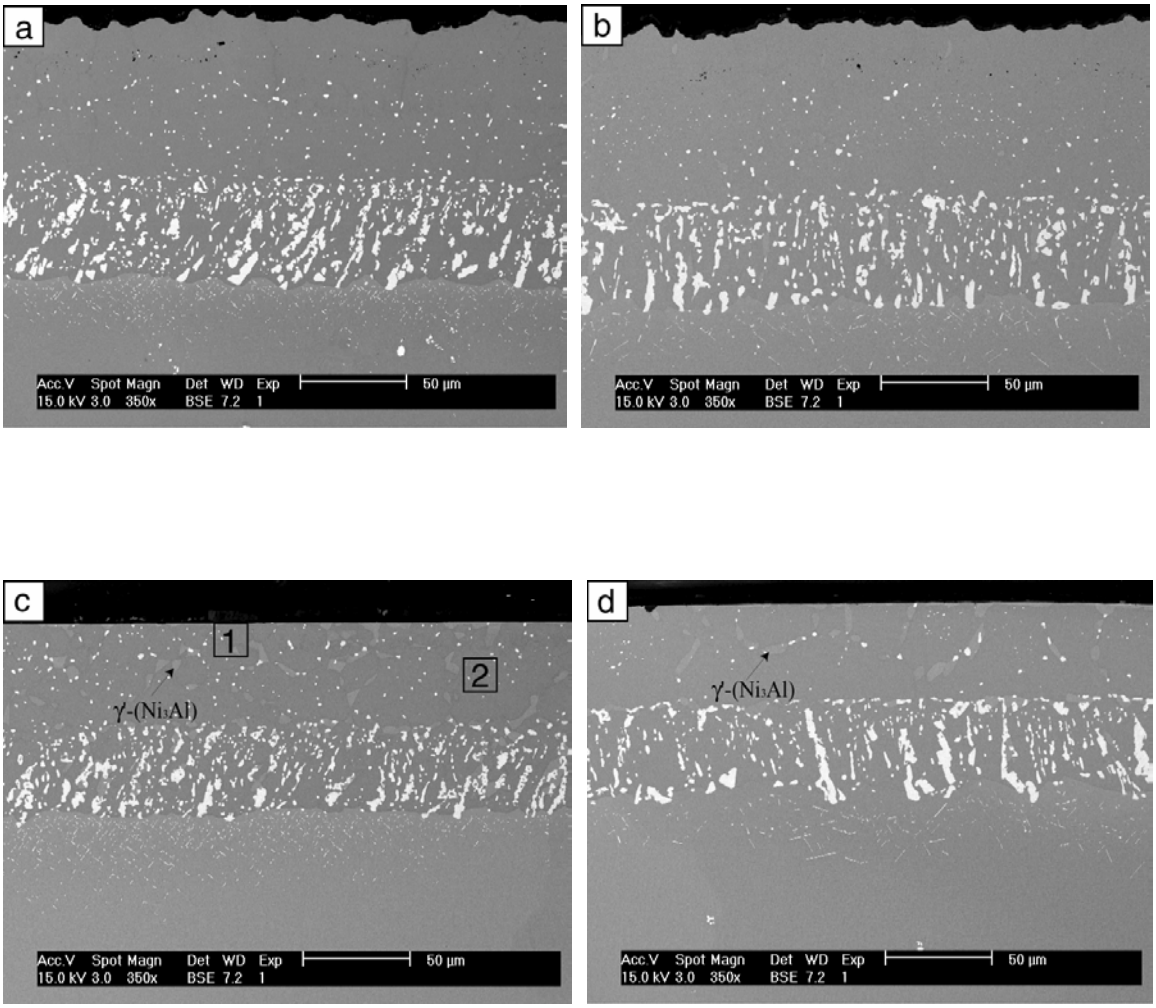

Figure 3.3: (a) A 20 hour cyclic non-accelerated aluminum depletion sample, (b) a 20 hour quasi-isothermal non-accelerated aluminum depletion sample, (c) a 20 hour cyclic accelerated aluminum depletion sample, and (d) a 20 hour quasi-isothermal accelerated aluminum depletion sample.

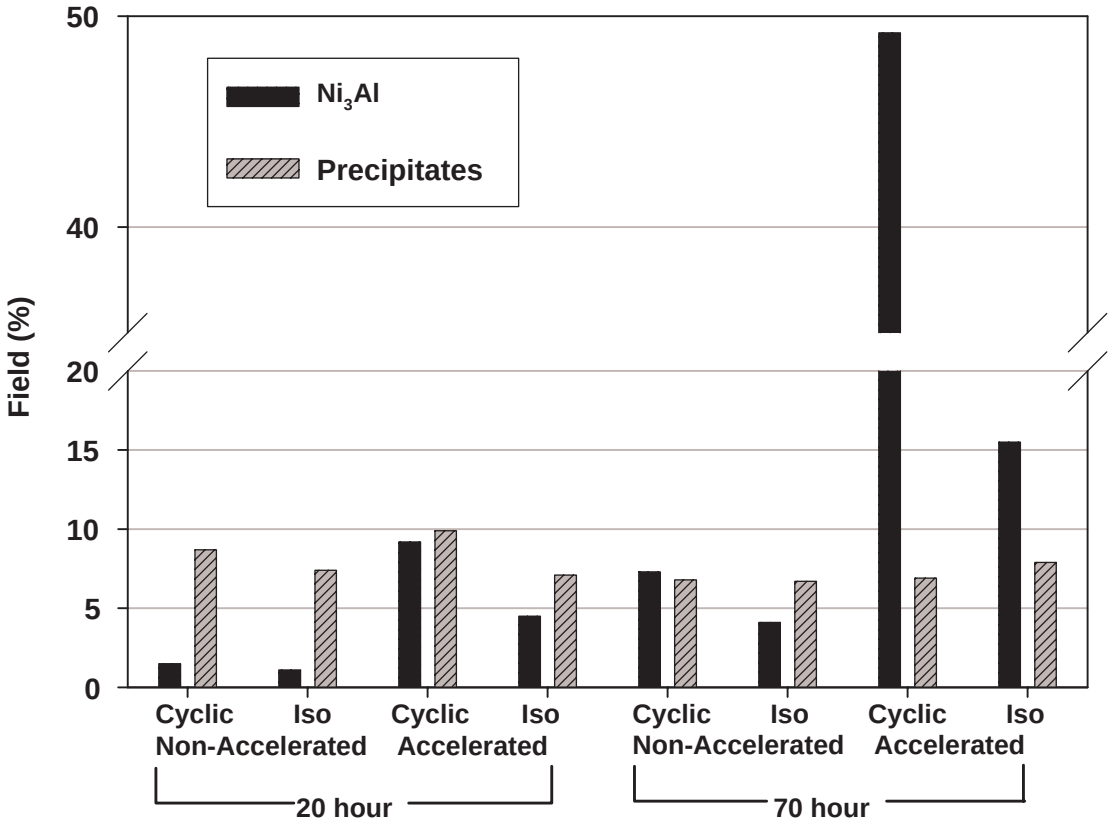

Figure 3.4: The results of grey-scale thresholding for quantification of γ'-(Ni_3Al) and precipitates percentages for 20 hour and 70 hour samples. The different γ'-(Ni_3Al) phase shapes for different heating types also support this observation.

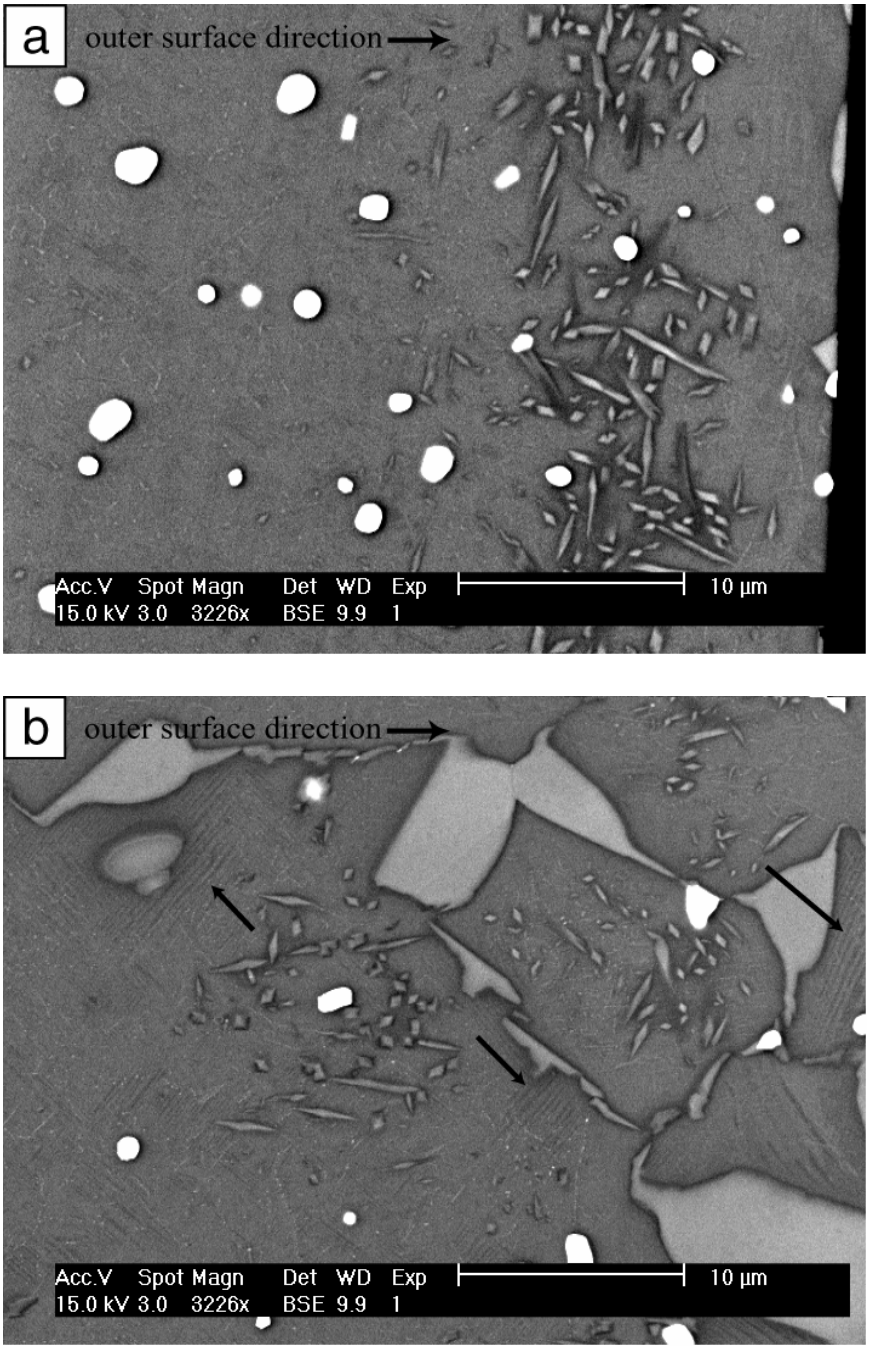

Figure 3.5: More detailed views of the bond coats of 20 hour cyclic accelerated aluminum depletion samples: (a) upper part (region 1 in Fig. 3.3c) and (b) middle part (region 2 in Fig. 3.3c).

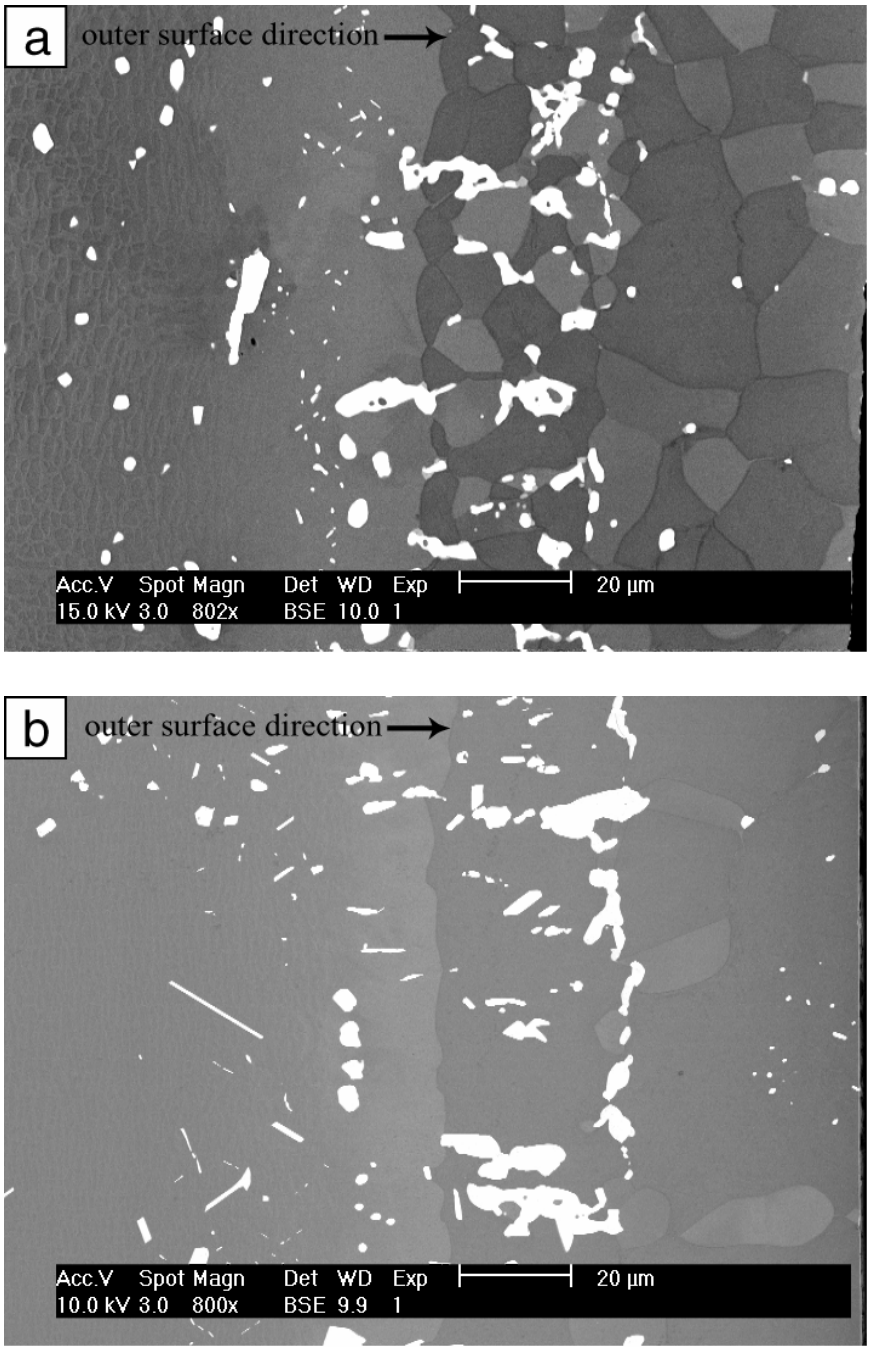

Figure 3.6: (a) A 70 hour cyclic accelerated aluminum depletion sample and (b) a 70 hour quasi-isothermal accelerated aluminum depletion sample.

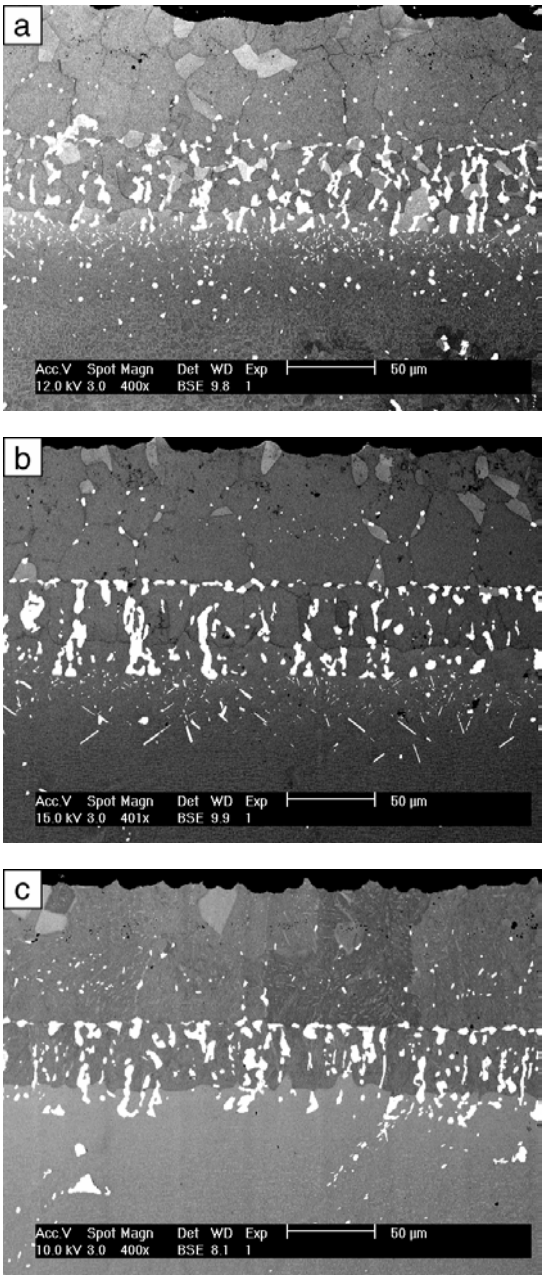

Figure 3.7: (a) An 80 hour cyclic non-accelerated aluminum depletion sample, (b) an 80 hour quasi-isothermal non-accelerated aluminum depletion sample, and (c) an 80 hour non-stop, true-isothermal sample.

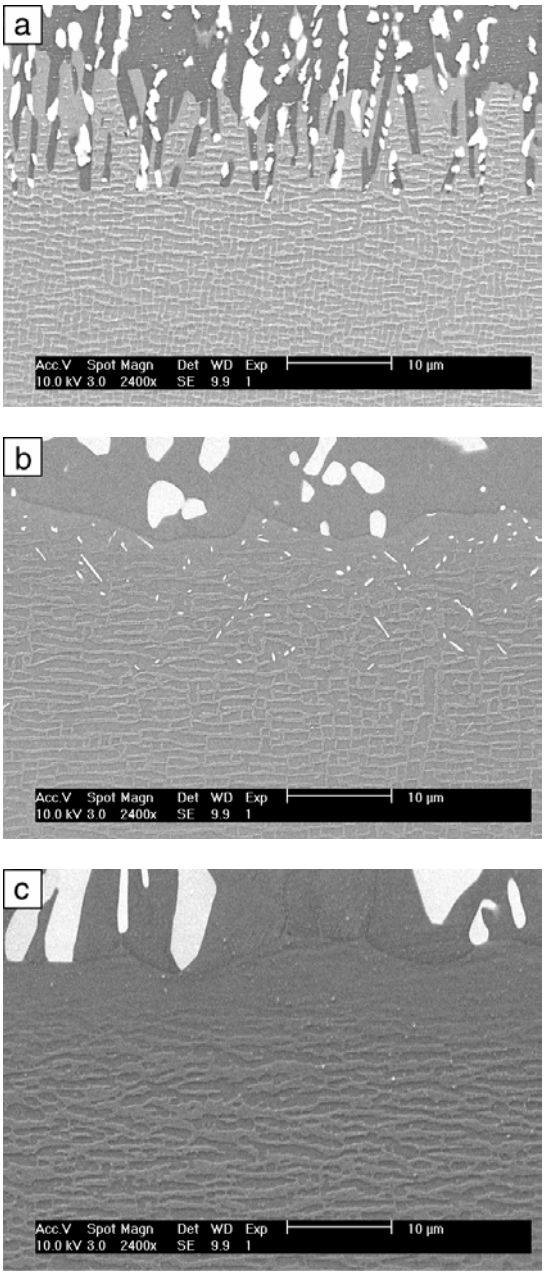

Figure 3.8: Detailed views of the substrate and inter diffusion layer of (a) an as-coated system, (b) a 10 hour cyclic non-accelerated aluminum depletion sample, and (c) a 10 hour isothermal non-accelerated aluminum depletion sample.

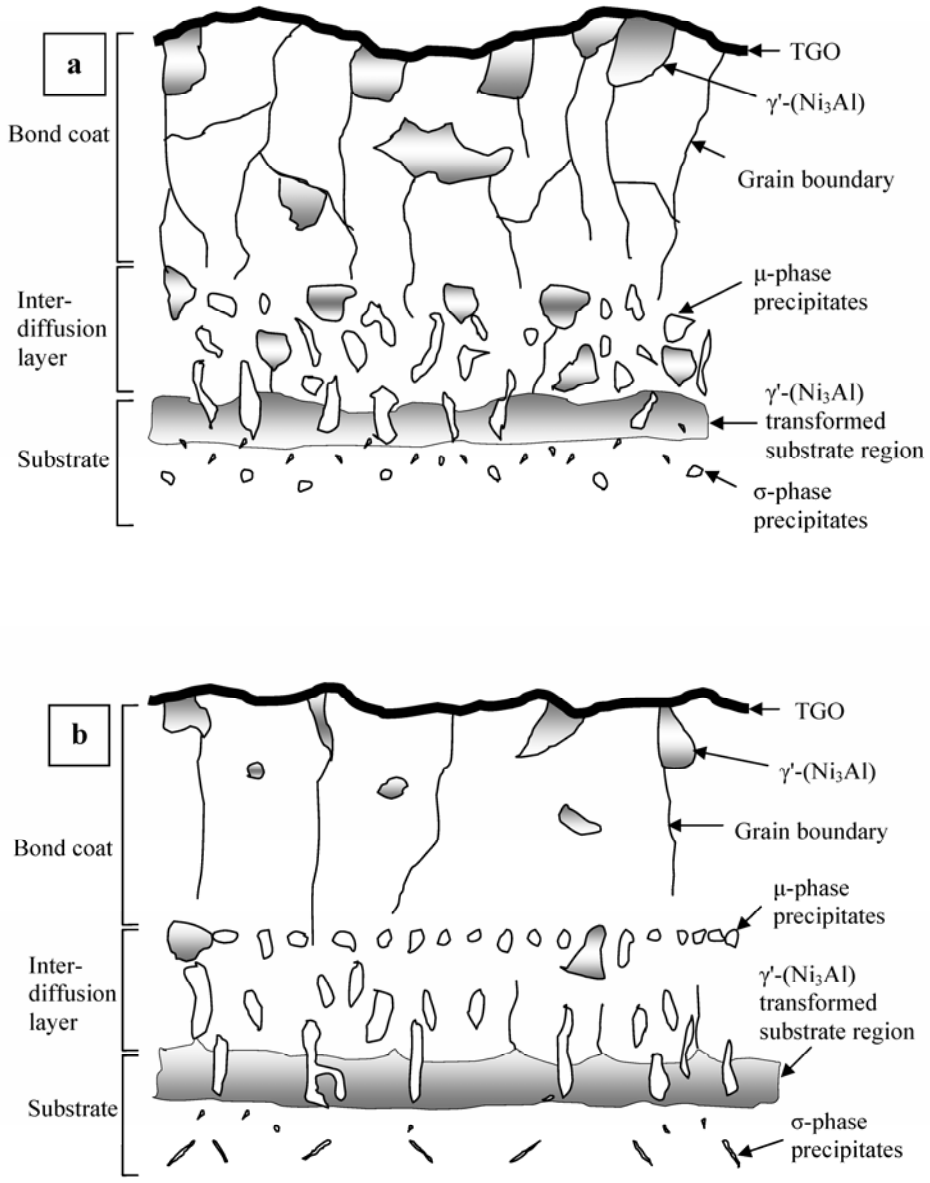

Figure 3.9: Schematic representation of the microstructure of various samples after 80 hours of heating: (a) the cyclic non-accelerated Al-depletion sample, (b) the quasi-isothermal non-accelerated Al-depletion sample, (c) the cyclic accelerated Al-depletion sample, and (d) the quasi-isothermal accelerated Al-depletion sample.

Figure 3.9 continued

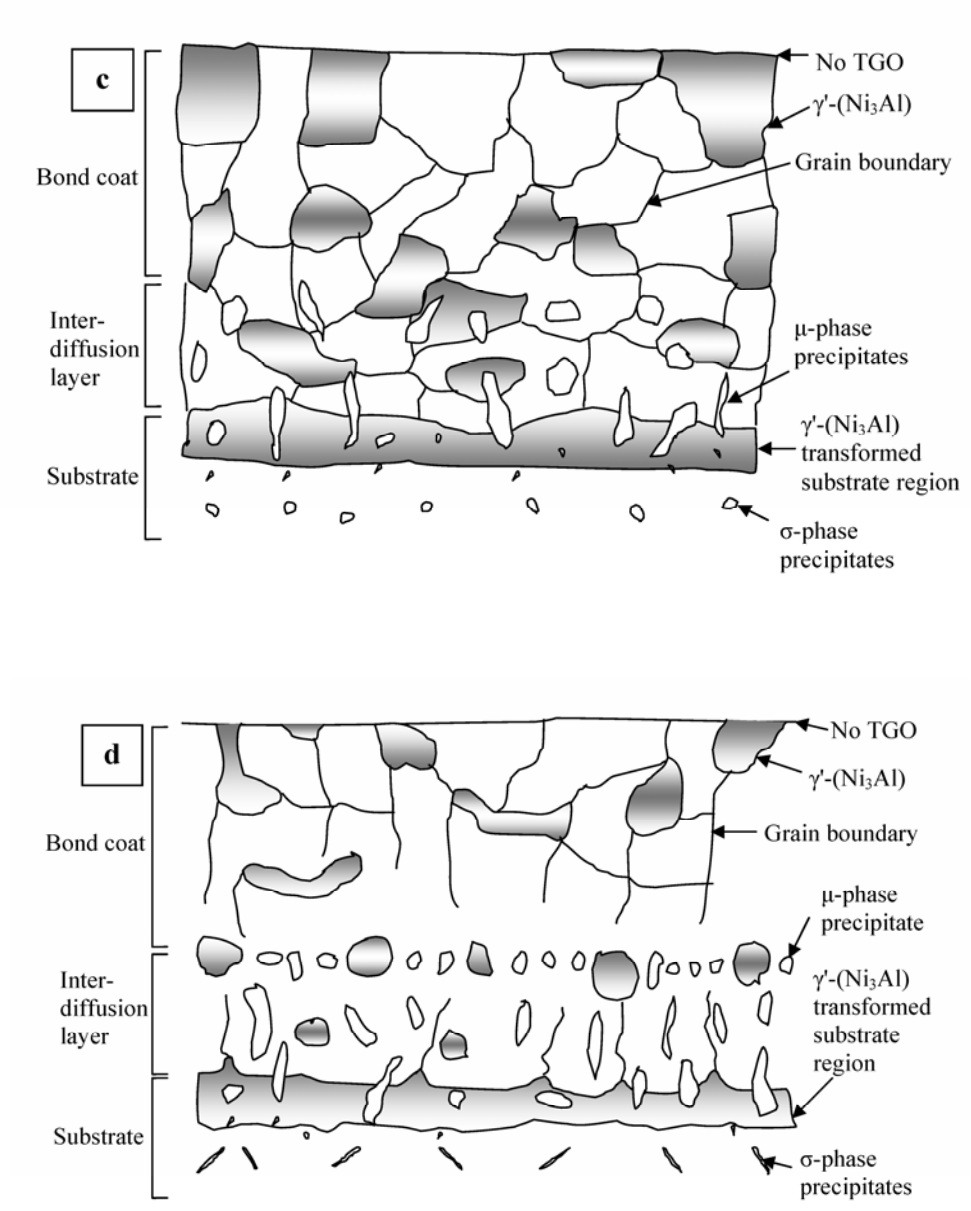

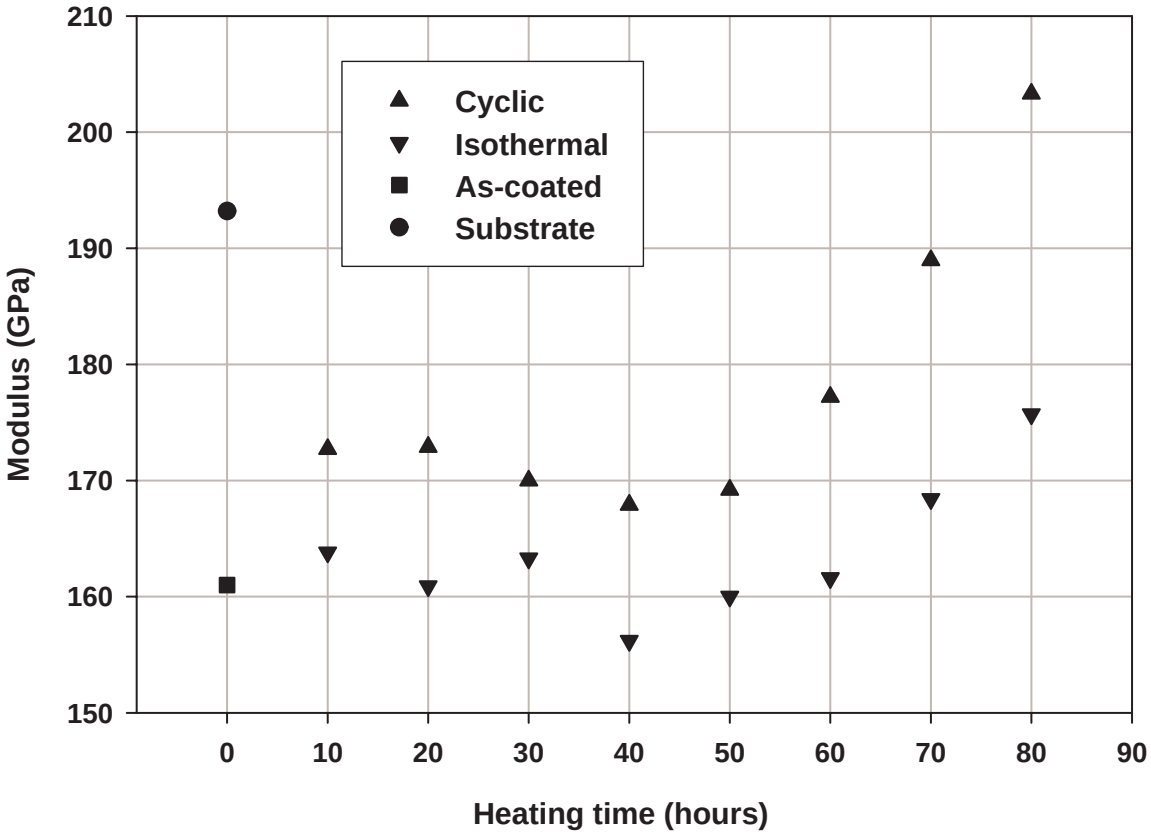

Figure 3.10: The moduli of an as-received substrate, an as-coated sample, and cyclic and quasi-isothermal accelerated aluminum depletion samples.

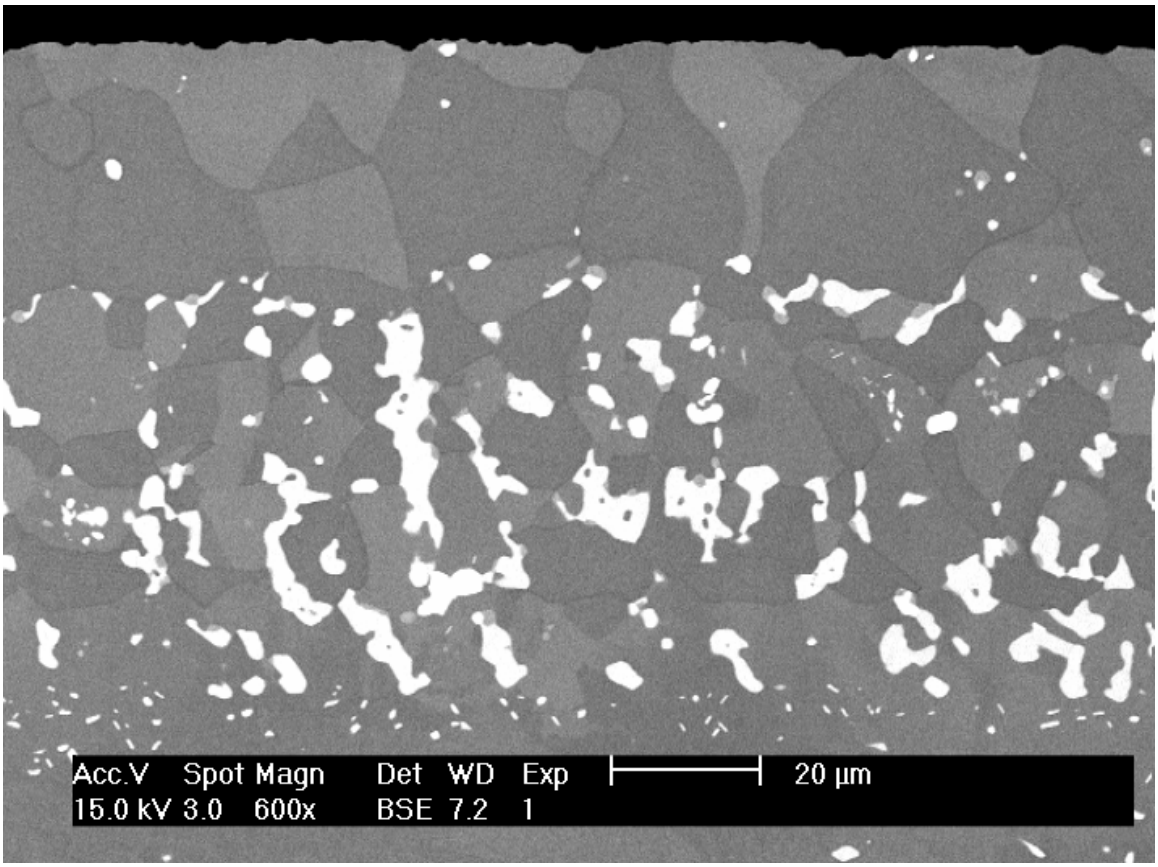

Figure 3.11: A typical image of a 60 hour cyclic accelerated aluminum depletion sample showing very high concentrations of γ'-(Ni_3Al) near the surface.

CHAPTER 4

ASSESSING THERMAL BARRIER COATING DAMAGE BY ACOUSTIC EMISSION ANALYSIS

1. INTRODUCTION

High temperature thermal cycling of thermal barrier coatings (TBCs) results in significant evolution of material microstructure. Thermally grown oxide (TGO) formation, bond coat degradation, and sintering of zirconia columns are three of the most prevalent evolving microstructures in TBCs. This microstructural evolution results in redistribution of stresses and damage, which ultimately leads to TBC spallation. Damage can happen at the top coat, TGO interface, and within the TGO layer. TGO growth causes further damage at the top coat - TGO interface and within the TGO layer by generating significant compressive stresses during cooling cycles [18, 20, 93]. Bond coat degradation includes γ'-(Ni_3Al) and martensitic phase transformations [24-26] and contributes to damage formation at the TGO interface and within the TGO layer mostly

by promoting TGO layer waviness [20, 33]. Sintering of top coat columns causes damage accumulation in the top coat and at the top coat-TGO interface by reducing the strain tolerance of the top coat [30].

As was already mentioned, damage in TBCs appear as cracks at the top coat-TGO interface and within the TGO layer. Cracks at the TGO interface are most critical since TBC spallation is initiated by cracks at the TGO interface [2]. The most recent mechanistic model of TBC failure postulates the existence of sub-critical cracks prior to macroscopic spallation [23]. Sub-critical cracks at the top coat near the TGO interface eventually link together and create conditions for macroscopic spallation. After the top coat becomes sufficiently debonded by interface cracks, TBC spallation results from buckling of the top coat during cooling cycles [94]. In-plane compressive stresses in the TGO layer are the result of coefficient of thermal expansion (CTE) mismatches at the TGO interface and TGO swelling during TGO formation [48]. These compressive stresses are the driving forces behind interface cracking and buckling.

Detection of cracks makes it difficult to verify the applicability and accuracy of models for sub-critical cracking in TBCs. Because sub-critical interface cracks form and grow beneath the opaque yttria stabilized zirconia (ZrO_2 with 7% Y_2O_3 or YSZ) and

the size of sub-critical cracks is postulated to be about 10-50 μm [6], the conventional way to detect sub-critical cracks is to section the specimen. This destructive sectioning is limited because of the difficulties in locating damage and the inability to distinguish between pre-existing defects, active damage, and damage caused by sectioning. If the transition from sub-critical cracking to critical cracks at the TGO interface is known in advance, catastrophic TBC failure could be predicted. It would also be valuable to understand how microstructural evolution is linked to damage in TBCs. Ideally this analysis of damage would take place for the entire TBC life.

To aid in analyzing the effect of TBC microstructural evolution on TBC damage, acoustic emission (AE) is monitored during thermal cycling. AE is a mechanical wave that is produced by rapid strain energy release [62], and can be generated during dislocation motion, phase transformation [63], crack formation [64], crack propagation [64], and other microstructural events. Damage detection in TBC specimens during indentation and scratching has been analyzed by the AE technique [65]. The TBC top coat cracking behavior under four point bending load was examined by measuring AE [66]. AE techniques have also been used to detect cracking activity in TBC specimens [67, 68]. Thermal fatigue failure of TBC specimens was monitored by

AE techniques [69]. As compared to AE from phase transformations, it was found that higher AE energy counts and cumulative counts were associated with macro-crack initiation and growth in TBCs [68].

This dissertation research has found that TBCs produce AE during thermal cycling. At this point, the AE analysis is not capable of identifying the type of damage or of locating damage spatially. However, AE detection is useful for its temporal resolution. With the current information base on microstructural evolution and on failure mechanisms in TBCs, the sources of AE and locations of damage can be postulated.

2. AE DETECTION EXPERIMENTS WITH A WAVEGUIDE WIRE

2.1 PROCEDURE

An experimental setup using a box furnace and a motion control system has been built and is schematically shown in Fig. 4.1. Fast heating and cooling are accomplished by moving the specimen in and out of a furnace with a stepper motor driven motion control system. The results given in this chapter are for a TBC specimen held in the furnace for 20 minutes at 1200 °C and out of the furnace for 23 minutes.

Compressed air aids in cooling of the specimen. AE is detected by a piezo transducer coupled to the specimen surface. A Vallen ASMY4 AE System samples the voltage signals from the piezo transducer and records signal characteristics such as threshold crossings, rise-time, amplitude, and energy. For high temperature applications, since the sensor has limited temperature capability, it is necessary to couple the specimen to the transducer through a waveguide. One type of waveguide is a nickel-chrome alloy resistance heating wire which is spot welded to the TBC specimen and to a steel blank where the AE sensor (Deci SE150-M) is attached. AE will propagate through the waveguide. The Vallen ASMY4 AE System is used to continuously monitor and record AE signals throughout the heating and cooling cycles. Another type of waveguide uses a solid alumina rod with a mechanism that contacts the specimen during the out-of-the-furnace cooling stage.

To resolve damage spatially and provide information about damage sources, images of the TBC top coat during cooling cycles were captured by a charge couple device (CCD) camera as shown in Fig. 4.1. A fiber optic light source is orientated almost parallel to the top coat surface for better surface contour resolution. In Chapter 6, it will

be described how captured images were used to investigate top coat and TGO interface damage and the propagation of the catastrophic spallation.

The thermal cycling rig shown in Fig. 4.1 is fully automated. The motion of the specimen is controlled by a program in the stepper motor controller. Limit switches are used to activate different parts of the control program, to turn on the cooling air, and to trigger the frame grabber for image acquisition. The AE system runs continuously, and therefore with the wire waveguide, heating, holding, and cooling AE are recorded for the entire life of the TBC.

2.2 AE RESULTS

2.2.1 AE Event Calibration

Figure 4.2 shows two typical thermal cycles with the maximum amplitude for each AE event. Each AE event represents a crossing of an arbitrarily set voltage threshold. The AE events shown in Fig. 4.2 are a mixture of AE from the TBC specimen and the wire waveguide. Also, the starting and ending of each heating and cooling periods have many AE events generated during the apparatus used to move the specimen in and out of the furnace. AE from the TBC specimen is believed to emanate from the

top coat, TGO interface, and TGO cracking. The AE events from the wire are most likely from oxidation. Wire-only tests have been done to determine the level of AE activity from just the wire. The wire-only tests generated almost no AE with amplitudes higher than 70 db. Therefore a 70 db threshold was used as a cut-off value to filter out AE events from the wire.

The cycles in Fig. 4.2 shows significant activity during cooling, minor AE events during heating and little or no activity during holding. Typical events emanating from the top coat include the following: contact between the columnar top coat grains resulting from compressive CTE mismatch stresses during cooling and from TGO growth stresses, separation of columnar top coat grains during heating and holding, and vertical cracking of sintered top coat microstructures. Within the TGO, the CTE misfit stresses are compressive during cooling, and TGO growth stresses are also compressive. Thus from the TGO and the TGO interfaces, AE activity would result from interface [6] and oxide cracking [95]. Bond coat phase transformation may cause AE events which are low energy events [68].

Heating and holding AE events are expected to be relatively low energy events. Therefore, significant numbers of AE events during the cooling period are

thought to be primarily related to damage at the top coat - TGO interfaces and within the TGO itself. An additional complicating factor is related to the loss of stiffness of the alloy wire waveguide at high temperatures. The alloy wire may not be transmitting AE as well at high temperatures.

2.2.2 AE Events During TBC Life

AE events throughout the TBC life were explored with three samples. Figure 4.3 shows the normalized cumulative AE events during cooling portions of each cycle. AE events were analyzed only during cooling portions of each cycle because most critical damage occurs during cooling cycles. To calculate the cumulative AE events, for the 23 minutes of cooling, AE events with an amplitude over 70 db were counted. The cumulative AE events were normalized by dividing the cumulative AE events for each cooling cycle by the average number of cumulative AE events for each cycle from 120 to 200 where all three AE tests generated no significant AE activity. This normalization procedure caused the results from all three samples to line up at "1" in what will be called "Region 2." The AE Test1 (AE1) and AE Test3 (AE3) specimens failed during one of the cooling cycles. The AE Test2 (AE2) specimen failed during repair of the waveguide wire. The AE1 specimen was a specimen that had been exposed to 1000 °C for 300 six

minute cycles. Given the relatively low maximum temperature and the short duration of the cycles, it was assumed that the AE1 specimen would behave like an as-received specimen. As mentioned in Chapter 1, sintering is not significant even after 1000 one hour cycles at 1100 °C cycles [38]. Therefore, sintering after 300 six minute 1000 °C cycles would be negligible. The AE2 and AE3 specimens had never been cycled. The results in Fig. 4.3 indicate that there are four distinct regions of AE activity during the life of a TBC. Although it is common for AE results to vary widely from one experiment to another, there is excellent consistency between the three experiments. The variability in the fourth region is expected since small differences in microstructure and in handling the specimen will be very critical in this region. Table 4.1 categorizes each region's AE event characteristics and possible causes of the AE events.

The first region is from the initiation of cycling to around the 120^{th} cycle. This period generates significant AE events. Such large numbers of earlier-cycle AE events have also been reported in other coatings [67, 68]. Before sintering, the EB-PVD YSZ top coat microstructure has distinctive feathery features and intercolumnar gaps [41]. After relatively short thermal exposure, the feathery features sinter together and create necks between columns [41]. TGO growth is known to be parabolic or nearly-parabolic

in nature [4, 27-29] and therefore during this period, TGO grows rapidly. The compressive stresses in the TGO layer increase as the temperature reduces. This compressive force in the TGO layer creates room temperature convex curvature of the TBC specimen during cooling cycles. Evidence of this curvature will be presented in Chapter 5. This convex curvature is accommodated by intercolumnar gaps in the YSZ top coat. When the top coat has experienced sintering, the gap formation requires that intercolumnar necks fracture. Therefore, the main source of the cooling cycle AE events in this first region may result from top coat vertical cracks and fracture of intercolumnar necks. It has been observed that interface crack nucleation does not occur before 34% of the TBC's life [3] and oxide cracking was not observed before 50 one hour cycles at 1200 °C [20]. Therefore it is not expected that interface cracking and oxide cracking are active in the first region.

The second region is from around the 120th cycle to the 200th cycle. In this period, there are few significant AE events. Because TGO growth follows a parabolic pattern, TGO growth slows down rapidly during this period. This reduction in TGO growth rate halts TBC convex curvature formation. Also, the waviness [20, 72] of the TGO layer caused by bond coat degradation plays an important role in reducing TBC

convex curvature by relieving in-plane compressive stresses in the TGO layer. TGO growth and TGO layer waviness are two competing factors which determine the degree of TBC convex curvature. It seems that during this period, TGO layer waviness becomes more dominant, thus also reducing the TBC's convex curvature. In Chapter 5 it will be shown experimentally that curvature decreases in Region 2. It has reported that extensive sintering has occurred after 50 hours of 1200 °C isothermal heating [40, 41]. This extensive sintering may prevent top coat columns from forming additional vertical cracks. Therefore the vertical cracking of the top coat is not active in Region 2.

The third region is from around the 200^{th} cycle to the 270^{th} cycle. During this period, AE events slowly increase. This region's AE events may be the result of TGO interface crack nucleation. The now thicker TGO is under high compressive stresses and oxide cracking at or near the ridges in the TGO wrinkles occurs to relieve these stresses [95]. Therefore TGO interface crack nucleation and oxide cracking may create AE events during this period.

The fourth region is from around the 270^{th} cycle to failure. During this period, AE activity increases rapidly. Sub-critical crack extension at the top coat near the TGO interface is believed to cause the AE events. Through specimen sectioning sub-critical

crack extension has been observed starting at approximately 76% of the TBC's life [3]. During this region, oxide cracking may be more prevalent and therefore also contribute more significantly to the AE event counts. With each passing thermal cycle, video images show that undulations in the top coat become more visible. Within just a few cycles before complete TBC spallation, sudden increase in undulation size appeared in the top coat surface images. After this point, the undulations become obvious even with bare eyes. The size increase of undulations seemed to occur through merging of adjacent undulations [72] and small scale buckling. This sudden size increase could indicate intensive interface crack extension/coalescence. The sudden change in the undulation size is coincident with the sudden AE event increase in AE3 at around the 420th cycle. Therefore, the later part of this period's AE events may be the result of extensive interface crack coalescence and extension.

The AE2 specimen failed during the sanding of the bottom of the substrate. During the sanding process, a sheer force was applied on the top coat parallel to the TGO interface. This may indicate that from around the 270^{th} cycle, the failure of TBC could occur at any moment and is very unpredictable, especially when external forces are applied to the TBC.

3. AE DETECTION EXPERIMENTS WITH A WAVEGUIDE ROD

AE analysis with a wire waveguide showed that there are four distinct regions of AE activity during the life of a TBC. However, AE detection with a wire waveguide has several limitations. As mentioned in Sec. 2.2.1, it is believed that oxidation of the waveguide wire generated AE. For this reason it was necessary to use a 70 db threshold to filter out AE events from the wire. Therefore, lower amplitude AE events which may have significance were excluded from the analysis. In addition, the spot welding process damaged the specimens, thus to affecting the TBC life. An additional complicating factor is related to the loss of stiffness of the alloy wire waveguide at high temperatures. The alloy wire may not be transmitting AE as well at high temperatures. Despite these limitations, the results presented in the previous section show very good consistency through Region 3.

To investigate AE events in more detail and to enable other interrupted-test investigative measures, the AE detection method needed to be altered. This could only be accomplished by using a waveguide that was not permanently attached. Since only cooling portions of the cycles are being investigated, it was decided to use an alumina rod outside the furnace to make contact with the specimen. Alumina was chosen because it

will not oxidize, is stability at high temperature, and has a high elastic modulus. The AE analysis is thus simplified by keeping the waveguide at lower temperatures and by removing the possibility of spot weld generated damage. An additional benefit of not spot welding wires onto specimens was the ability to periodically use other nondestructive means to study the specimens. For example, a profilometer could now be used to probe curvature and roughness change of the TBC systems. SEM could also be used to look at top coat cracking/damage as a function of the number of cycles. The results from profilometer and SEM analysis will be discussed in detail in Chapters 5 and 6.

3.1 PROCEDURE

Figure 4.4 shows how the alumina wave rod was incorporated into the thermal cycling rig. As was the case for the wire waveguide AE detection experiments, the TBC specimen was held in the furnace for 20 minutes at 1200 °C and out of the furnace for 23 minutes. The alumina waveguide rod was incorporated by placing a custom made frame and mechanism just below the bottom face (the substrate side) of the TBC specimen in the cooling position. A fan aids in cooling of the specimen.

The frame and mechanism for the waveguide rod is as follows. The alumina wave rod is a 0.25 inch diameter long cylinder shape. The top side of the wave rod contacts the bottom face of the specimen during cooling cycles. The bottom of the specimen is sanded smooth so that there is good contact between the waveguide rode and the specimen. The bottom side of the wave rod is bonded to a Deci SE150-M AE sensor which is housed in a sensor holder. A cam contacts the bottom of the sensor holder and every 180 degree rotation of the cam creates contact and release between the specimen and the alumina rod/sensor assembly. The cam is controlled by a circuit with a 12 VDC motor, switches, and a relay. The circuitry is linked to the motion control circuitry for moving the specimen in and out of the furnace. As was the case for the *wire* waveguide setup, the waveguide *rod* setup is fully automated for continuous cycling. The only difference is that meaningful AE is collected only after the waveguide rod has contacted the specimen in the cooling position. More details of the mechanism and its circuitry are provided in Appendix 1.

For specimens that were investigated with profilometry and SEM, the TBC top coat was carefully polished by using 400, 600, 1000, and 2000 grit sand papers. Thermal cycles with AE detection were interrupted regularly to measure curvature and roughness

and to take SEM images of the top coat. As mentioned earlier, these curvature and SEM results are presented and discussed in Chapters 5 and 6.

3.2 AE RESULTS

Four new experiments with the alumina waveguide rod were done to further explore cooling cycle AE events throughout the TBC's life. Figure 4.5 shows the normalized cumulative AE events of the four *new* experiments (N-AE1, N-AE2, N-AE2, and P-AE1). The specimen designated P-AE1 was a polished specimen that was also used for profilometry and SEM. One wire waveguide AE detection experiment, AE3 in Fig. 4.5 was also included for comparison purposes. To calculate the cumulative AE events of the four new AE experiments, each AE event with an amplitude of 40 db or above during the 23 minutes of cooling was counted. Recall that the wire waveguide experiments included only AE events that were higher than 70 db. The cumulative AE events were normalized by dividing the cumulative AE events for each cooling cycle by the average number of cumulative AE events for each cycle between 120 to 200. All specimens except for the N-AE2 specimen failed during the cooling cycle of the thermal loading tests. The N-AE2 specimen failed during an extended time at room temperature while apparatus was being adjusted.

As was the case in the wire waveguide AE detection experiments, results in Fig. 4.5 indicate that during the life of TBCs there are four regions of AE activity. The new method for transmitting AE to the sensor and the lower cut-off amplitude for the new experiments did not change the general trends found in the AE. Nonetheless, using the waveguide rod did increase the life of the specimen and enabled the collection of periodic profilometry and SEM information.

Generally speaking, the beginning and end of region 1 and region 2 are more easily identified as compared to region 3 and region 4. Region 3 starts somewhere after the 200^{th} cycle. However, the length of region 3 ranges from a maximum of around 450 cycles to a minimum of around 170 cycles. Region 3 is believed to be where interface crack nucleation happens. This is expected to be a highly stochastic process and therefore there is more variability in its duration. Region 4 is believed consist of crack coalescence and small scale buckling. Region 4 has rapid AE event increase and spallation of the TBCs eventually happens after around 50 to 100 cycles from the start of Region 4. Since region 4 is relatively consistent in its duration, it can be concluded that the life of the TBC is determined by the stochastic events in region 3. Furthermore, damaged caused by specimen handling and in particular by spot welding of wire

waveguides would certainly shorten the length of region 3 and cause a shorter overall TBC life.

The failure of N-AE2 indicates that the length of the cooling period may have significant influence on TBC life. As mentioned above, N-AE2 was left at room temperature for much longer than the usual 23 minutes. The residual stress state at room temperature appears to have caused the specimen to fail. The influence of cooling period duration (or room temperature dwell time) is expected to be significant only when the TBC is already in region 4. Nonetheless, this phenomenon could warrant further investigation.

3.3 EARLY LIFE AE CHARACTERISTICS

As shown in both wire waveguide and alumina rod waveguide AE detection experiments, early cycles of the TBC life have significant number of AE events. With the rod waveguide, it was possible to use a lower cut-off threshold, and these early cycle AE activities were identified. Figure 4.6 shows the 4^{th} to 12^{th} thermal cycle AE events in N-AE2. As was mentioned earlier, the starting and ending of each heating and cooling periods have a wide range of AE events from vibration of the cycling rig mechanism and rod waveguide mechanism. The red lines and the green lines represent the starting and

ending of the cooling cycles, respectively. Thus AE events along the red and green lines are the noise from the cycling rig mechanism and wave rod loading frame. There are no AE activities during the 4th cooling cycle. As indicated in Fig. 4.6, the early cycle AE activities start from around the 5th cooling cycle and become more obvious during the 6th cooling cycle. The early cycle AE activities decreased after the 15th cooling cycle and decreased further after around the 24th cooling cycle.

These early cycle AE events happen in a unique pattern. Figure 4.7 shows the 1st AE event occurrence time from the 6th to 24th cooling cycles for three AE experiments with the wave guide rod AE detection. As shown in Fig. 4.7, the 1st AE event occurrence time decreases as the cycle number increases. The 1st AE event occurrence time decreases more rapidly for first few cycles and more gradually for the later cycles. The manner in which the 1st AE event occurrence time decreases with increasing numbers of cycles seems to be linked to how the room temperature curvature of the TBC changes. This would suggest that these early AE events are related to vertical cracking and the fracture of intercolumnar necks. It is also noted that within each cycle, the curvature development is slow to develop for the earliest of cycles and fast for later cycles. As will

be shown in Chapter 5, curvature is "locked-in" after the first 32 cycles. AE activity decreases after the curvature has stabilized.

4. CONCLUSION

AE experiments with two different methods for collecting signals from high temperature specimens have been performed. One method used a wire waveguide and the other used a waveguide rod. Results were presented primarily in the form of normalized AE events during cooling versus numbers of cycles. Four regions of AE activity were identified.

Despite the different methods for collecting AE and despite the normal variation in the specimens, the results showed excellent consistency in regions 1 and 2. Spot welding the wire waveguide is suspected of causing damage to the TBC specimens. However, spot welding damage did not significantly affect the AE event characteristics in regions 1 and 2. Regions 1 and 2 AE event characteristics seem to be determined by TBC curvature and are influenced primarily by microstructural evolution. Since there is no indication of interfacial cracking in regions 1 or 2, TBC failure (spallation) is not expected in this region.

Regions 3 and 4 are affected considerably by handling damage. All of the alumina rod waveguide experiment specimens survived longer compared to wire waveguide experiment specimens. The waveguide rod specimens also had much more variability in their lives. In particular, the length of region 3 seems to be statistical in nature and is seriously affected by handling damage. The length of region 3 damage is most significant in determining the overall TBC life. Handling damage seems to hasten the transition from region 3 to region 4 and accelerate the TBC spallation drastically.

Region	Cycles	AE Events	AE source/Damage
1	1^{st} - 120^{th}	Increasing	Top coat vertical crack formation and intercolumnar neck fracture due to TBC convex curvature
2	120^{th} - 200^{th}	Constant	Diminishing of TBC convex curvature
3	200^{th} - 270^{th}	Slowly increasing	Interface crack nucleation and oxide cracking
4	270^{th} - failure	Rapidly increasing	Interface crack extension and oxide cracking

Table 4.1: AE event and source descriptions for each stage of the TBC life cycle.

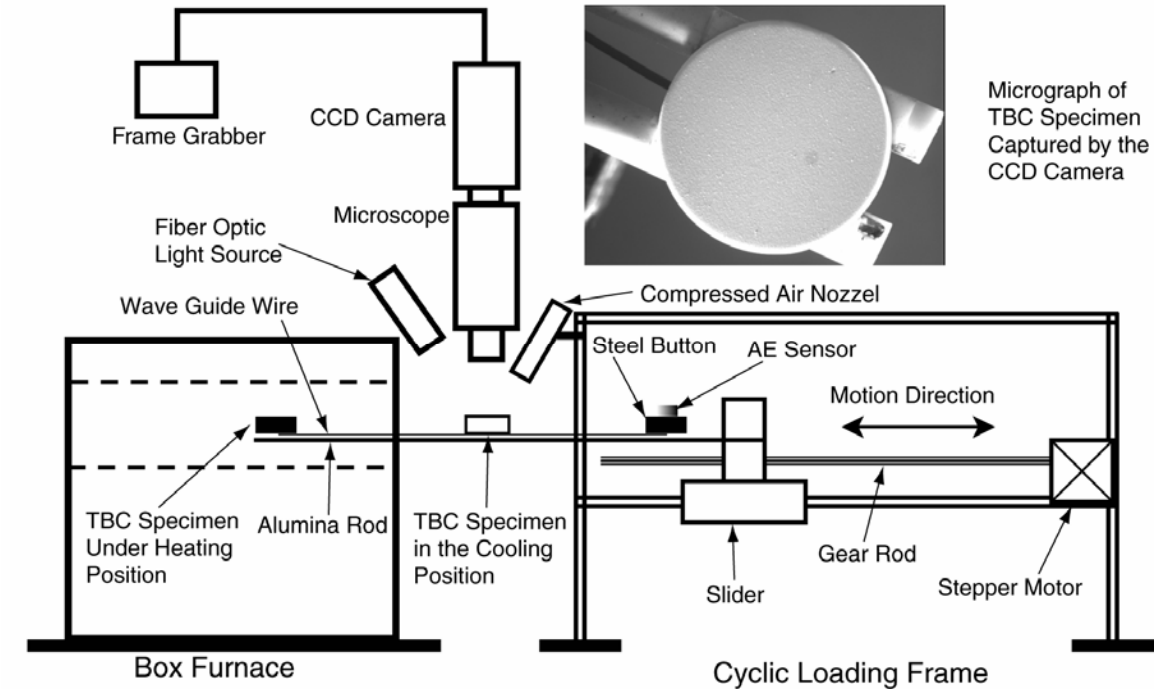

Figure 4.1: A schematic of the thermal cycling apparatus for *in situ* AE detection and top coat surface image capture.

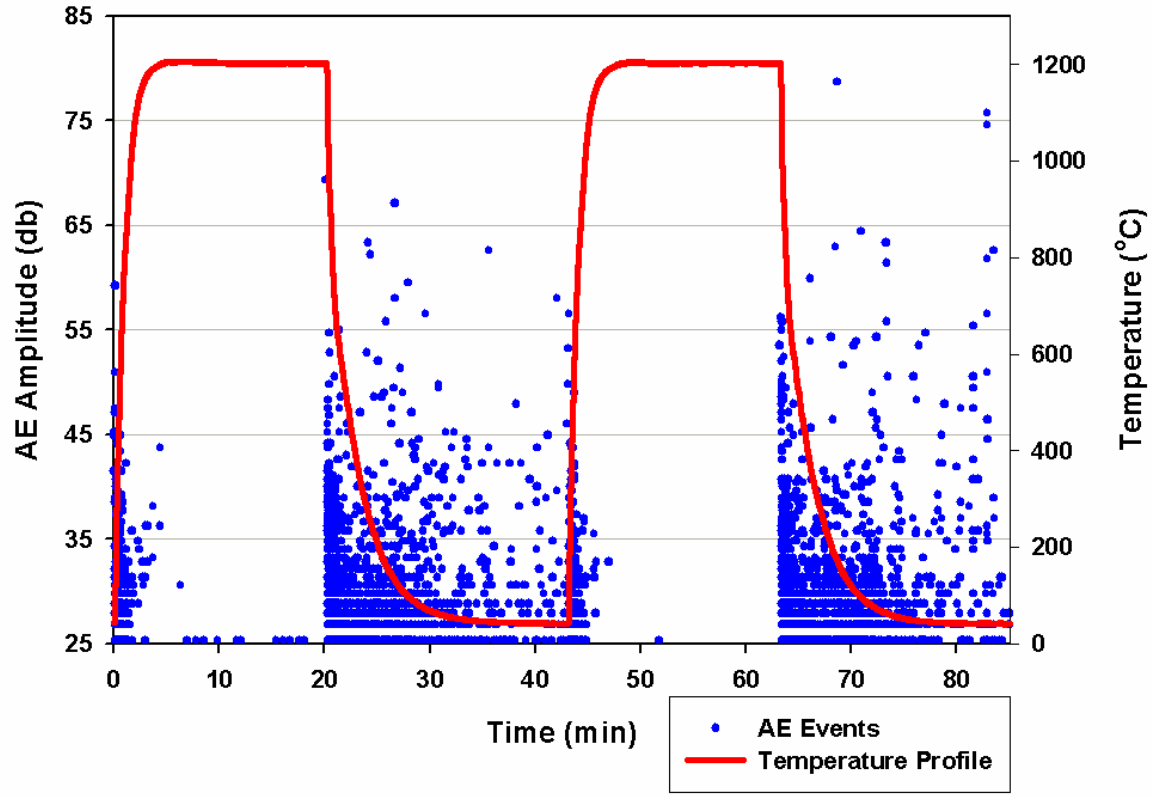

Figure 4.2: Two thermal cycles showing AE events and the temperature profile.

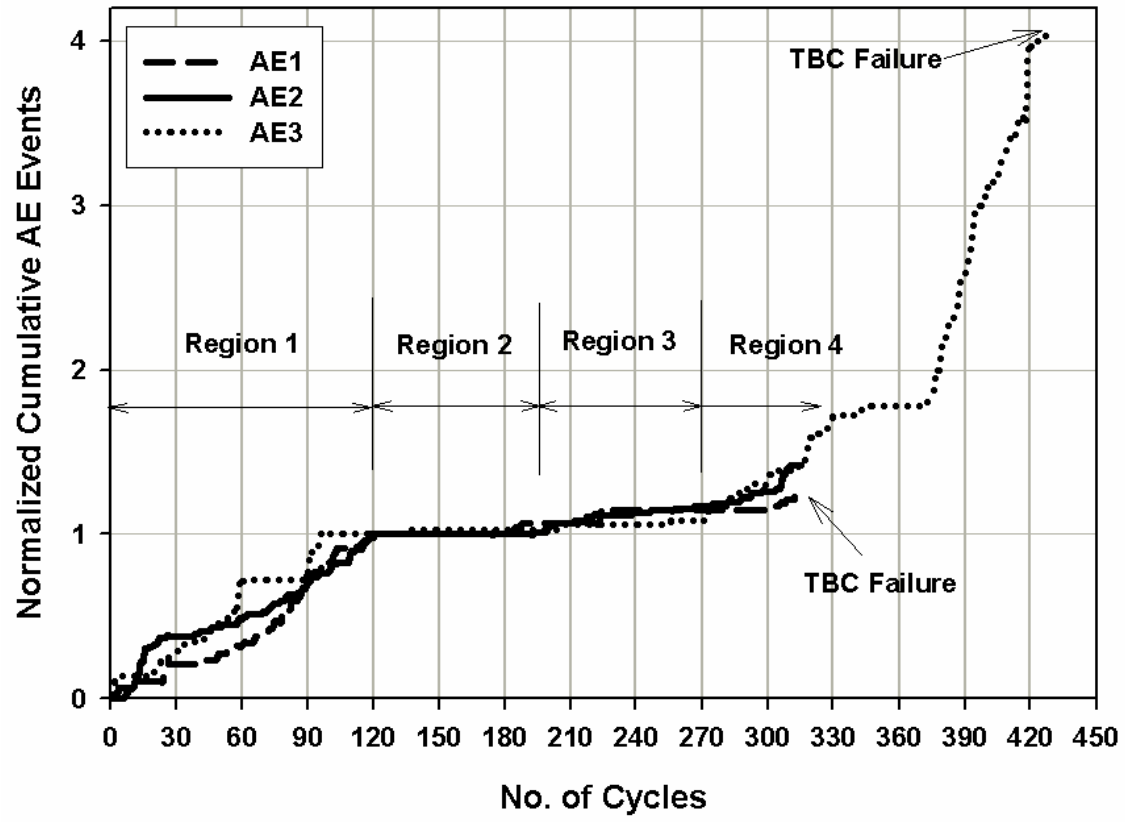

Figure 4.3: Normalized cumulative AE events during cooling and with amplitudes over 70 db.

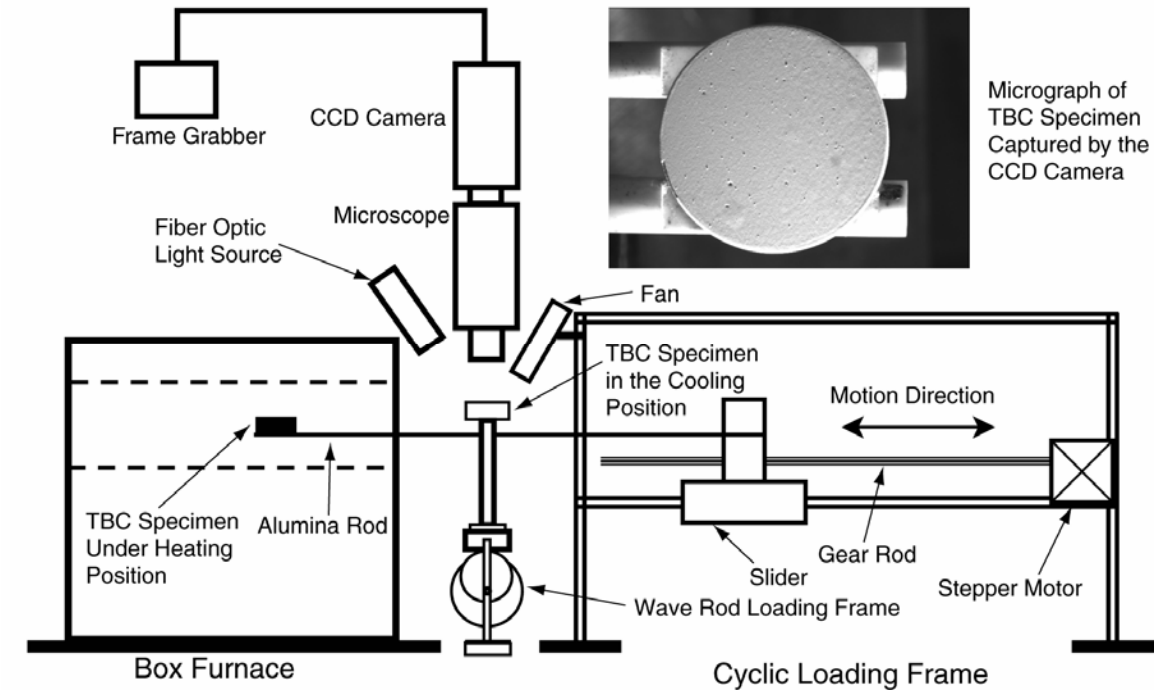

Figure 4.4: A schematic of the thermal cycling apparatus for *in situ* top coat surface image capture and AE detection with a waveguide rod.

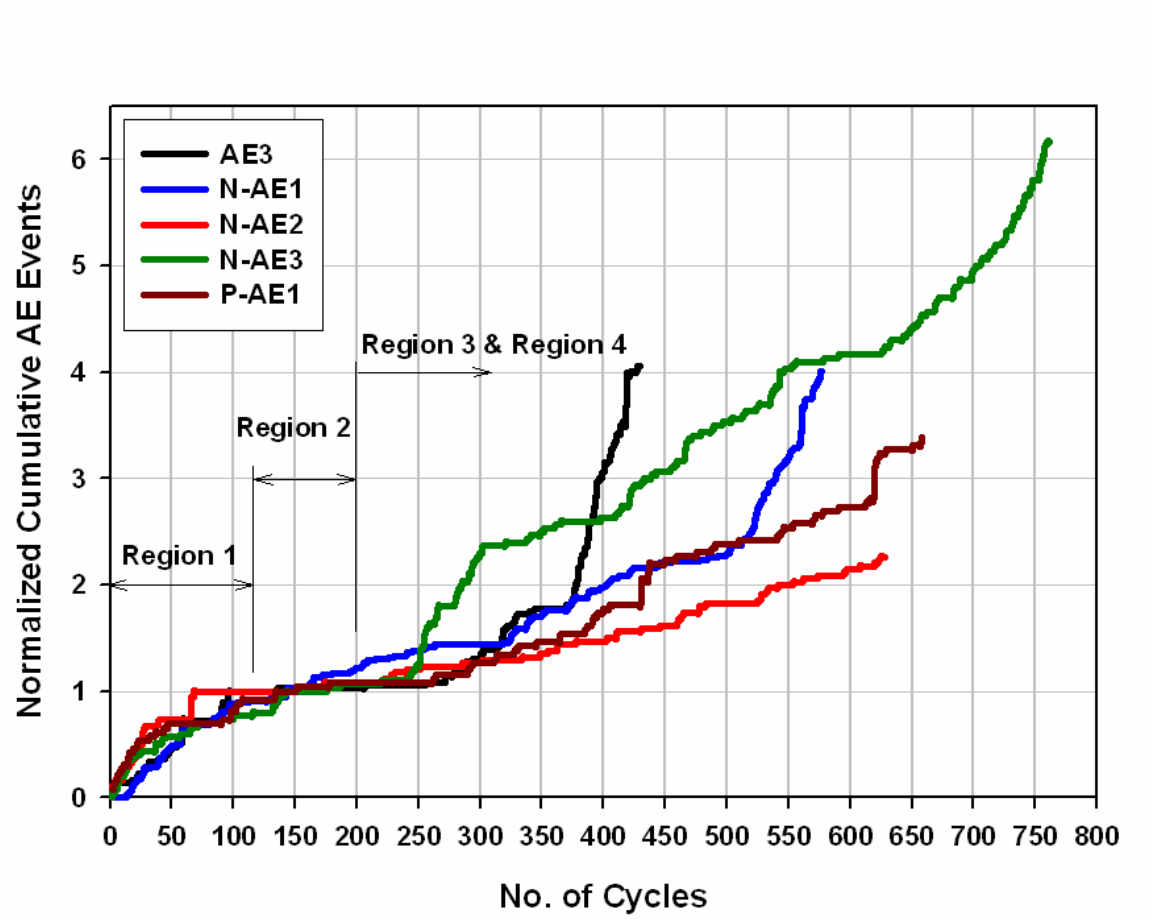

Figure 4.5: New experiments with normalized cumulative AE events during cooling from 1200 ºC.

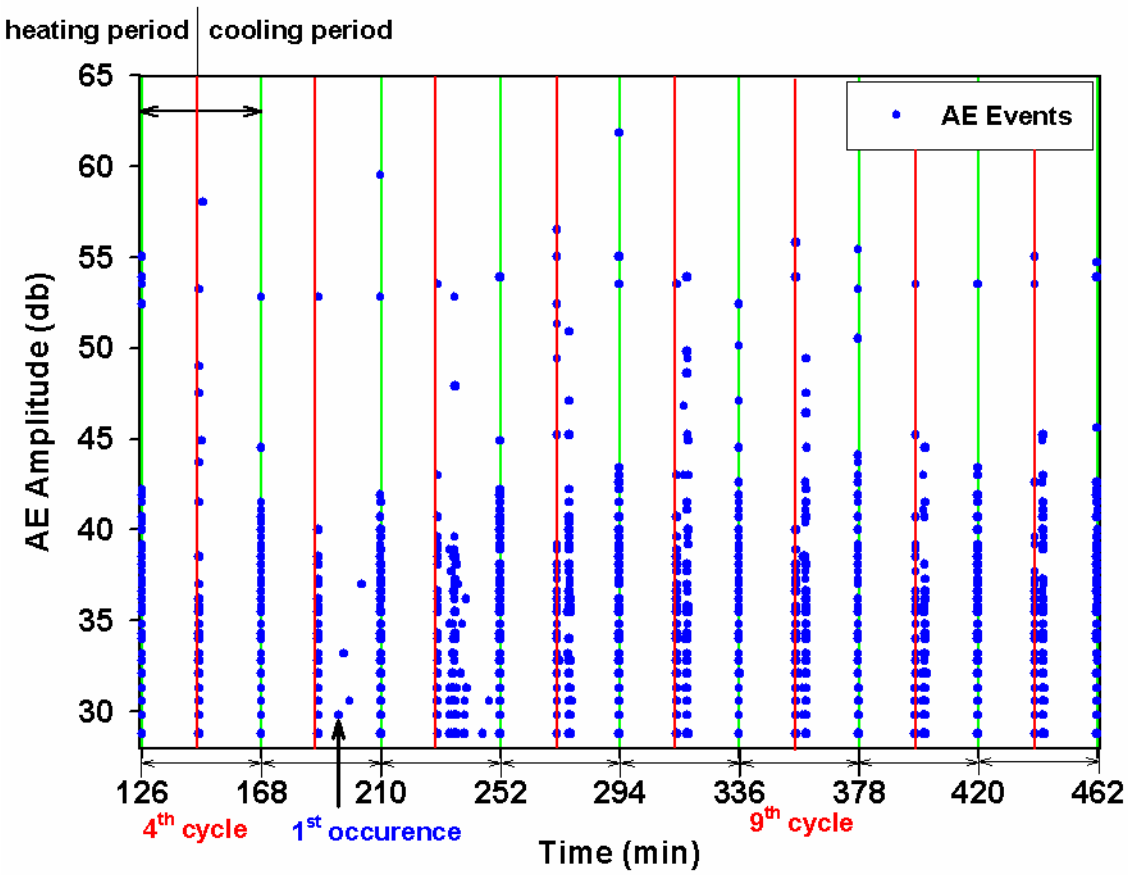

Figure 4.6: A plot of how the AE events are distributed throughout cycles 4 through 12. Note that after the 5th cycle there is activity between the initial cooling activity and the subsequent heating activity.

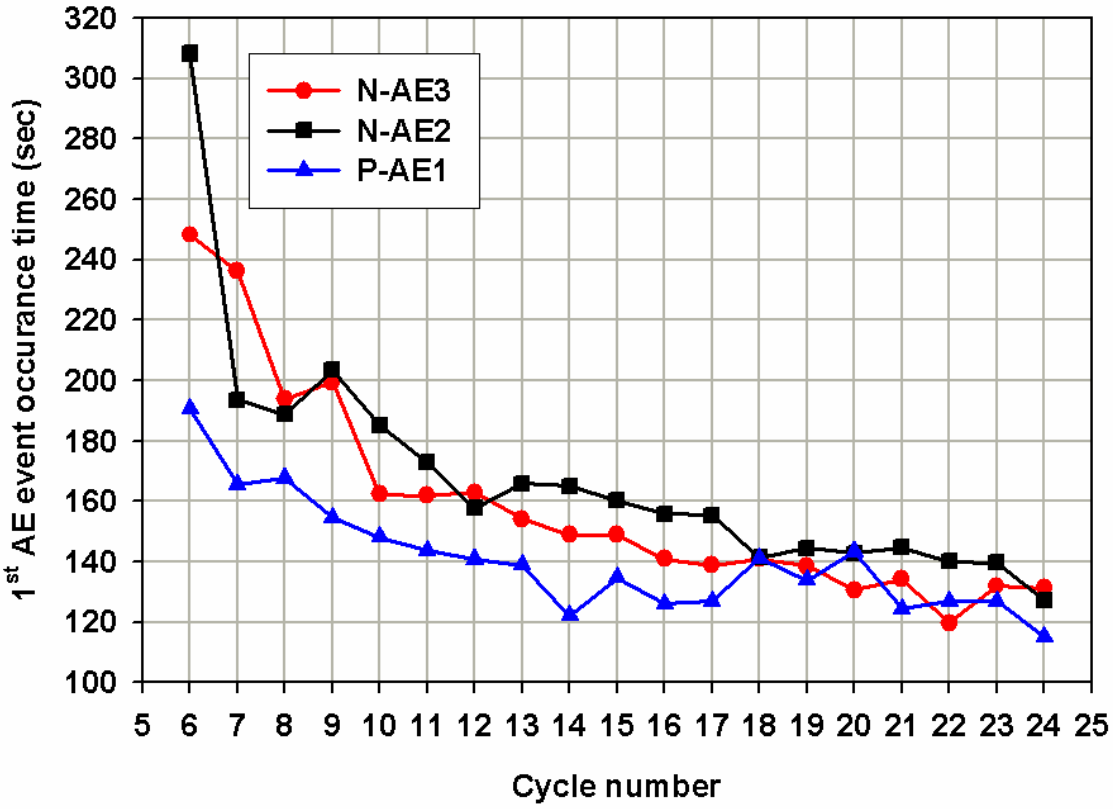

Figure 4.7: A plot showing the occurrence time of the first AE events after the initial cooling AE (See Fig. 4.6).

CHAPTER 5

ASSESSING THERMAL BARRIER COATING RESIDUAL STRESSES AND INTERFACE DELAMINATION WITH OPTICAL PROFILOMETRY

1. INTRODUCTION

Thermal barrier coating (TBC) spallation has been observed when TBC specimens are cooled from high temperature to ambient temperature. At ambient temperature, the thermally grown oxide (TGO) layer experiences high in-plane compressive stresses (3-6 GPa) mainly due to the coefficient of thermal expansion (CTE) misfit between the TGO layer and substrate and TGO swelling [18]. The TGO layer in-plane compressive stresses have been measured by piezospectroscopy [93, 96-98]. Curvature measurements can also be used to determine coating stresses. By measuring the curvature change of TBCs due to coating removal [30] and coating deposition [99, 100], the compressive stresses in the coating layer were evaluated. *In situ* TBC coating

stresses were also evaluated during the coating deposition process by measuring substrate curvature change and the temperature [101].

There is still considerable debate regarding the relaxation of TGO residual stresses. Some ways in which TGO stresses may relax include developing waviness of the TGO layer, interfacial cracking [4], plastic deformation of the bond coat and/or TGO [72], top coat creep [102-105], bond coat creep [26, 102, 106] and TGO creep [103-105]. Since TGO waviness develops in a parabolic fashion [4, 27-29], TGO waviness probably relieves TGO residual stresses during the earlier period of the TBC life. Interface crack formation would follow to relieve the TGO residual stresses after TGO waviness was formed.

Interface crack formation/coalescence result in roughness on the top coat after small scale buckling. Regions of intact interface and regions of top coat-TGO separation can generate undulations on the top coat surface [72]. Because of compressive residual stresses at the TGO layer, intact interface will form valleys and separated interface will form hills on the top coat surface. Therefore, the distribution of valleys and hills on the top coat surface can be directly related to interface debonding. By tracking the evolution

of the out-of-plane displacement of the top coat, interface crack coalescence can be studied.

The in-plane compressive stresses in the TGO layer generate large scale buckling of the top coat when the top coat becomes sufficiently debonded by interface cracks. Therefore, determination of the TGO layer's in-plane compressive stresses along with the debonding size is critical information for analysis of top coat buckling.

As mentioned in Chapter 4, a profilometer was used to measure TBC curvature change and top coat out-of-plane displacement after fixed numbers of thermal cycles. Curvature measurements are used to estimate the TGO layer residual stress evolution and changes to the top coat surface are used to investigate interface delamination. The undulation characteristics on the top coat surface are reported and are used to estimate the spacing between neighboring undulations. The undulation spacing provides valuable information for life prediction modeling.

2. TEST PROCEDURE

A TBC specimen was thermally cycled with the apparatus shown in Fig. 4.4. Prior to cycling, the TBC top coat was carefully polished by using 400, 600, 1000, and 2000 grit sand papers. As described in Chapter 4, acoustic emission (AE) was also

monitored during the experiment. The cycling and AE detection were interrupted regularly to measure curvature and other surface characteristics of the TBCs.

A Wyko NT3300 optical profilometer (www.veeco.com) was used to examine the top coat. The NT3300 uses a white light interferometer and is non-contact. The NT3300 has a vertical resolution to 0.1 nm and measures heights from Angstroms to millimeters. The accompanying software, Vision32 calculates surface measurement parameters including roughness by R parameters for 2-D measurement and S parameters for 3-D measurement. The software also has a useful option called "stitching" to generate the high resolution full field surface profiles and can also produce full field 3-D profile images.

3. RESULTS

3.1 TBC CURVATURE CHANGE

When a thin coating is bonded to a substrate and is under residual stresses, the substrate forms curvature to compensate for the coating stresses [71]. The curvature can be related to the stress state, and therefore measurement of coating-substrate curvature

enables quantification of residual stresses. The curvature can be expressed by the Stoney formula [71]

$$k = \frac{1}{R} = \frac{6f}{M_s h_s^2}, \qquad \text{(Eq. 5.1)}$$

where κ is the curvature and R is the radius of curvature. M_s and h_s are the biaxial modulus of the substrate material and the thickness of the substrate, respectively. M_s can be expressed as $E_s/(1-\upsilon_s)$ where E_s and ν_s are elastic modulus and Poisson's ratio of the substrate material, respectively. f is the force per unit length on the coating. The main advantage of using Stoney's formula lies in the absence of coating material properties. Since the coating is much thinner than the substrate, coating material properties can be neglected.

Since TBCs are basically four layer systems consisting of a top coat, TGO, bond coat, and substrate layer, Eq. 5.1can not be used directly to calculate the TGO layer residual stresses from the TBC curvature change. However, since the TGO layer generates stresses that are much bigger than the top coat layer stresses, it will be assumed that the curvature change is caused solely by the TGO layer stresses. Since the top coat is very thin and the modulus of the top coat is very low before zirconia sintering, the

assumption of sole effect of TGO layer stresses on the curvature change is reasonable. Even with zirconia sintering, the top coat is probably not completely sintered out dense. Also, because the modulus and CTE of the bond coat is similar to that of the substrate and the bond coat thickness is negligible compared to the substrate thickness, the bond coat can be regarded as the part of the substrate.

Figures 5.1a and 5.1b show contour maps of the top surface profile for a specimen cycled 32 and 634 times, respectively. Details regarding the cycling were provided in Chapter 4. The specimen was marked so that it could be returned to the profilometer in the same orientation after each round of cycling. After 32 cycles the specimen already shows distinct convex curvature. However, Fig. 5.1a does not show noticeable roughness on the top surface. After 634 cycles the specimen shows a slight increase in convex curvature. More significantly, compared to the specimen cycled 32 times, for the specimen cycled 634 times the top coat roughness has increased from R_z = 0.431 μm to R_z = 2.250 μm. R_z is the average maximum profile height and is the average of the vertical height distance between the ten highest points and ten lowest points in the evaluation area. After 634 cycles damage along the edge of the specimen is also visible in the profilometry image.

Figure 5.2 shows top surface profiles for a TBC specimen at different numbers of cycles. The profiles were taken along the diameter of the TBC specimens in the y-direction. The curvature and roughness evolution is clearly shown in Fig. 5.2. Also, the as-coated specimen only has a few dimples which are probably from initial defects in the top coat. It is clearly shown that after just 32 thermal cycles, the curvature and roughness increases significantly compared to the as-coated specimen. The curvature and roughness is relatively constant between the 32nd to 200th thermal cycles. Curvature and roughness begin to change again between the 200^{th} and 300^{th} cycle and the rate of increase of curvature and roughness accelerated significantly after 300 thermal cycles.

The curvature (κ) of the TBC was determined from the radius of the convex curve (radius of curvature, R) along the diameter of the TBC specimen. The value of R was given by the Vision32 software. Then κ was calculated by taking the reciprocal of R. Figure 5.3 quantitatively shows the curvature of the TBC along with AE events from P-AE1. It is noted that the curvature change and AE events are closely related. Generally speaking, AE events happen whenever the curvature is increasing.

To model TGO formation, a parabolic growth model [107] is used, and therefore the TGO thickness, h_{TGO} can be expressed as follows:

$$h_{TGO} = \sqrt{k_p t} \quad \text{where} \quad k_p = D_0 \exp(-Q/RT), \qquad \text{(Eq. 5.2)}$$

where t is time, k_p is the parabolic growth constant, and T is temperature. Q is the activation energy for O_2 and has a value of 320 kJ/mol. R=8.314 J/mol/°K is the universal gas constant. D_0 is the diffusion constant and was found by fitting experimental data to the parabolic growth model for 1200 °C cyclic heating. The TGO thickness data were extracted from the cross section views of the cycled specimens in Chapter 3. The specimens were PtAl bond coats (LDC-2E) completely covering CMSX-4 superalloy buttons. The heating period was 10 minutes. Although, there were differences in the specimen type and cycling conditions, the data is applicable for the current system and experimental condition because of the following reasons: the cyclic heating temperature which is most critical to TGO parabolic growth was identical and bond coat material was same type of PtAl. For cyclic heating, D_0 was found to be $9.9\times10^{-5}m^2/s$. For reference purpose, D_0 was found to be $4.9\times10^{-5}m^2/s$ for quasi-isothermal heating. The TGO formation curve shown in Fig. 5.4 was generated by using Eq. 5.2 with the experimentally determined value for D_0 . Each red dot in Fig. 5.4 represents the TGO thickness data from the cycled specimens in Chapter 3.

The mean stress σ_m of the TGO layer can be expressed as

$$\sigma_m = \frac{f}{h_{TGO}}. \qquad \text{(Eq. 5.3)}$$

Therefore, for constant *f*, the mean stress in the TGO layer decreases as the thickness of the TGO layer increases.

Figure 5.5 shows the normalized residual stresses in the TGO and AE events as a function of number of cycles. The residual stresses were calculated with Eqs. 5.1-5.3. The material properties used in these equations are E_s = 213 GPa and v_s = 0.25 for the René N5 substrate [108]. The stress was normalized by dividing the residual stress calculation for each cycle by the residual stress calculation for the specimen cycled 32 times. The TGO layer residual stresses increase rapidly and reach a maximum value at the earlier cycles of TBC life and then decrease with further thermal cycling. Although curvature is continuing to increase, the growth of the TGO causes the mean TGO stress to decrease. A pivotal moment occurs near the 300th cycle when the TGO layer residual stress slowly increases again until the failure. The variation of TGO layer residual stresses with increasing numbers of cycles is similar to what was previously measured with photoluminescence [22]. The observation from Fig. 5.3 that AE events are occurring when curvature changes can also be applied to Fig. 5.5 which shows that AE

events occur when residual TGO stresses increase. This linkage is not surprising since curvature and residual stress are related through Eqs 5.1–5.3.

As seen in Fig. 5.3 and Fig. 5.5, the TBC curvature and TGO layer residual stresses increase drastically during the first 32 cycles. This is accompanied by high accumulation of AE events. The TGO layer residual stresses seem to reach a maximum value between the starting of cycling and the 32nd cycle. During the rapid increase in TGO residual stresses, there is also a sharp increase in the thickness of the TGO (see Fig. 5.4). This curvature (residual stress) increase resulted from the substrate bending to compensate for the in-plane compressive force on the TGO layer whose coefficient of thermal expansion is lowest of all TBC components. In addition, it is known that there are intrinsic compressive stresses developed during TGO growth [30, 104]. Since the TGO is under significant compression, this leaves the substrate and top coat in tension. The suggestion in Chapter 4 that AE events in Region 1 of the TBC life are from vertical cracking in the top coat is supported by curvature and residual stress measurements in this chapter.

After the 64th cycle, the AE events diminished and the curvature stayed the same. Since the TGO is thickening, constant curvature implies that the mean TGO layer

residual stresses is decreasing. The curvature stayed almost unchanged and TGO layer residual stresses decreased between the 100^{th} and 200^{th} cycle. There are several reasons why the curvature remains constant and TGO layer residual stresses decrease.

First of all, the TGO layer waviness is increasing [20, 33]. The TGO layer waviness relieves compressive stresses in the TGO layer. The creep of the bond coat can also contribute to the residual stress relief [26, 102, 106]. Therefore, constant curvature may result from competition between the TGO growth and TGO waviness/bond coat creep. It is noteworthy that the region of constant curvature and decrease in TGO layer residual stresses is coincident with the AE event plateau period.

A second potential reason for constant curvature is related to sintering of the top coat. After relatively short thermal exposure (50 cycles of 1hour heating at 1200 °C), feathery features of the individual yttria stabilized zirconia (YSZ) columns sinter together and create necks between columns [41]. As the top coat sinters, the top coat becomes stiffer and tensile force at the top coat/TGO interface during the cooling cycles gradually increases. This tensile force at the top coat/TGO interface helps the substrate counteract the compressive TGO forces and therefore the system remains straighter.

Between the 200th and 300th cycle, both curvature and AE activity start to rise again. As thermal cycling continues, the TGO layer thickens and the compressive force at the TGO layer increases. The TGO waviness formation seems to slow down at this point in the TBC life. It also seems that from this point, crack nucleation initiates at valleys in the TGO waviness. It has been reported that crack nucleation initiates after 34% of cyclic life [6]. In the current research the curvature and AE event increase between the 200th and 300th cycle coincides with around one third of the TBC life. The curvature and the AE activity increase noticeably after around the 300th cycle and continue to increase until TBC failure. However, the degree of the increase is minimal compared to the increasing during the 1st 100 thermal cycles. It seems that the combination of the compressive stresses and waviness at the TGO layer reaches its critical point at around the 300th cycle and interface cracking/delamination becomes active after this point. After approximately 300 thermal cycles, due to the combination of interface cracking/delamination and compressive residual stresses, the top coat may undergo small-scale buckling.

3.2 ROUGHNESS/WAVINESS CHANGE DURING THE TBC LIFE

Figures 5.6a and 5.6b show three-dimensional images of the top surface profile for the specimens cycled 32 and 634 times, respectively. The corresponding contour maps for these specimens were shown in Figures 5.1a and 5.1b. Fig. 5.6a shows roughness which was not clearly shown in Fig. 5.1a. Comparison between Figures 5.6a and 5.6b displays the obvious roughness evolution of the top coat surface.

Figure 5.7 shows a zoomed-in view of Fig. 5.2 for the purpose of better demonstrating the roughness profile changes of the top coat. Roughness changes drastically during the first 32 thermal cycles. Between the 32^{nd} and 300^{th} cycle, the roughness profile does not change significantly. However, after around 300 thermal cycles, the surface exhibits much more significant roughness which continue to evolve until TBC failure.

Figure 5.8 quantitatively shows the roughness change by plotting top coat average maximum profile height, R_z change and AE event change during the TBC life. The average R_z values in Fig. 5.8 also have bars indicating the standard deviation. The as-coated specimen's R_z value results from pre-existing defects on the top coat surface. The average maximum profile height initially varies parabolically with number of cycles.

However, there is a slope change in the average maximum profile trend near the 200th cycle. From the as-coated to the 200th cycle, the more rapid rise in R_z may be related to the TGO layer waviness formation. The top coat average maximum profile changes less rapidly from the 300th cycle to failure compared to the 1st 100 thermal cycles. It seems that this 300th cycle to failure region's average maximum profile increase is related to interface delamination of the top coat.

In Fig 5.9 the roughness profile change of the top coat is presented statistically with histograms that show the number of data points at each surface height on the entire top coat surface. The surface height of "0" is defined by the height of the mean line of the top coat surface. The number of data points at larger surface heights has increased noticeably by 32 thermal cycles, stays relatively constant between the 32nd and 200th cycle, and increases again after the 300th cycle. The general histogram shape from the 64th to the 200th cycle is similar. Although the general histogram shape from the 300th to 634th cycle is similar, the number of data points at a surface height greater than 6 μm significantly increases as thermal cycling progresses. Increased roughness in the latter portion of the TBC life is believed to be related to small-scale buckling which is in turn related to interface delamination. If areas with a surface height greater than 6 μm are

designated as delaminated, small - scale buckled area, then these regions will most likely be the ones where spallation initiates. Therefore, 6 μm will be the critical surface height that indicates the presence of small-scale buckling.

There are additional ways to characterize surface profiles. The mean spacing and peak count describe the wavelength and frequency change of the top coat due to waviness formation. The mean spacing is the horizontal distance between points that cross the mean line of the top coat surface and the peak count is the number of the peaks which locate above the roughness average. Figure 5.10 shows the mean spacing and peak count change during TBC life. The mean spacing change follows a trend that is similar to that of the average maximum profile. The mean spacing changes rapidly after the first 32 cycles, changes slowly up to the 133rd cycle, and stays constant up to the 200th cycle. The means spacing up to the 200th cycle therefore seems to be influenced primarily by the development of TGO waviness. The peak count changes in the opposite direction of the mean spacing value. The peak count diminishing indicates coalescence of adjacent interface delaminations. The rate of change of mean spacing and peak count change again between the 200th and 300th cycle.

It is also interesting to observe that roughness changes differently in different annuli of the round specimen. The specimen is initially roughening in the center of the specimen up to approximately two thirds of the specimen's radius. The largest peak to valley distances occur at the outer edges of this central region. The waviness extends beyond two thirds of the specimen radius and starts to cover the entire top coat surface after the 100^{th} cycle. After the 200^{th} cycle, the average wavelength (mean spacing) of the bumps approaches 0.6 mm, and there are around 0.82 peaks/mm along the 25.4 mm diameter of the specimen. After the 300^{th} cycle the mean spacing continues to increase with further cycling. Due to what is believed to be small-scale local buckling, bumps appear on the top coat. From these experimental results, it is estimated that a mean spacing of around 0.7 mm will lead to buckling of the YSZ. Between the bumps, there are valleys which are due to intact interfaces. The average length of these valleys is 0.2 mm.

Between the 600^{th} and 634^{th} cycles the roughness increases rapidly. At this point there are only 20 or so cycles remaining in the TBC life, and this roughness increase may indicate more critical top coat delamination/small scale buckling. A few larger wavelength bumps appear toward the edge of the top coat surface after the 600^{th}

cycle. These bigger wavelength bumps seem to be created after coalescence of adjacent interface delaminations and several smaller bumps assembling into one bigger bump. The wavelength of the bigger bumps averages to 1.7 mm and 2.8 mm for the 600^{th} and 634^{th} cycle, respectively.

Figures 5.11a and 5.11b show 2-D and 3-D images of post small-scale buckling locations after 634 thermal cycles. Figures 5.11a and 5.11b are also the magnified views of the rectangular regions highlighted in Figures 5.1b and 5.6b. Figures 5.11a and 5.11b show a distinctive bump surrounded by smaller bumps which will soon coalescence and cause spallation of the TBC. Coalescence of interface delaminations happens near the end of the TBC life (~90% of the TBC life), and these few bigger bumps are responsible for spallation of the TBC. The absence of coalescence until the end of the TBC life was proven by the thermal imaging of TBCs, and the critical size of the delamination for spallation was also mentioned [109].

As shown in Figures 5.11a and 5.11b, the spallation causing delamination is elliptical in shape. The elliptical defect is orientated with the longer axis of the ellipse aligned with the radial direction of the specimen. This orientation indicates that interfacial cracks propagated toward the center of the specimen along the radial direction

[110]. The spallation causing delamination is 2.8 mm long and 1 mm wide after 634 cycles. Imaging leads to the conclusions that coalescence happens from four adjacent bumps being connected in the radial direction.

Figure 5.12 shows x and y profiles of the spallation causing delaminated spots shown in Figures 5.11a and 5.11b. Fig. 5.12 shows the spallation causing delaminated spots have 3 ~ 4 μm higher peak points than the rest of the bump peaks. The absolute height of the spallation causing delaminated spots is placed above the critical surface height of 6 μm which was mentioned earlier and is associated with Fig. 5.9.

Figure 5.13 shows a top surface CCD camera image just one cycle before spallation. The 4.5 mm long and 2.7 mm wide bump in Fig. 5.13 was from coalescence of adjacent bumps including the distinctive bump and surrounding bumps in Figures 5.11a and 5.11. As mentioned earlier, the bump is more elliptical than circular. This is further proof of the orientation of coalescence. More detailed study of the spallation causing delaminated spots will be presented in Chapter 6.

4. CONCLUSION

Interrupted-test optical profilometry has shown that sudden curvature and roughness increases happened after just 32 thermal cycles. During the 32 to 200 thermal

cycle range, minimal curvature and roughness changes occurred. Curvature and roughness began increasing again after around 300 thermal cycles.

TGO layer residual stresses were calculated using measured curvature and Stoney's formula. The TGO layer residual stresses increased rapidly during the first 32 thermal cycles. Due to TGO waviness and bond coat/TGO layer creep, the TGO layer residual stresses decreased after the first 32 thermal cycles.

Roughness change of the top coat was related to TGO waviness and interface crack delamination/coalescence and small-scale buckling. Coalescence of interface delamination was observed near end of the TBC life. Curvature and roughness change followed trends that were almost identical to the trends in AE activity. This supports the notion that AE events are closely related to TGO layer residual stresses and interface damage.

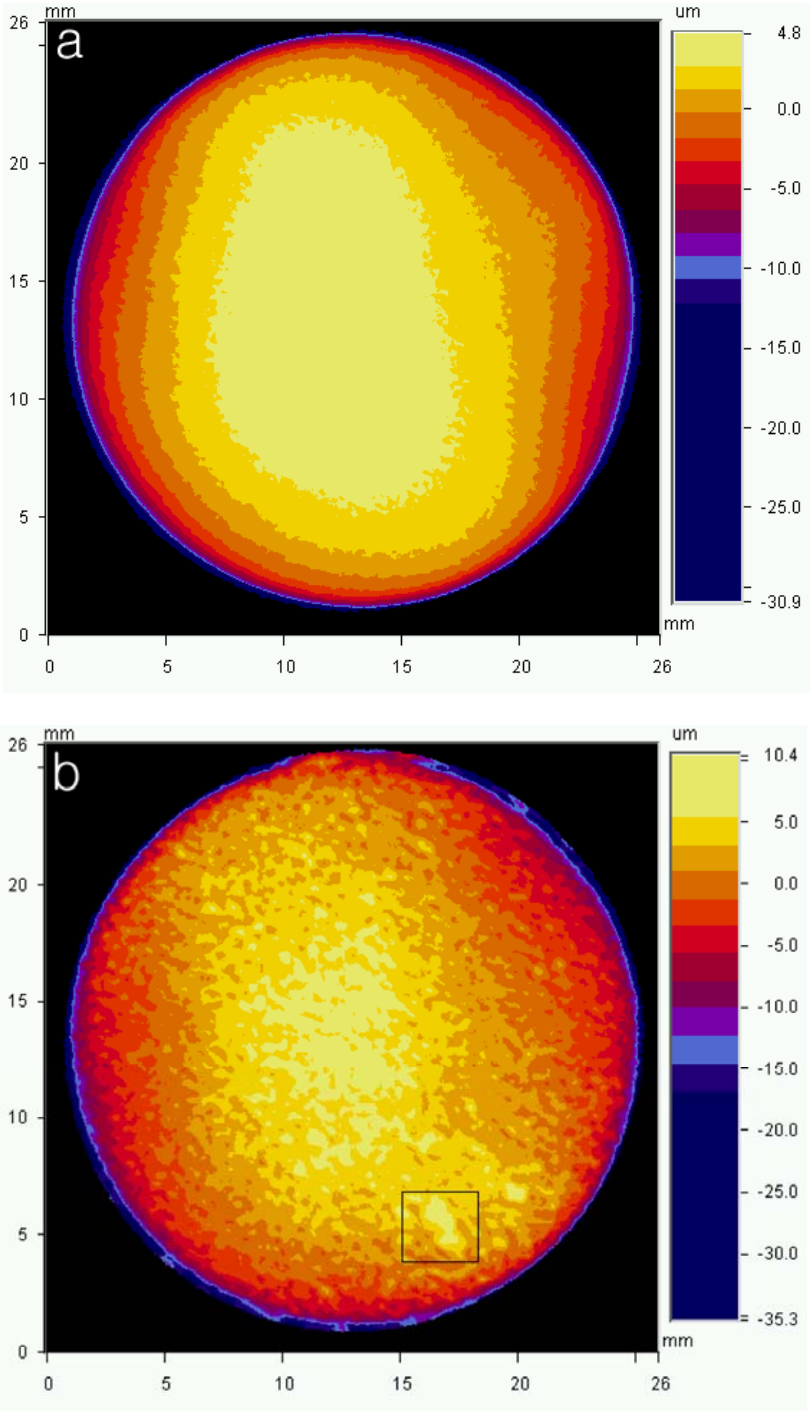

Figure 5.1: Top surface profile images for a specimen cycled (a) 32 times and (b) 634 times.

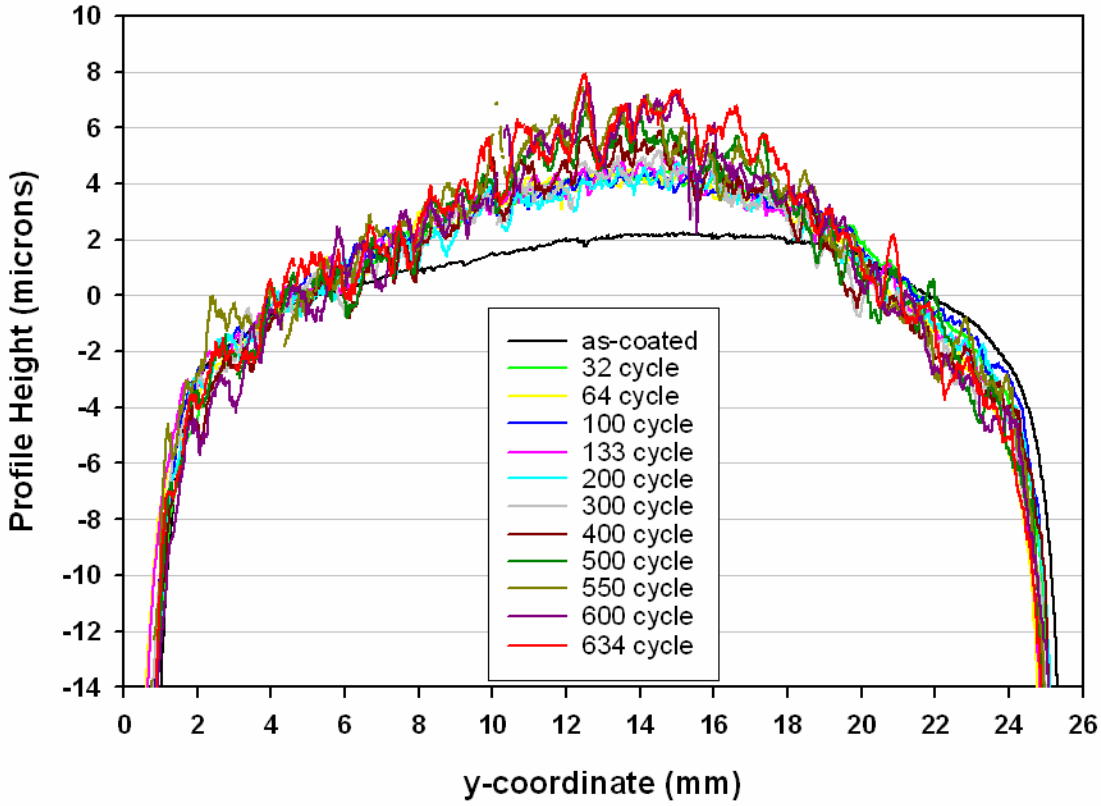

Figure 5.2: Profiles of the top surface along the diameter of the TBC specimens and in the y-direction.

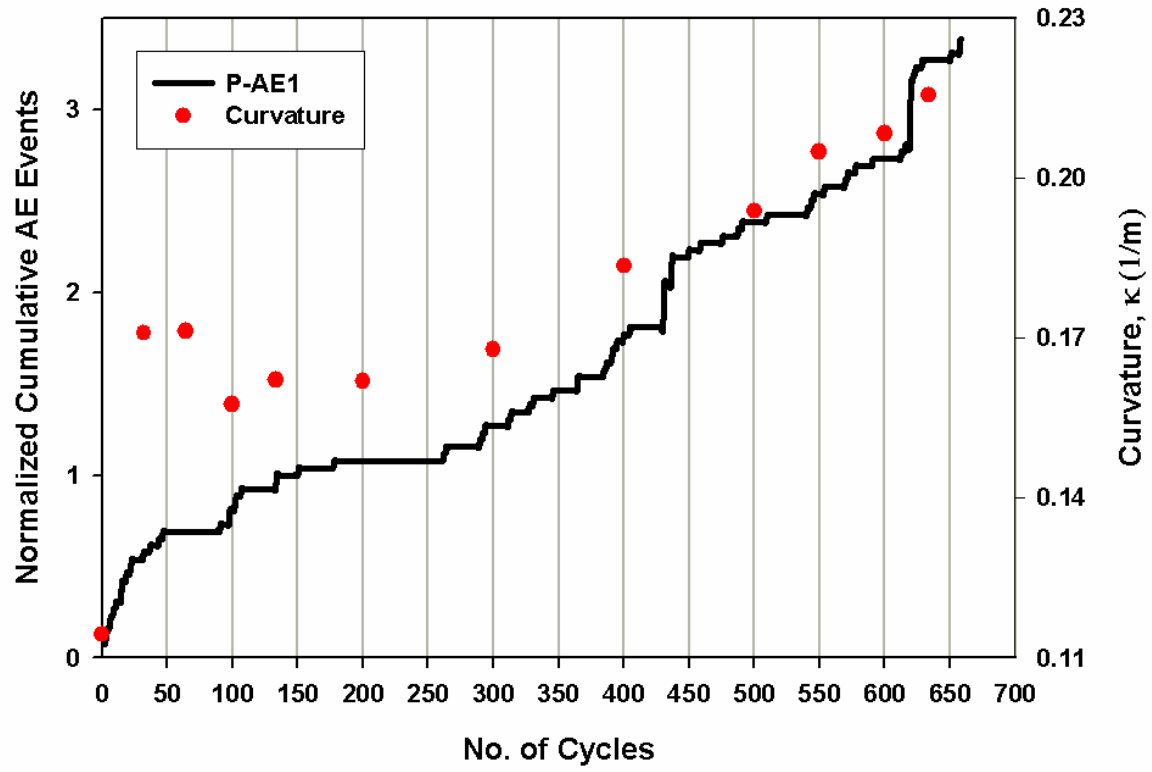

Figure 5.3: The top coat curvature and cumulative AE events both plotted as a function of number of cycles.

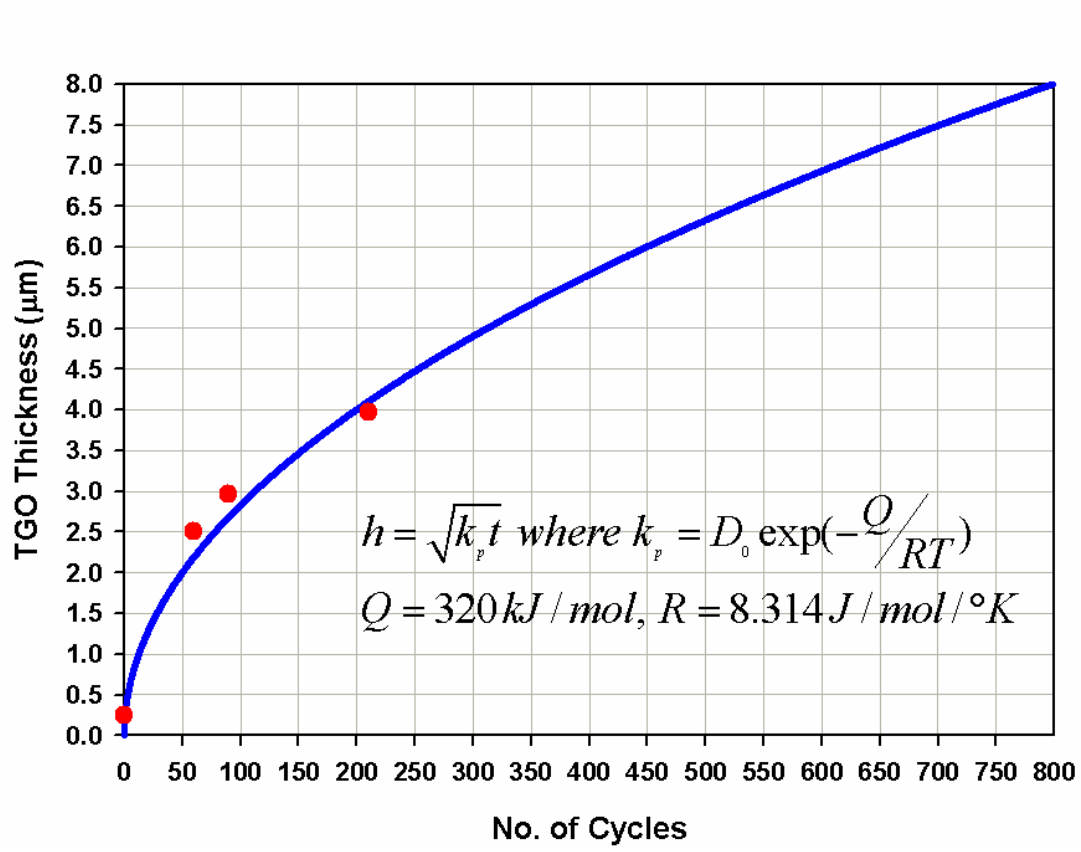

Figure 5.4: The parabolic TGO growth model for 1200 °C heating cycles.

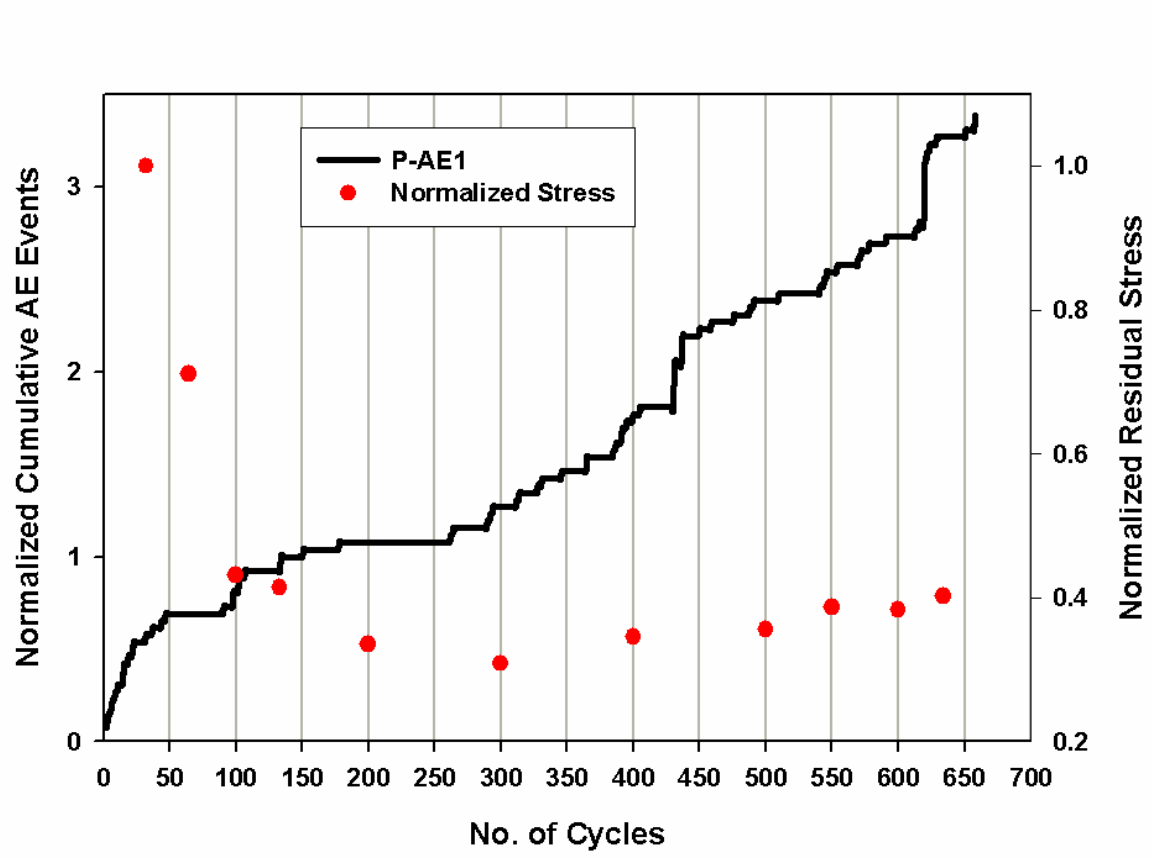

Figure 5.5: The normalized TGO layer residual stresses along with AE events.

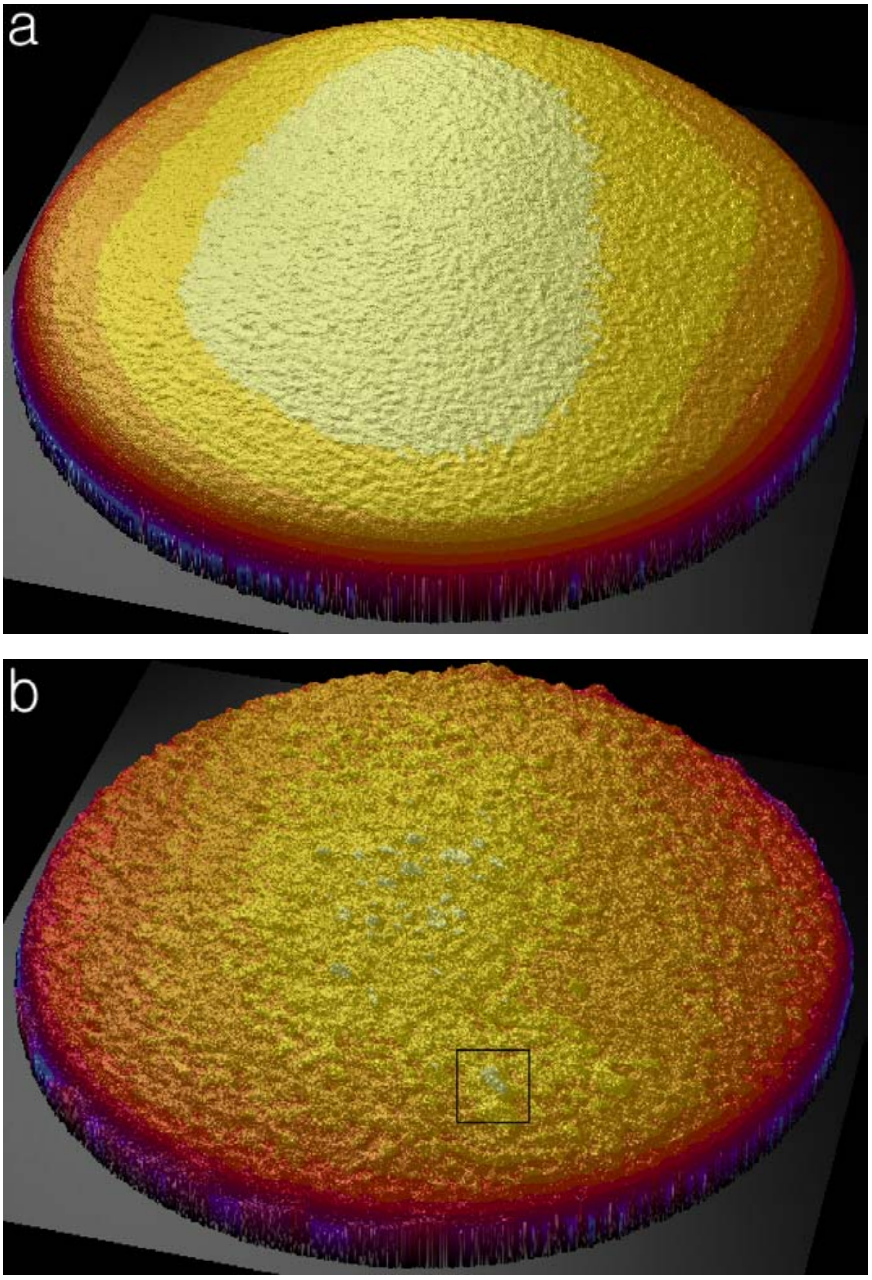

Figure 5.6: 3-D images of the top surface for the specimen cycled (a) 32 times and (b) 634 times.

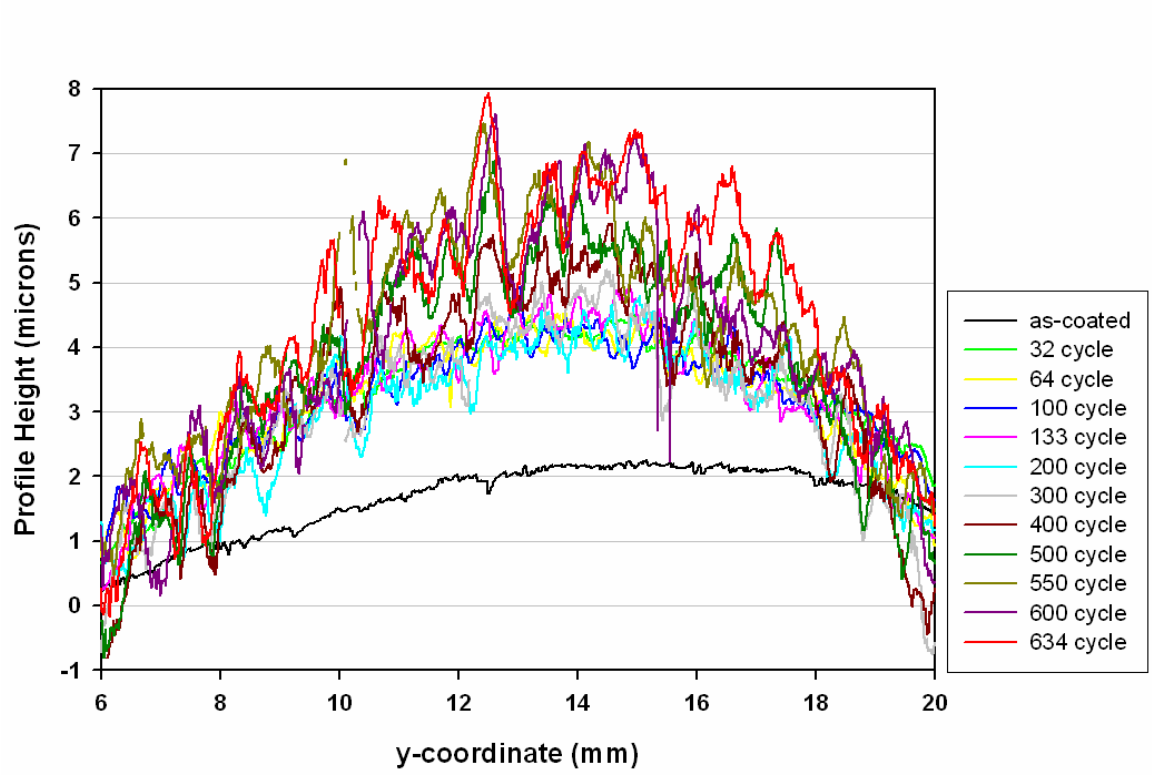

Figure 5.7: Re-plotting of the profiles shown in Fig. 5.2 with a smaller scale which highlights the roughness of the specimens.

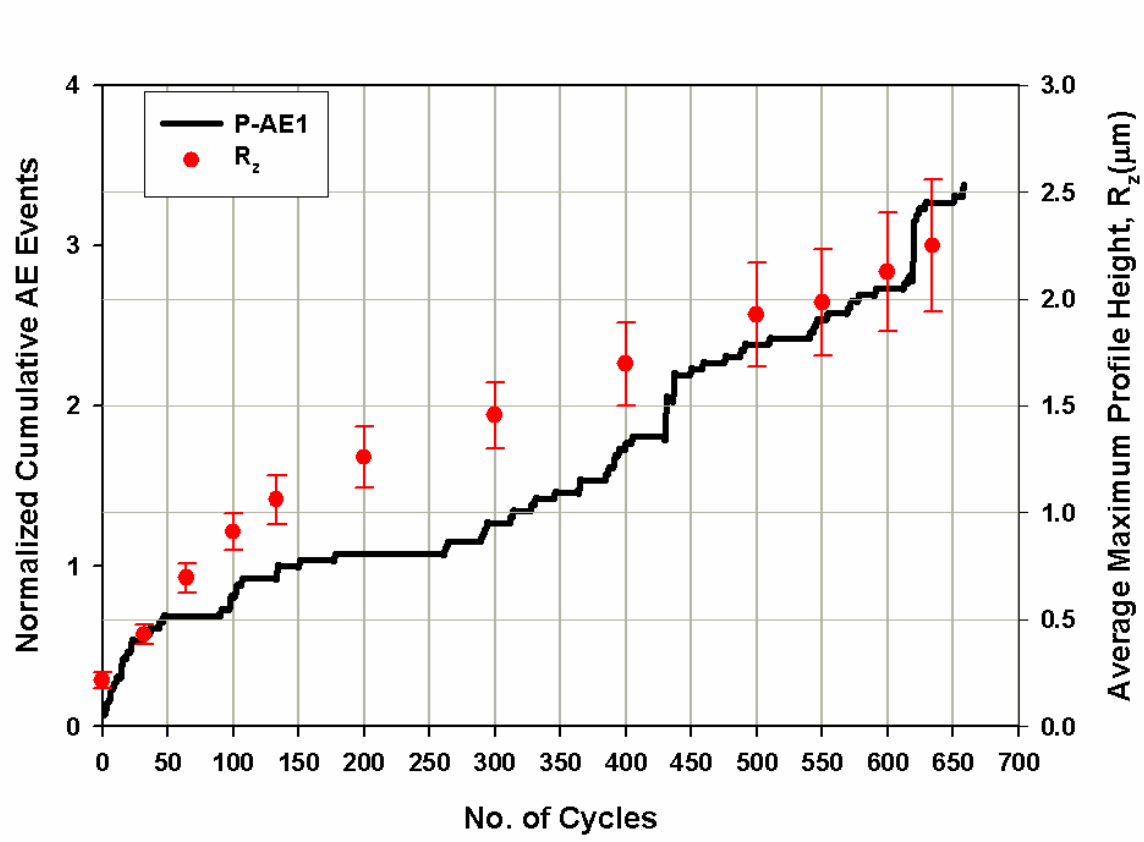

Figure 5.8: The average maximum profile (R_z) changes (with standard deviation) and AE events during 1200 °C heating cycles.

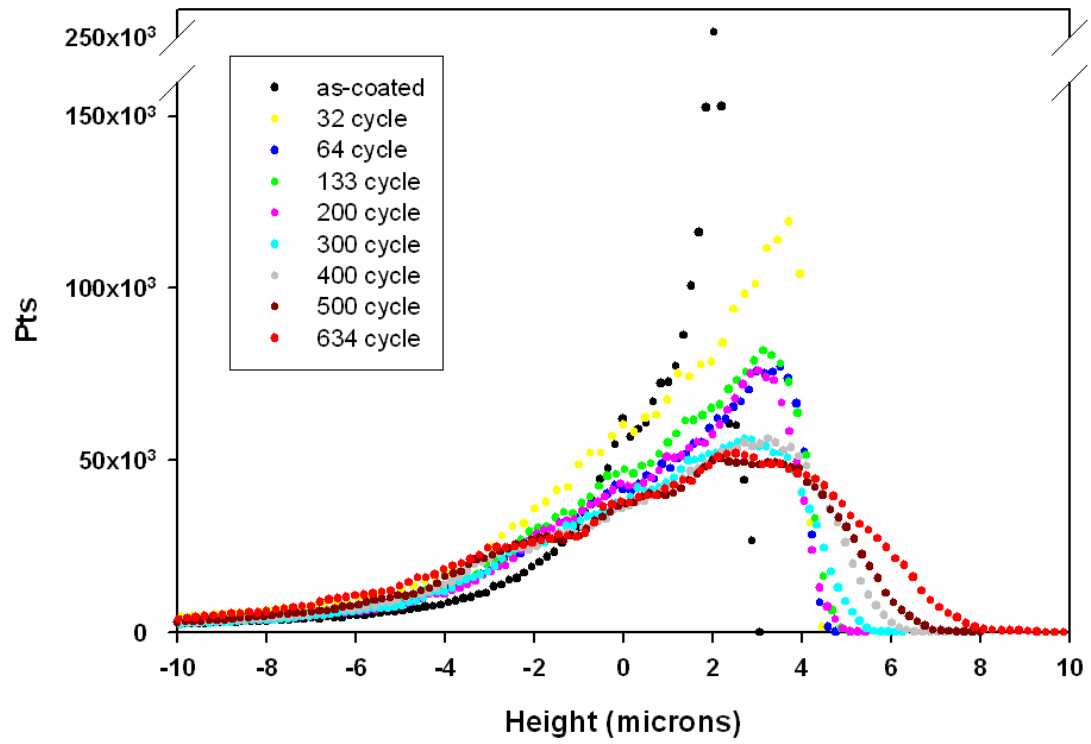

Figure 5.9: Histograms showing the number of times each height appears in a specimen cycled different numbers of times.

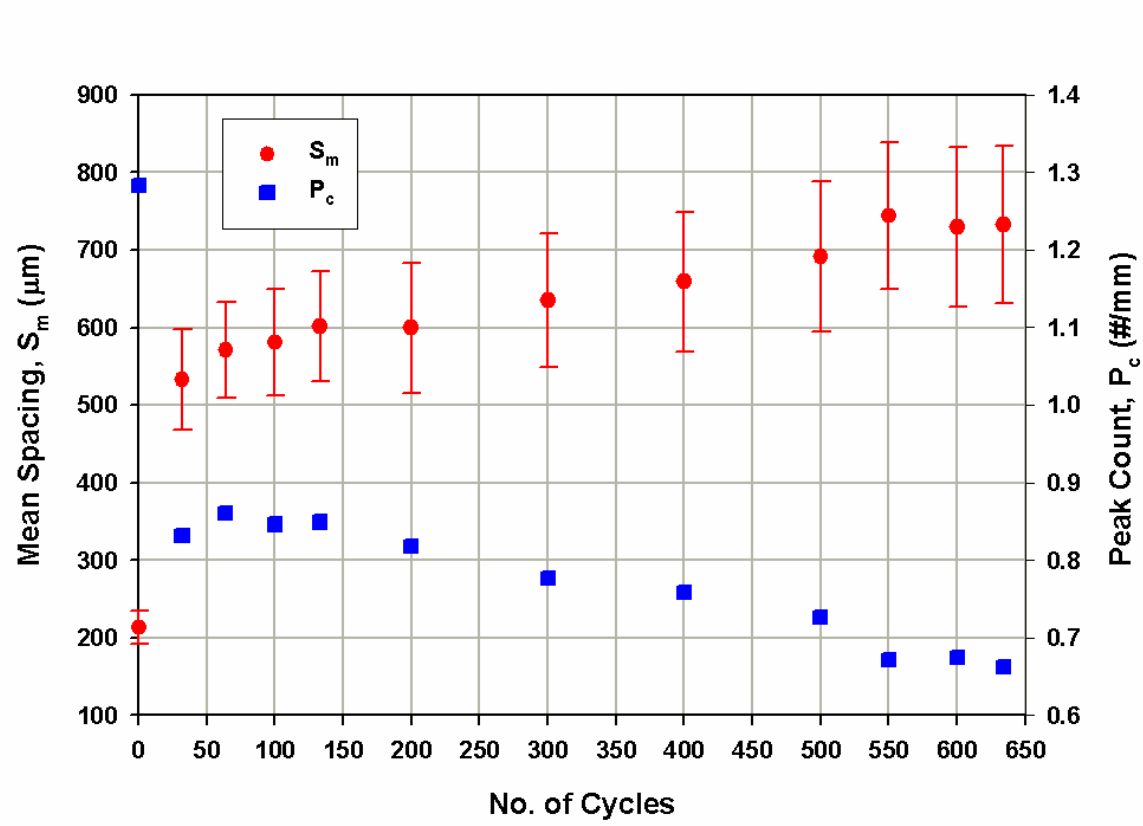

Figure 5.10: Mean spacing and peak count values during the TBC life.

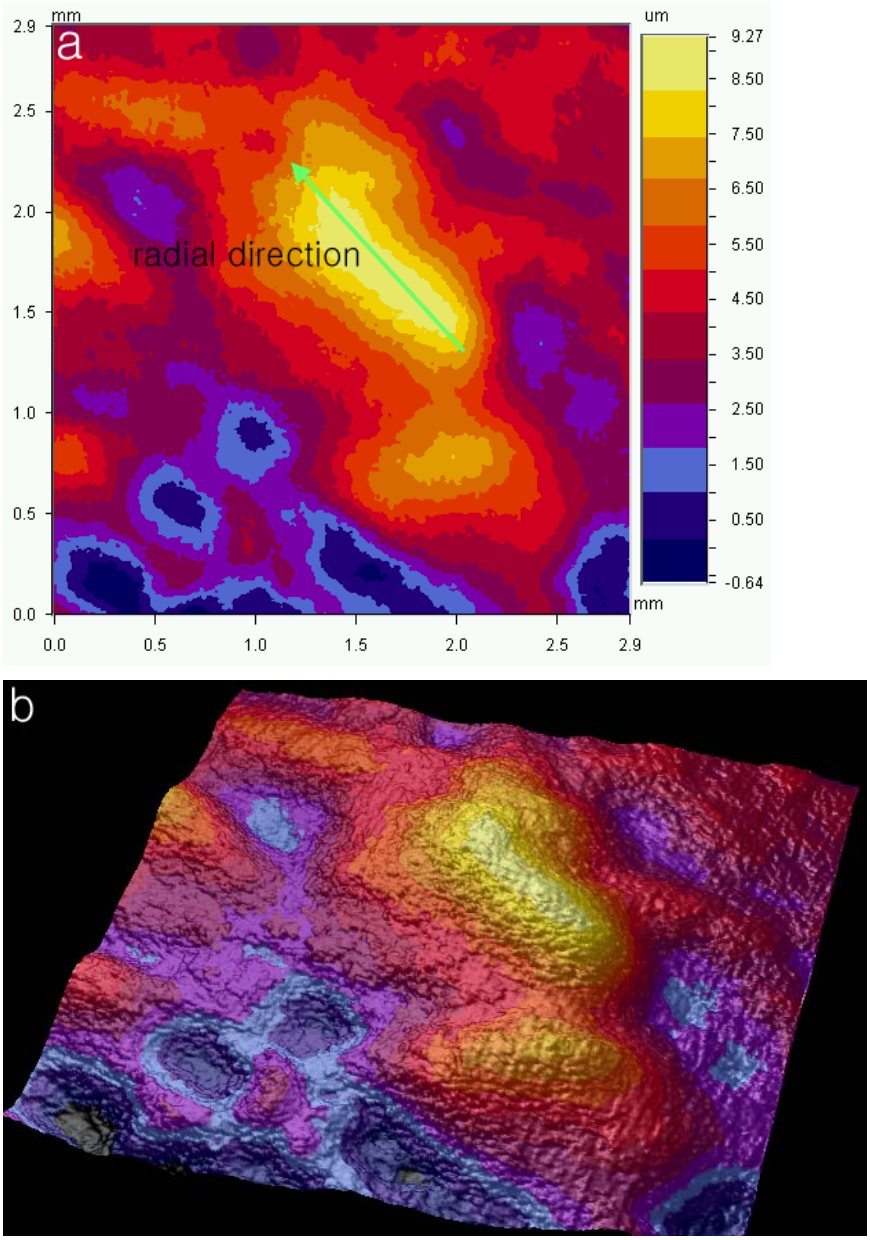

Figure 5.11: Detailed images of (a) a 2-D contour plot and (b) a 3-D plot of a delamination in the specimen cycles 634 times; this delamination caused final spallation.

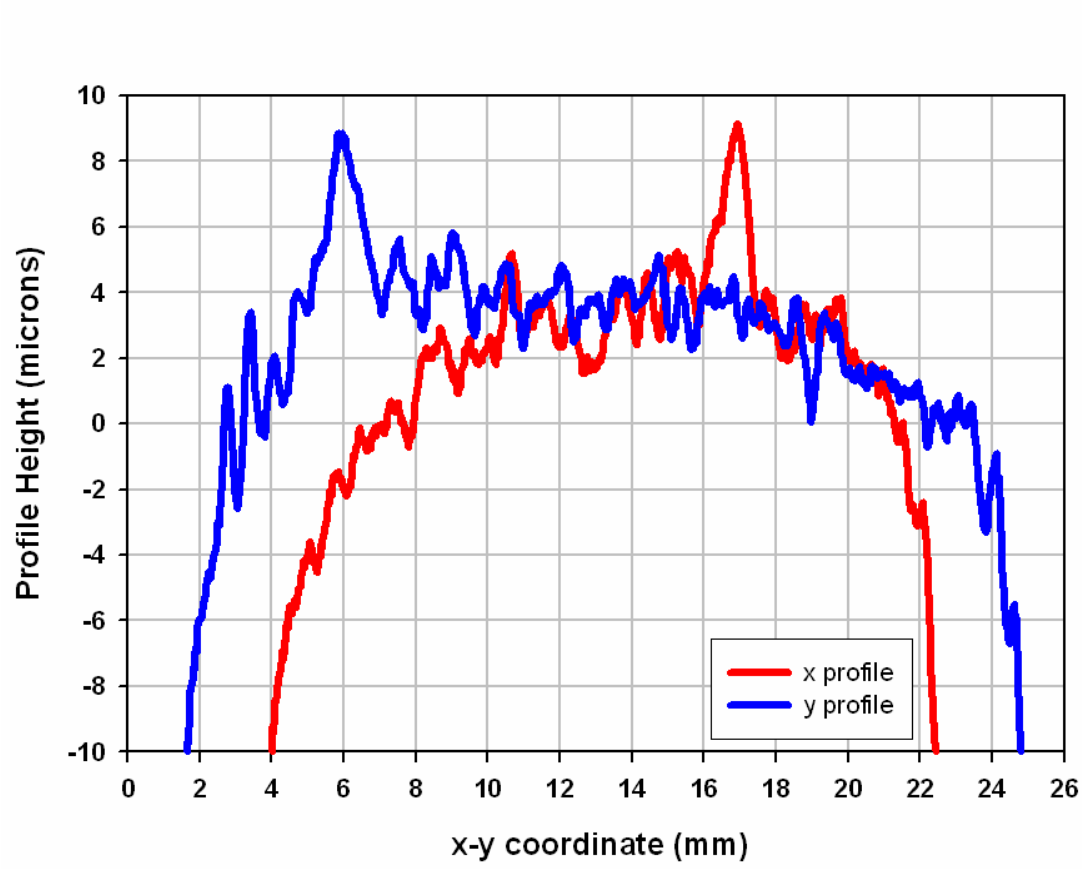

Figure 5.12: The x and y profiles of the delamination in Fig. 5.11.

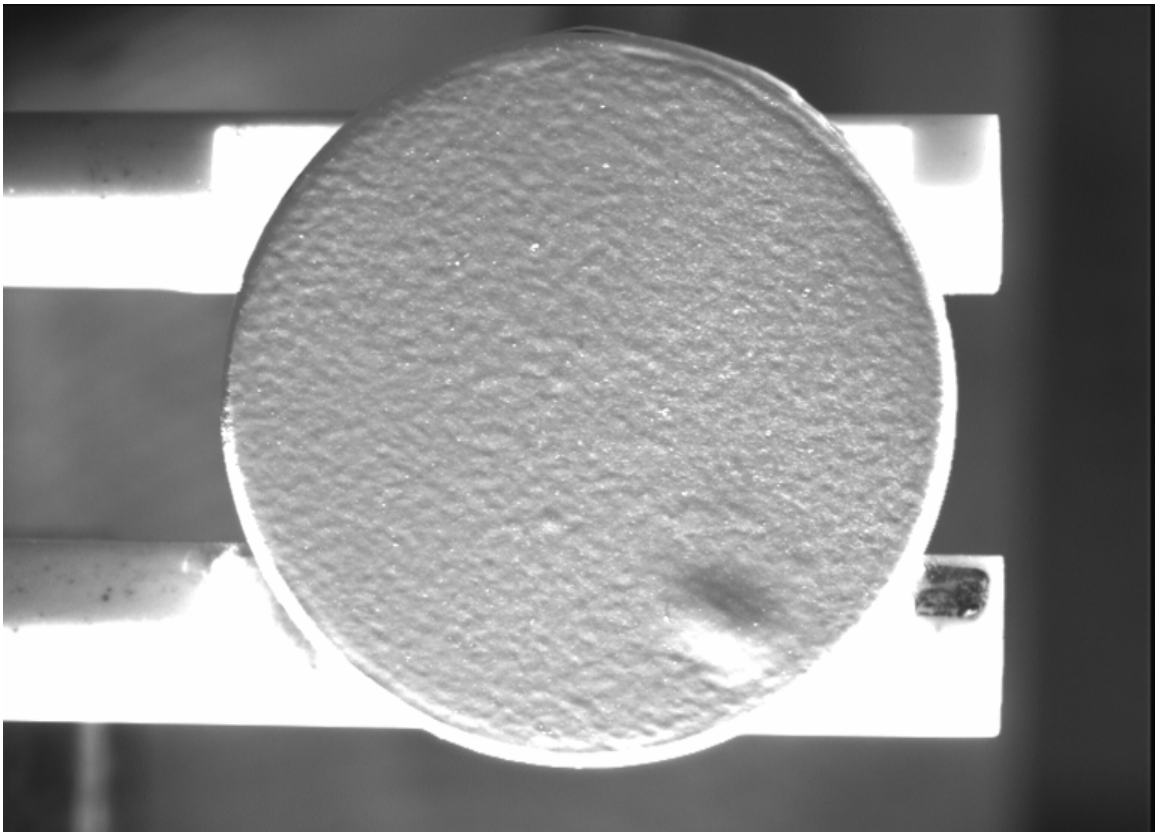

Figure 5.13: A top surface CCD camera image one cycle before the TBC spallation (diameter = 25.4 mm).

CHAPTER 6

TOP COAT CRACKING AND SPALLATION

1. INTRODUCTION

As has been described in previous chapters, thermal cycling of thermal barrier coatings (TBCs) leads to microstructural evolution and damage. Among all the damage that occurs in TBCs, damage in the thermally grown oxide (TGO), top coat, and TGO interface are most critical to the durability of the TBCs. At the end of the TBC life, the accumulation of damage leads to top coat buckling and spallation. If damage in the TGO, top coat, and TGO interface can be tracked as a function of thermal cycling, better life prediction models can be developed.

It is not an easy to trace damage at the TGO layer, top coat layer, and TGO interface. Damage to the TGO layer and TGO interface is covered by the opaque yttria stabilized zirconia (YSZ) top coat. Another challenge is the size of damage. Most cracks

are tens of microns long and sub-microns in width. Therefore, novel methods must be developed to detect and monitor damage in TBCs.

Scanning electron microscopy (SEM) has the necessary resolution to track thru-thickness top coat cracks. These cracks will henceforth be called top coat "vertical" cracks. The top coat already possesses vertical gaps within the columnar structure. Therefore, it is difficult to distinguish between pre-existing columnar gaps and the formation of the top coat vertical cracks, especially with smaller widths. However, as was described in Chapter 5, with only minimal polishing of the top coat surface the columnar microstructure was smooth enough to enable visualization of cracking. Thus, top coat vertical crack formation is studied by interrupting thermal cycling and taking periodic SEM images.

To investigate TGO and TGO interface damage with better time resolution, images of the TBC top coat were captured by a charge couple device (CCD) camera during every cooling cycle. The setup for acquiring these images was described in Chapter 4. A Nikon lens (Micro-Nikkor 105 mm f/2.8D) was used with a Pulnix CCD camera (TM-9701), and a National Instruments frame grabber (IMAQ PCI-1424) captured images 6 times per minute. For better contour resolution a Zeiss white-light

source (Schott KL 1500 electronic) was directed through fiber optics to be almost parallel to the top coat surface. Either compressed air or a small fan was used to more quickly cool the specimen and to minimize image distortion caused by thermal convection.

The CCD images during the final cooling cycle are analyzed to provide new insight into the buckling (spallation) process. Spallation propagation is dependent on where the critical delamination is located. From all of the experiments it is found that there are two possible locations of the critical delamination. The size of the critical delamination is used with a buckling formula to calculate the critical top coat strain.

The extent of TGO interface cracking can be estimated from the top coat CCD images. Due to the large thickness of the substrate, the substrate controls the overall thermal expansion/contraction of the TBC specimen. However, when interface cracking occurs, the top coat is no longer constrained to the substrate. Therefore, when the TBC specimens are cooled, the separated top coat region will not contract in the same fashion as the bonded top coat region.

Digital image correlation (DIC) is a method for calculating displacements and displacement gradients by using homogeneous deformation fields to map deformed image subsets onto undeformed images [73-78]. Since DIC has *in situ* and non-contact

capability, DIC can be used to monitor the thermal contraction behavior of the entire top coat of the TBC specimens. The CCD images taken during the cooling portion of each cycle are used for this purpose. Regions with intact interfaces contract differently from regions with separated interfaces, and therefore the DIC technique shows which region of the interface is damaged. The size of the critical delamination is readily obtained with this technique.

2. SEM ANALYSIS OF TOP COAT VERTICAL CRACKING

All SEM images were collected with a Hitachi S-4300. As mentioned earlier, the YSZ top coat was polished to enable viewing of cracks. The surface of the specimen was not coated with conductive material, and therefore most images have evidence of charging. The specimen was marked so that features of interest could be found from one session to the next. All edge-part SEM micrographs shown in this chapter are oriented such that the right hand side of the image is closer to the edge of the TBC specimen.

Figures 6.1a and 6.1b show the as-coated top coat surface before polishing and at lower and higher magnification, respectively. Fig. 6.1a shows two deposition defects. Such defects were relatively common. Fig. 6.1b shows a detailed view of Fig. 6.1a and

how individual columns construct the unique top coat structures. Fig. 6.1b clearly shows how the top coat consists of distinct columns.

Deposition defects in the TBC top coat are common. Figure 6.2a is a magnified view of a deposition defect shown in Fig. 6.1a. After cycling the columns that form the deposition defect fall out and the defect becomes a pit like the one shown in Fig. 6.2b. Individual columns are generally around 10 μm wide. However, the columns in a defect are around 3 ~ 5 times wider than normal. In addition the individual columns in the defect have a more tapered geometry. Theses tapered columns form a cone shaped geometry with columns that are not normal to the specimen surface.

Recall from Chapter 5 that polishing of the top coat was accomplished by sanding with 400, 600, 1000, and 2000 grit sand papers. Figures 6.3a and 6.3b show the un-cycled, polished top surface near the middle and edge of the specimen. It was not desirable to take off too much top coat materials and therefore there are large sections that are not perfectly smooth. In addition, Figures 6.3a and 6.3b also show many pin holes from gaps between columns and deposition defects. However, most importantly for this study, there are no visible cracks on the polished surface.

Since the top coat is also deposited on the sides of the specimens, the columns have to transition from being perpendicular to the top to perpendicular to the side. Therefore the edge of the specimen is tapered downward and it would take significant polishing to smooth the very edges. For the specimen shown in Fig. 6.3b, it is seen that the unpolished edge of the specimen has a width of around 350 μm. This indicates that there is a transition in column orientation at around 350 μm away from the outermost edge.

Figure 6.4 shows a detailed view of the 350 μm wide unique edge feature before the polishing of the top coat. There are two regions of this unique edge feature. The first region is from the outmost edge to around 120 μm. This is the thickness of the top coat along the edge of the specimen. The second region is from around 120 μm to 350 μm and is the region where column orientation transitions from perpendicular to the top to parallel to the top. These regions are significant because of the cracks that initiate in these regions during thermal cycling.

Figures 6.5a and 6.5b show the top surface of the polished specimens near the middle and edge after 32 thermal cycles at 1200 ºC. In comparing Figures 6.5a and 6.5b to the un-cycled polished specimen in Figures 6.3a and 6.3b, it is seen that vertical cracks

are present throughout the top coat [111]. However, the middle-part of the specimen shows more cracks and wider cracks compared to the edge-part. The width of the cracks in the middle is around 0.2 μm. It seems that the vertical cracks often originate from deposition defects and connect deposition defects together [111].

Sudden convex curvature formation during thermal cycling was documented in Chapter 5. This curvature change was especially prominent in the earlier stages of TBC life. The top coat vertical cracks shown in Figures 6.5a and 6.5b are most likely necessary to accommodate convex curvature. The fact that cracks remain open at room temperature despite compressive residual stresses is consistent with the observation of curvature. It is also likely that the top coat vertical crack formation seen in Figures 6.5a and 6.5b are the source of the earlier cycle AE events described in Chapter 4.

Figures 6.6a and 6.6b show the same middle-part of the polished top coat surfaces after 100 and 634 thermal cycles. Compared to vertical cracks on the specimen cycled 100 times, the top coat surface that experiences 634 cycles has more noticeable vertical cracks. The vertical top coat cracks in the middle of the specimen were formed during the initial 32 thermal cycles and stay almost unchanged until the 200^{th} cycle. The middle-part vertical cracks started to become more prevalent and wider after around the

300th cycle. This observation is consistent with the Chapters 4 and 5 results showing an increase in AE events and top coat convex curvature after the 300th cycle. However, at the same time it is noted that most of the vertical cracks on the middle region of the top coat surface formed during the initial 32 thermal cycles and little new crack formation was detected during further thermal cycles. Given the fact that the there are no new cracks forming after the 300th cycle, shear lag theory [112] would indicate that saturation cracking occurred in the first 32 cycles and the interfacial shear strength did not change or has decreased.

Compared to vertical cracks in the middle of the specimen, the edge-part cracks show more distinct changes as thermal cycling progresses. The SEM images in Figures 6.7a and 6.7b show edge cracks that had formed by the 200th cycle. After the 200th cycle, compared to middle-part vertical cracks which were stationary, more visible and bigger vertical cracks had formed along the edge of the top coat. Most edge cracks were oriented circumferentially.

Initially it was found that the edge-part cracks were present at either 120 μm from the edge or 350 μm from the edge. Recall that these two dimensions are significant because coating is 120 μm thick and the column orientation begins to change at 350 μm

from the edge. Cracks that form 120 μm from the edge will be called "Type I" cracks and cracks at 350 μm will be called "Type II" cracks. It is noted that when Type I cracks formed (*e.g.*, Fig. 6.7a), there were no cracks in the region between 120 μm and 850 μm from the specimen edge. Only at distances more than 850 μm from the specimen edge were vertical cracks again visible.

Fig. 6.7b shows Type II edge vertical cracks which were formed at the 350 μm from the specimen edge. In the presence of Type II cracks, there was no region without cracking. The cracks were present at all radial locations greater than 350 μm from the edge. Compared to Type I vertical cracks, the Type II edge cracks are generally wider.

The cracks in Figures 6.7a and 6.7b seem to have formed due to coefficient of thermal expansion (CTE) misfits between the top coat and substrate and sintering of the YSZ. During the heating of the TBC specimen, the top coat layer experiences tensile stresses since the substrate has a higher CTE than the top coat. After sintering of the YSZ, the top coat loses its strain tolerance and vertical cracks form. It also has been suggested that the vertical cracks originate from pre-existing bond coat grain boundary ridges and grow wider as the TGO layer thickens [37].

It was found that the regions with Type I cracks (at 120 μm) did not have Type II cracks (at 350 μm) and *vice versa*. Damage is likely at 120 μm from the outer edge because of the changing column alignment and the mixed-mode loading. After 400 cycles approximately 60% of the circumference at 120 μm from the outmost edge was either cracked or chipped. About 30% of the circumference at 350 μm from the outmost edge was cracked after 400 thermal cycles. After 634 thermal cycles, in the type I edge crack case, there were vertical cracks which cover between 850 μm and 1650 μm away from the outmost radius. In the type II edge crack case after 634 thermal cycles, vertical cracks started from 350 μm inner radius from the outmost edge and extended up to 1000 μm toward to the center of the specimen.

Figures 6.8a, 6.8b, and 6.8c show top coat vertical cracks after 300, 500, and 634 thermal cycles, respectively. The right hand side of all three micrographs is close to the edge of the specimen. All micrographs show large cracks that are overall oriented circumferentially. These large circumferential cracks are zigzagged, and there are smaller cracks at various orientations between major cracks.

Figures 6.9a and 6.9b show what the 120 μm Type I crack looks like after 300 cycles and 500 cycles, respectively. With this level of detail it is seen that the surface

discontinuity is not at quite 120 μm from the specimen edge. However, it is expected that the base of the crack is at the corner of the specimen edge and is therefore at 120 μm away from the outmost edge of the coated specimen. After 300 cycles, the 120 μm inner radius cracks have advanced outwards by around 10 μm. It is believed that some TGO growth and some delamination are responsible for this movement. From unaided visual observation of all experiments, the 120 μm edge cracks usually become visible between 300 and 350 cycles.

After further cycling, 120 μm Type I cracks cause the top coat on the side of the specimen to separate from the substrate. Figures 6.10a and 6.10b show two different edge crack separations after 550 cycles and 634 cycles, respectively. These cracks are located close each other, however it is believed that they are not connected. The separation that occurred after 634 cycles also shows a vertical crack which runs through the thickness of the YSZ layer on the side surface.

3. IMAGING OF DELAMINATION PROPAGATION: THE DEVELOPMENT OF SPALLATION

3.1 TYPES OF TBC SPALLATION

Top coat buckling leads to top coat spallation and is the final phase of the TBC life. Buckling of the top coat releases the compressive strain energy stored in the TGO and top coat layer. Based on the location of the initial buckling, the final spallation can be categorized into two cases: buckling from the largest interior delamination and buckling from the largest edge delamination [113]. The formation of the delamination spot and failure characteristics are somewhat different for the two cases.

In the 1st case, the center of the biggest delamination spot is usually located at around two-thirds of the radius of the TBC specimen. It was mentioned that the Type I edge cracks are more common and that regions with Type I cracks also have cracks at 850 μm to 1650 μm from the specimen edge. Delamination seems to initiate in the region just beyond 1650 μm from the outer edge of the specimen. During spallation, the interface crack propagates by mode I fracture due to buckling forces.

The 2nd spallation location is associated with a Type II edge crack. It was mentioned that Type II edge cracks are present from 350 μm to 1000 μm from the edge of

the specimen. Critical delaminations initiated just inside of this annulus. Just one or two cycles before spallation, the critical delamination advances towards the edge of the specimen and creates an edge delamination. The creation of the edge delamination produced many AE events. Once the delamination was large enough, buckling occurred.

Out of six experiments the 1st case occurred four times. There are two reasons why the 1st case buckling is slightly more common than the 2nd case buckling. The first reason comes from the higher percentage of Type I edge cracks. The second reason comes from the geometry of the delamination. Since the edge delamination is near a free surface, as compared to a delamination that is surrounded by intact top coat, there is less energy available to propagate a buckle.

3.2 DETAILED OBSERVATIONS OF CASE 1 SPALLATIONS

Figures 6.11 and 6.12 show successive images of the top coat surface during the spallation cycle of AE3 and N-AE3. Since they initiate near Type I edge cracks, both of these spallations are classified as Case 1 spallations. Figure 6.13 is a plot of the AE events and temperature profile during the spallation cycle of AE3 (shown in Fig. 6.11). It is seen that there are two very distinct bursts of AE activity. By analyzing the time

resolved CCD images of the top coat, it was found that these bursts correspond to top coat buckling.

Fig. 6.11a shows a critical debond in the upper right corner of the specimen, approximately two-thirds of the radial distance from the center of the specimen, and with a diameter of about 5.5 mm. This debonding was created by the coalescence of the interface cracks at the completion of the 420^{th} cycle out of the 429 total cycles. Fig. 6.11b shows the initiation of the first buckle. The initiation of the first buckle is coincident with the start of the first burst shown in Fig. 6.12a. Fig. 6.11c shows how the buckle is propagating. As seen in Fig. 6.13, this propagation generates many AE events. Fig. 6.11d shows arrest of the first buckle. At this point vertical TBC top coat cracks appeared on the border between the intact and separated interface. These vertical TBC top coat cracks are kink cracks, or in other words interface cracks that deflect into the top coat and extended to the top surface [114]. It is likely that a region with better interfacial bonding aided in arresting the first buckle. From this point to the initiation of the second buckle, the AE activity decreased significantly. With continued cooling, the TGO layer develops larger in-plane compressive stresses due to CTE misfits. These higher stresses are needed in order to initiate a new buckle. Fig. 6.11e shows the progress of the second

buckle. Larger scale buckling of the top coat generated vertical TBC top coat cracks on the upper left corner of the specimen. The propagation of the second buckle again generated many AE events. Fig. 6.11f shows the buckle propagation up to the final spallation and extension of vertical TBC top coat cracks in the middle of the specimen.

The darker spot at the lower left edge of TBC top surface shown in Fig. 6.11a is an edge delamination which developed during much earlier cycles. A similar edge delamination was also observed in the AE1 specimen. During the earlier cycles, this delamination was more apparent than other interior undulation spots. However, the edge delaminations in both AE1 and AE3 did not grow from their initial sizes and did not initiate spallation of the TBC top coat. AE1 and AE3 seem to prove that buckling from edge delaminations requires higher energy.

Fig. 6.12 shows successive images of the top coat surface of the N-AE3 specimen during its spallation cycle. Fig. 6.12a shows the beginning of the first buckle. The cooling cycle time (or temperature) at which buckle propagation began was similar for N-AE3 and AE3. One interesting point in Fig. 6.12a is the existence of two dominant inside debonding spots. Both debonding spots had started to appear 8 cycles before the spallation which happened at 761 cycles. Both debonding spots formed in regions with

the most significant surface roughness. The surface roughness became apparent at around 18 cycles before the spallation. The debonding spot 1 was located at around two-thirds of the specimen radius and had an elliptical shape. The debonding spot 1 coincided well with the AE3 debonding spot in location and general shape. Debonding spot 1 was a product of coalescence of two adjacent delamination spots and became a critical debonding spot just 1 cycle before the spallation. Debonding spot 2 was located at the center of the specimen and had a doughnut shape. Although debonding spot 2 was bigger than debonding spot 1, the first buckle was initiated from debonding spot 1. It seems that for debonding spot 2 the center of the hollow shape was still intact and this geometry prevented buckling.

The initial shape of debonding spot 1 was elliptical. The major and minor axes of debonding spot 1 were 4.8 mm and 2.5 mm, respectively. However, just before the initiation of the first buckle, the debond started in the radial direction and increased the separation in the minor axis direction. Eventually, the debonding spot 1 became more circular with a diameter of 4.8 mm. This diameter is comparable to the diameter of the largest debonding spot in the AE3 specimen.

Fig. 6.12b shows where the first buckle arrested. Although the size of the buckled area between N-AE3 and AE3 (Fig. 6.11d) is different, the timing of the first buckle arrest for both specimens is identical. Unlike for AE3, in N-AE3 the first buckle resumed propagation about 20s after stopping. Fig. 6.12d shows the connection between the first buckle and the debonding spot 2. The first buckle propagated and advanced toward the debonding spot 2 and created the one larger debond that is shown in Fig. 6.12e. Between Figures 6.12e and 6.12f further interface delamination occurred. Fig. 6.12f shows the top coat surface at the end of the spallation cycle.

3.3 DETAILED OBSERVATIONS OF CASE 2 SPALLATIONS

Figures 6.14 and 6.15show successive images of the top coat surface during the spallation cycles of N-AE1and P-AE1. Since the delaminations initiate near Type II edge cracks, both of these spallations are classified as Case 2 spallations. The initiation of the edge delamination which eventually caused spallation in the N-AE1 specimen occurred at the 353 of 577 cycles. Fig. 6.14a shows the start of the interface crack propagation of the edge delamination spot. AE results indicated that just 2 cycles before the spallation cycle, the critical edge delamination shown in Fig. 6.14a was abruptly

formed. The critical edge delamination had a semi-circular shape with a diameter of 4.4 mm.

Fig. 6.14b shows initiation of the first buckle from the edge delamination spot. The temperature of the specimen was around 50 ºC. In comparison to the 130 ºC temperature that caused buckle initiation in Case 1 spallations, this is a relatively low temperature. This indicates that higher driving force is needed to propagate edge delaminations.

Fig. 6.14c shows the propagation of the first buckle from the edge delamination spot. Fig. 6.14d shows the first buckle at its maximum size of the first buckle, and Fig. 6.14e shows the formation of a new delamination region. The new delamination for a second buckle is shown in Fig. 6.14f. In Fig. 6.14g, two buckles were arrested by intact interface. As was the case with the specimen in Fig. 6.11f, along the intact and separated border, kink cracks developed. Fig. 6.14h shows the completion of the spallation cycle and more kink cracks which ran along the whole diameter of the N-AE1 specimen.

Figure 6.15 presents another example of buckling failure from an edge delamination in P-AE1. Fig. 6.15a shows an obvious undulation spot very close the edge

of the specimen and at 12 cycles before the spallation cycle. Fig. 6.15b is the last image of the cycle before the spallation cycle. The critical delamination in Fig. 6.15b is roughly elliptical in shape and has a major and minor axis of 4.5 and 2.7 mm.

Fig. 6.15c shows that the top coat had already buckled somewhere between the last image of the previous cycle and 80 seconds into the cooling portion of the spallation cycle. This buckle was stationary until the time shown in Fig. 6.15d when the temperature reached around 71 ºC. This temperature is also lower than the 130 ºC that caused buckling in Case 1 spallations.

The buckle shown in Fig. 6.15e was stationary until around 21 minutes and 20 seconds into the cooling cycle. At 26 minutes and 50 seconds the buckle reached its maximum cooling cycle size and is shown in Fig. 6.15f. The spallation shown in Fig. 6.15f is relatively small. Images were taken for 10 hours longer but no further spallation was observed. However, after sitting at room temperature for a couple of days, it was found that the amount of spalled material had increased. During still longer time at room temperature, the top coat became almost completely delaminated. This phenomenon was typical for all TBC specimens. It seems that residual stresses in the system enabled continued spallation over long periods of time.

3.4 POST FAILURE OBERSERVATIONS

In this section observations of the spalled surfaces are shown. In general, there were only differences in the amount of intact and separated areas. It was found that TBC spallation happens at both the YSZ/TGO and TGO/bond coat interface [21, 115].

Figure 6.16a shows the N-AE2 specimen after the spallation of the top coat. The upper part of the specimen image has initially intact interface and the lower part of the specimen image shows interfaces that separated during the spallation cycle. As was mentioned in Section 3.3, a few days after the images were taken, the intact interface area also spalled. Figure 6.16b shows two distinct regions in the spalled section. The upper region is covered with white island shape regions while the lower region shows no such regions. The lower region is the spalled region in Fig. 6.16a and is where spallation happened during the final cooling cycle of TBC life. The upper region is the intact region in Fig. 6.16a and was exposed days after the cyclic heating ended.

Figures 6.17a and 6.17b show backscattered electron (BSE) SEM micrographs of post spallation surfaces. It is noted that heavier elements will appear lighter in BSE images. The finely distributed white areas are YSZ (ZrO_2, At. Weight = ~41) top coat remnants on top of the TGO (Al_2O_3, At. Weight = ~20.4) layer, and dark gray parts are

intact TGO on top of the bond coat (Pt-NiAl, At. Weight = ~42.5) layer. The large white areas are exposed bond coat regions that resulted from TGO/bond coat interface failure. It has been reported that TGO/bond coat interface separation happens along bond coat ridges [116]. Thru-thickness cracks in the TGO layer are also visible in Fig. 6.17b. There is no YSZ present adjacent to the TGO cracks. It also appears that the TGO cracks coincide with grain boundary ridges in the bond coat.

It is interesting to note that TGO/bond coat interface delamination happens only after the specimen has been sitting for an extended period of time. During thermal cycling delamination/buckling occurs only along the YSZ/TGO interface. It has been reported that YSZ/TGO interface delamination is dominant when sever ratcheting exists and TGO/bond coat interface delamination is dominant when little ratcheting exists [21]. Although it is possible that moisture plays a role and/or that the higher energy available at room temperature plays a role in activating TGO/bond coat interface failure, detailed understanding of the observed interface-switching is still lacking.

4. INTERFACE DELAMINATION DETECTION USING DIGITAL IMAGE CORRELATION (DIC)

4.1 TOP COAT DAMAGE DETECTION BY DIC

During cooling, TBC specimens experience thermal contraction. Since the TBC substrate is much thicker (~30 times) than the top coat layer, the substrate controls the overall thermal contraction when TBC specimens are cooled. If the TBC specimen is undamaged, the thermal strain in the top coat layer should be uniform. However, when interface cracks are present, the top coat is no longer uniformly constrained. The difference in CTE, α, between the substrate (α ~18.0 x $10^{-6}/^{o}$C) and top coat (α ~12.0 x $10^{-6}/^{o}$C) is ~6.0 x $10^{-6}/^{o}$C. So, when the TBC specimen is cooled, delaminated top coat regions will not contract as much as bonded top coat regions.

Figure 6.18 shows a contour map of y-direction thermal contraction strains in the AE3 specimen. Two consecutive top coat images, taken one cycle prior to TBC spallation, were used in DIC codes to produce Fig. 6.18. The first image was taken at 200 °C, and the second was taken at 40 °C. The contour map shows relatively uniform compressive y-direction top coat strains except for in the upper right corner of the specimen. This region corresponds to the position of the largest debonding spot shown in

Fig. 6.11a. With extensive DIC calculations at each cycle, this particular undulation spot region was traced back in time, and it was found that the strain differences were noticeable as early as the 190th cycle. Note that no undulation was visible using the darkfield-like CCD images until much later in the specimen's life. Furthermore, the 190th cycle is coincident with the start of the third region in Fig. 4.3 where AE events slowly increase again.

The strains associated with the largest undulation region were initially less compressive and were finally tensile. A separated interface would explain why the strains were less compressive before the generation of a visible undulation. After the undulation became apparent in the video images, DIC strain calculations on this spot yielded tensile strains. For the undulation to be visible in the video images, it must have enough out-of-plane displacement or "bending" to influence the way light is reflected towards the camera lens. The outward bending of the separated top coat would generate the tensile strains that were calculated by the DIC.

4.2 BUCKLING CRITERIA

Buckling of the top coat happens when compressive forces exceed the delaminated top coat's critical load. Since the spallation causing delamination became

circular just before the buckling, the buckling analysis can be made with a circular delamination. The delamination can be modeled as an isotropic circular plate under uniform radial edge compression with clamped edges. For delaminations with $0.0 < h/R < 0.15$, the formula for the elastic stability is as follows [94]:

$$\sigma = 1.1 \times E\left(\frac{h}{R}\right)^2, \qquad \text{(Eq. 6.1)}$$

where σ is the critical stress, E is the elastic modulus of the top coat, h is the thickness of the top coat, and R is the radius of the circular delamination. For the current TBC specimens, h is 120 μm and E is taken to be a post-sintered value of 100 GPa. For the AE3 spallation, R is 2.8 μm. Application of Eq. 6.1 results in a top coat, in-plane compressive strain of ~0.2%. When the top coat reaches this strain level at the given delamination size, buckling will occur.

DIC was used to determine the average thermal contraction strain in the top coat during cooling from 1200 ºC. Images taken at 1 minute intervals were used in the calculation starting from 2 minutes of cooling and continuing until the full 23 minutes of cooling. Figure 6.19 shows the results of the DIC calculations with "Spallation-1" which is 1 cycle before spallation and "Spallation+3" which is 3 cycles after spallation. For

Spallation+3 the calculation was performed on a region that is assumed to be detached from the substrate. For reference purposes, temperatures of the TBCs were reported along with the strain calculations.

Spallation-1 is the thermal contraction strain of the top coat combined with the substrate and is well matched with the thermal contraction of the substrate alone. Spallation+3 is the thermal contraction strain of free standing YSZ top coat material. The curve for "Sp-1 – Sp+3" is the difference between Spallation-1 and Spallation+3 and represents the strain that is exerted *on* the top coat (by the substrate) during the spallation cycle. As seen in Fig. 6.19, the top coat compressive strain is ~0.2% at 7 minutes after the initiation of the cooling period. This top coat strain value agrees well with the value found from Eq. 6.1.

5. CONCLUSIONS

During thermal cycling, the top coat layer develops vertical cracks. These cracks are primarily at the center and the edge of the top surface. Curvature causes development of the center cracks, and these cracks formed during the cooling portions of earlier cycles. CTE misfits and sintering of the YSZ caused the edge cracks.

Vertical top coat cracks in the top coat are prominent around the edges of the specimen. For almost the entire circumference of the specimen only two locations for the edge cracks were observed. The location of the edge crack affected subsequent interior cracking. It is believed that the open vertical cracks make the top coat more compliant and therefore there is less energy available for buckling (spallation). After a critical delamination formed, buckling occurred just inside of the interior, vertical crack regions. Since there were two different locations for the interior vertical cracks, spallation was also found to initiate at one of two different general locations.

TBC spallation has been observed at both the YSZ/TGO and TGO/bond coat interface. While delamination/buckling during the last cycle of thermal loading occurs only along the YSZ/TGO interface, TGO/bond coat interface delamination happens only after extensive time at room temperature.

DIC calculations were performed to identify critical delaminations. The DIC method is capable of finding sub-surface damage well before it is visible with videography. Calculations have shown that initially circular delaminations with radii of 2.0-2.5 mm will buckle when under compressive strain of ~0.2%. The critical debonding

size and strain value were confirmed by the image measurements and with DIC calculations.

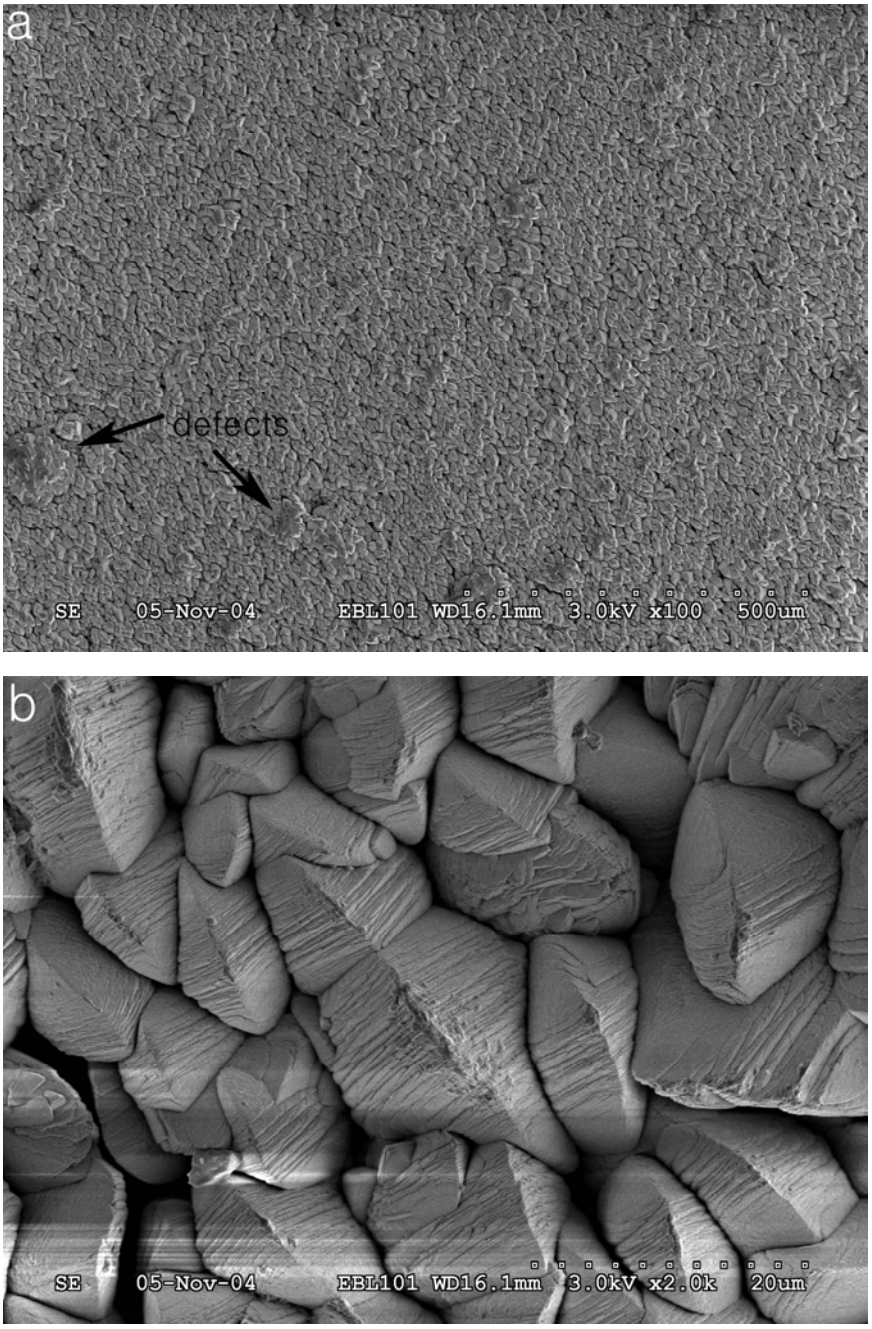

Figure 6.1: Micrographs of the as-coated top coat surface before polishing at (a) x100 and (b) x2.0k magnification.

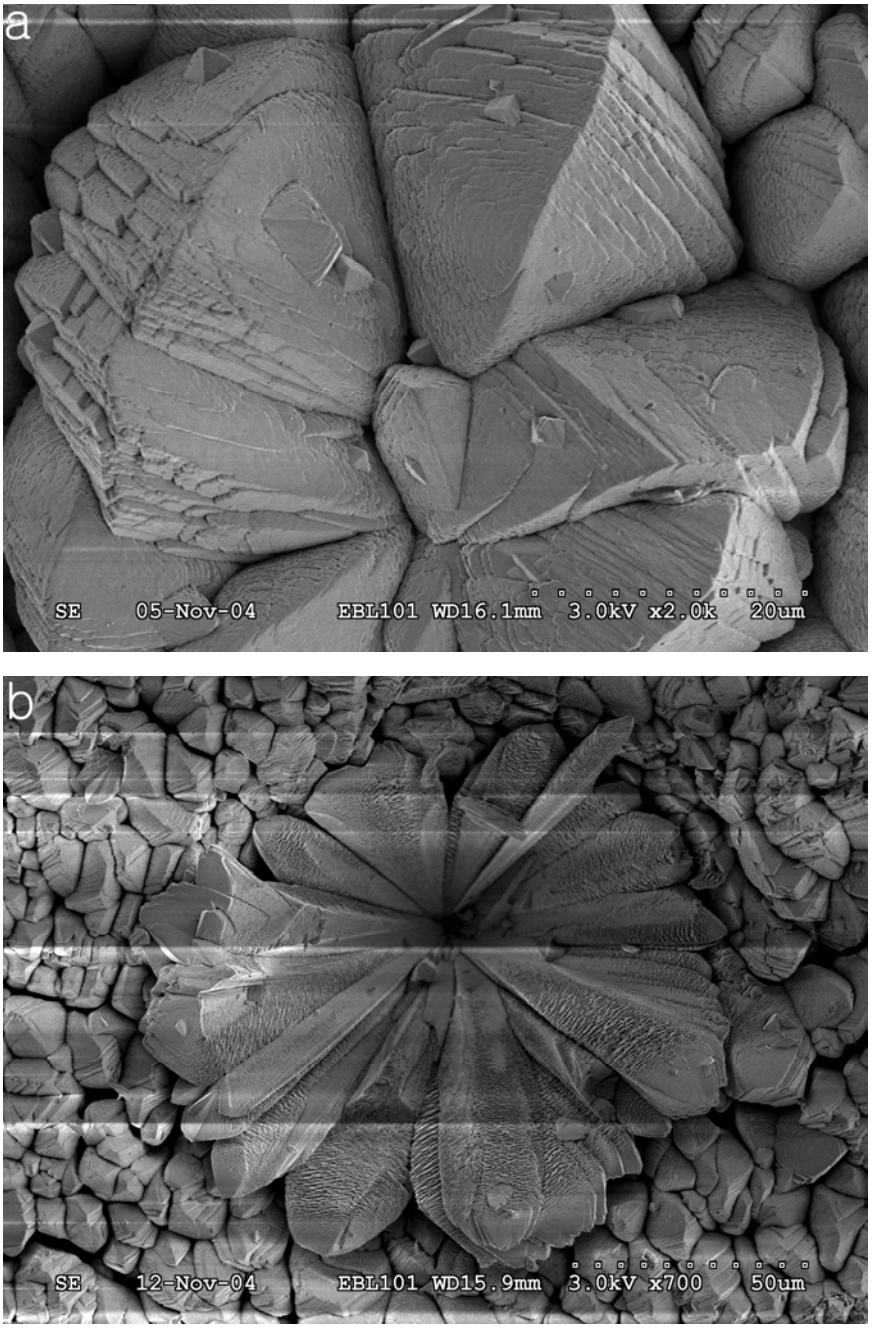

Figure 6.2: Micrographs of (a) individual columns at a defect site and (b) a pit caused thermal cycling of a defect.

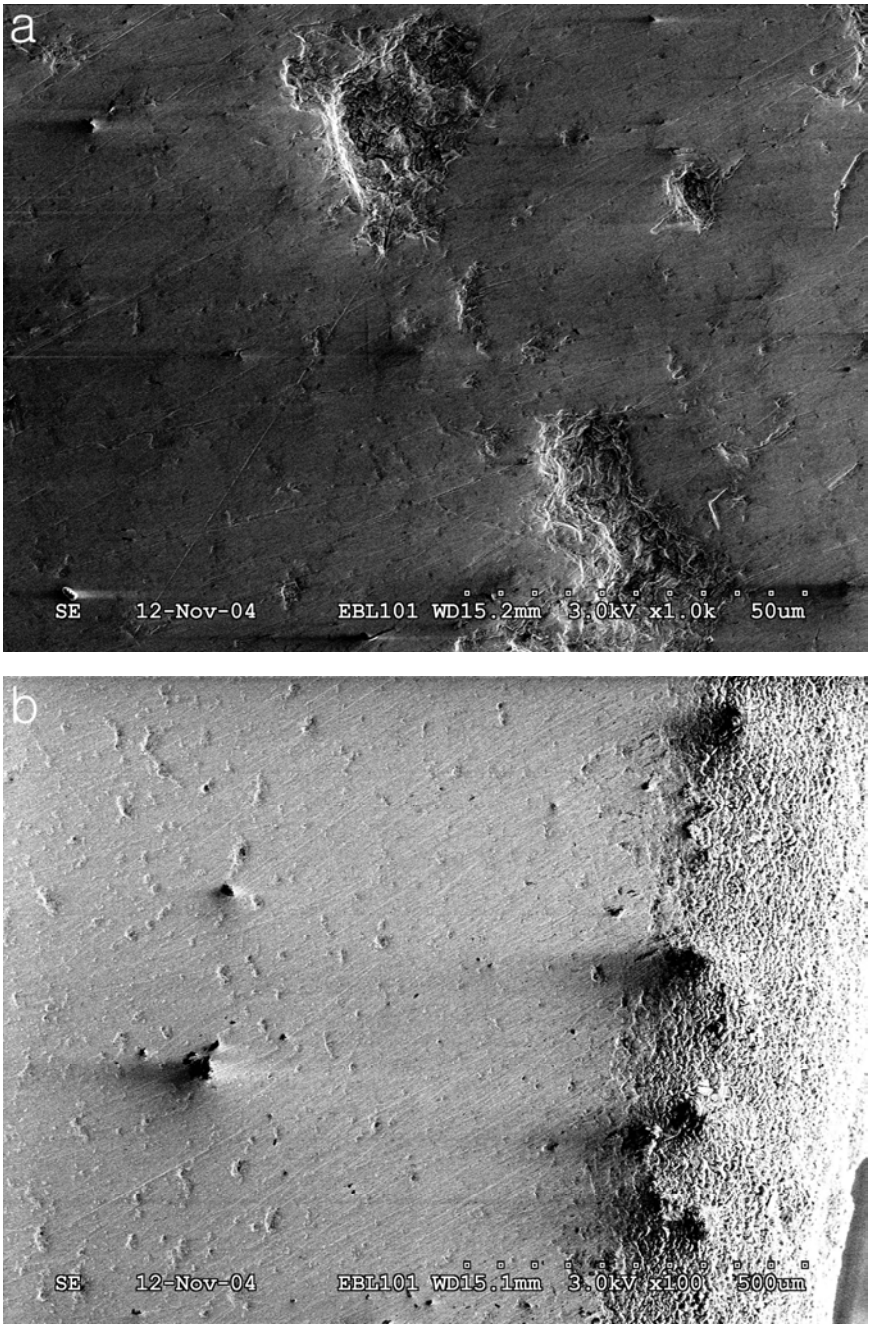

Figure 6.3: Micrographs of the un-cycled, polished top coat surface near the (a) middle of the specimen and (b) edge of the specimen.

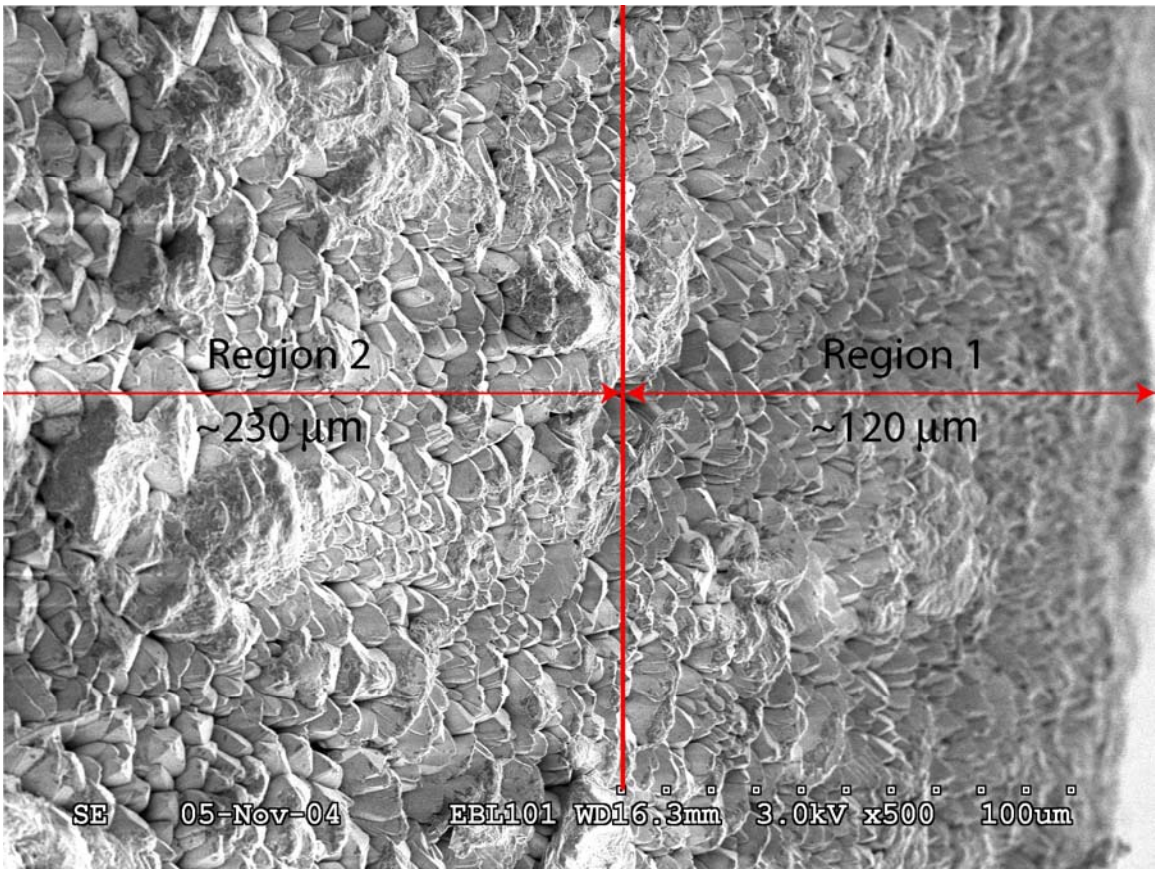

Figure 6.4: A micrographs near the edge of a specimen and showing how the edge of the specimen can be divided into two regions.

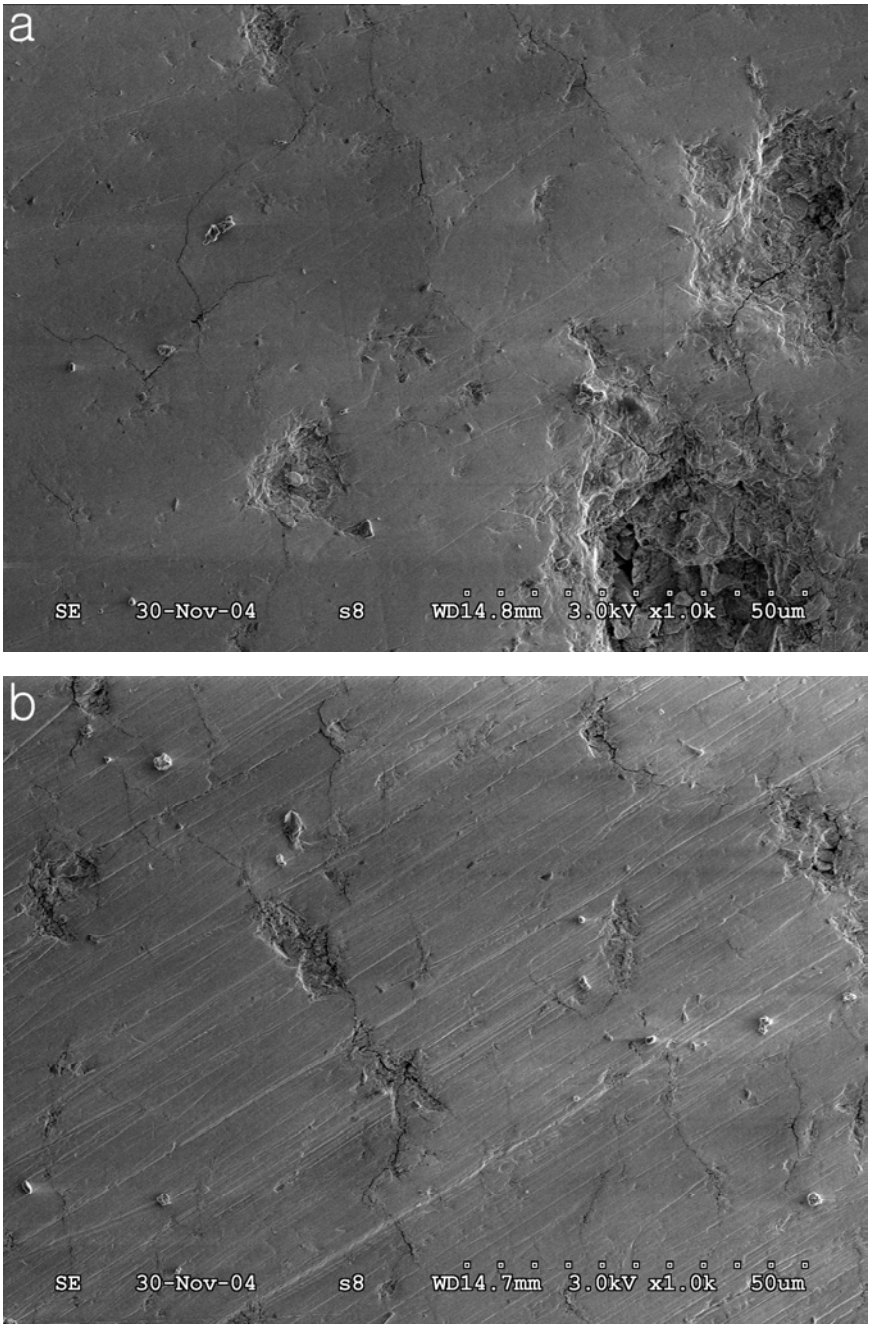

Figure 6.5: Micrographs of the polished top coat surface after 32 cycles and at (a) the middle-part and (b) the edge-part of the specimen.

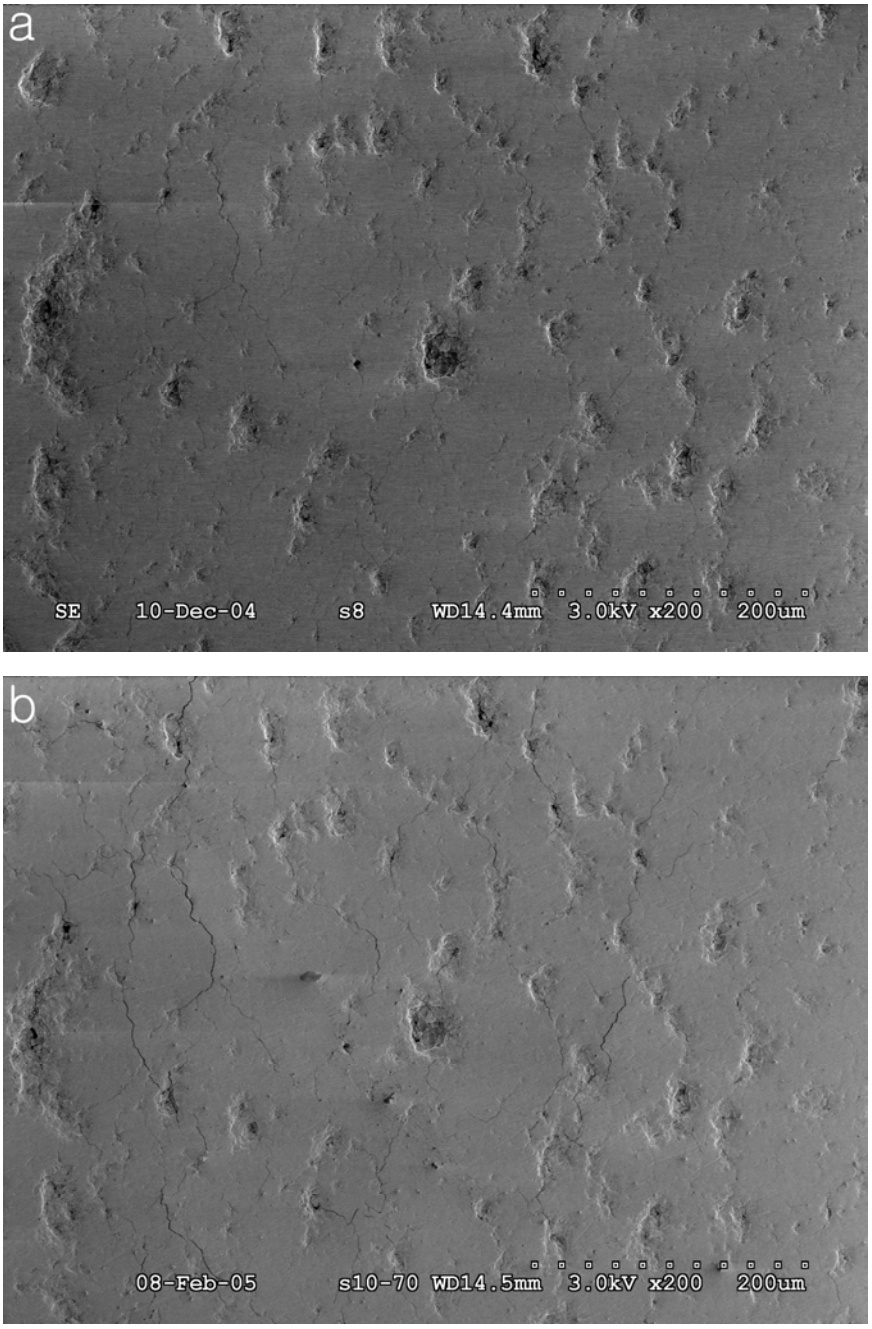

Figure 6.6: Micrographs from the middle-part of the polished top coat surface after (a) 100 and (b) 634 thermal cycles.

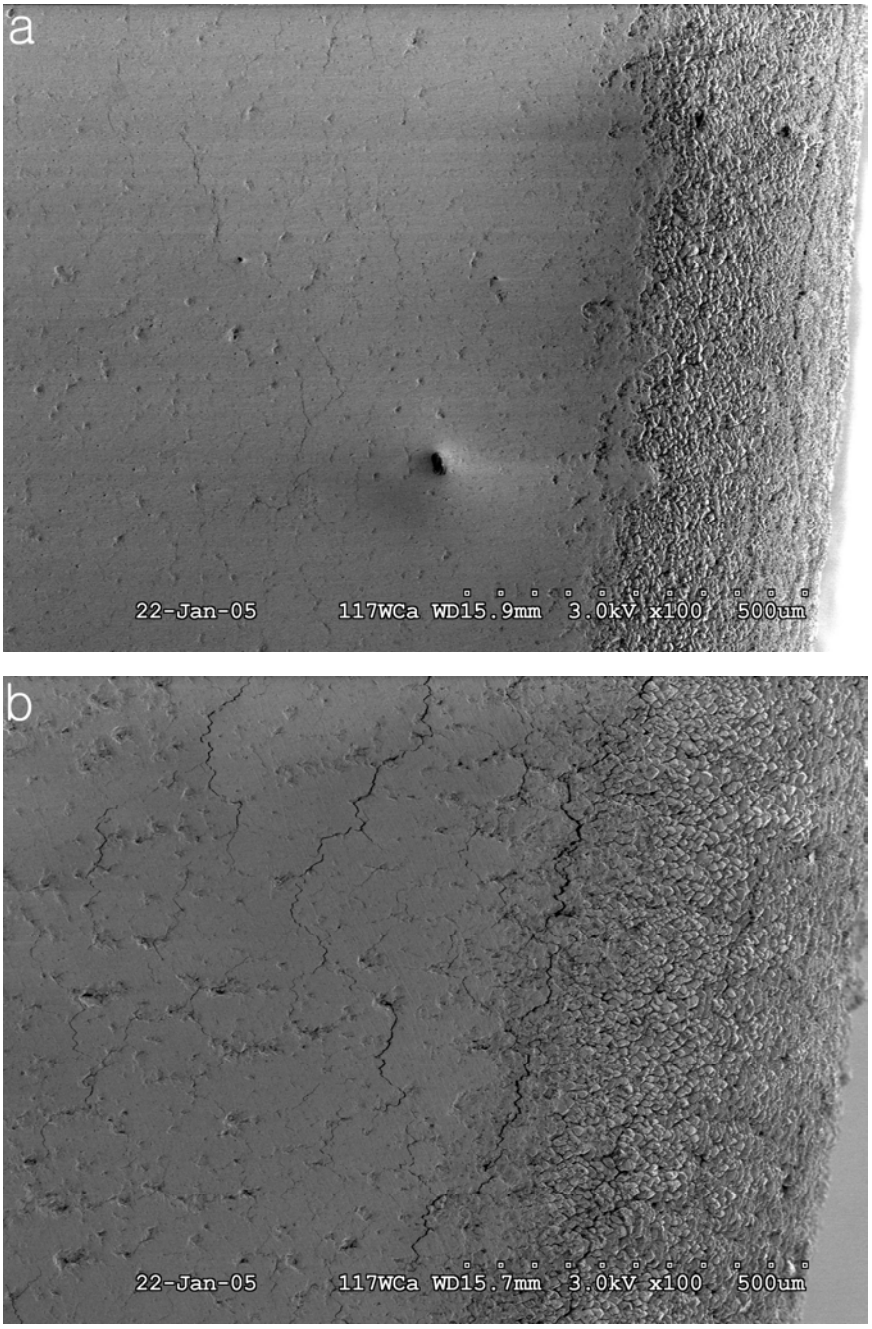

Figure 6.7: Two typical types of edge cracks after 200 cycles: (a) major cracks at 120 μm and (b) major cracks at 350 μm away from the outmost edge.

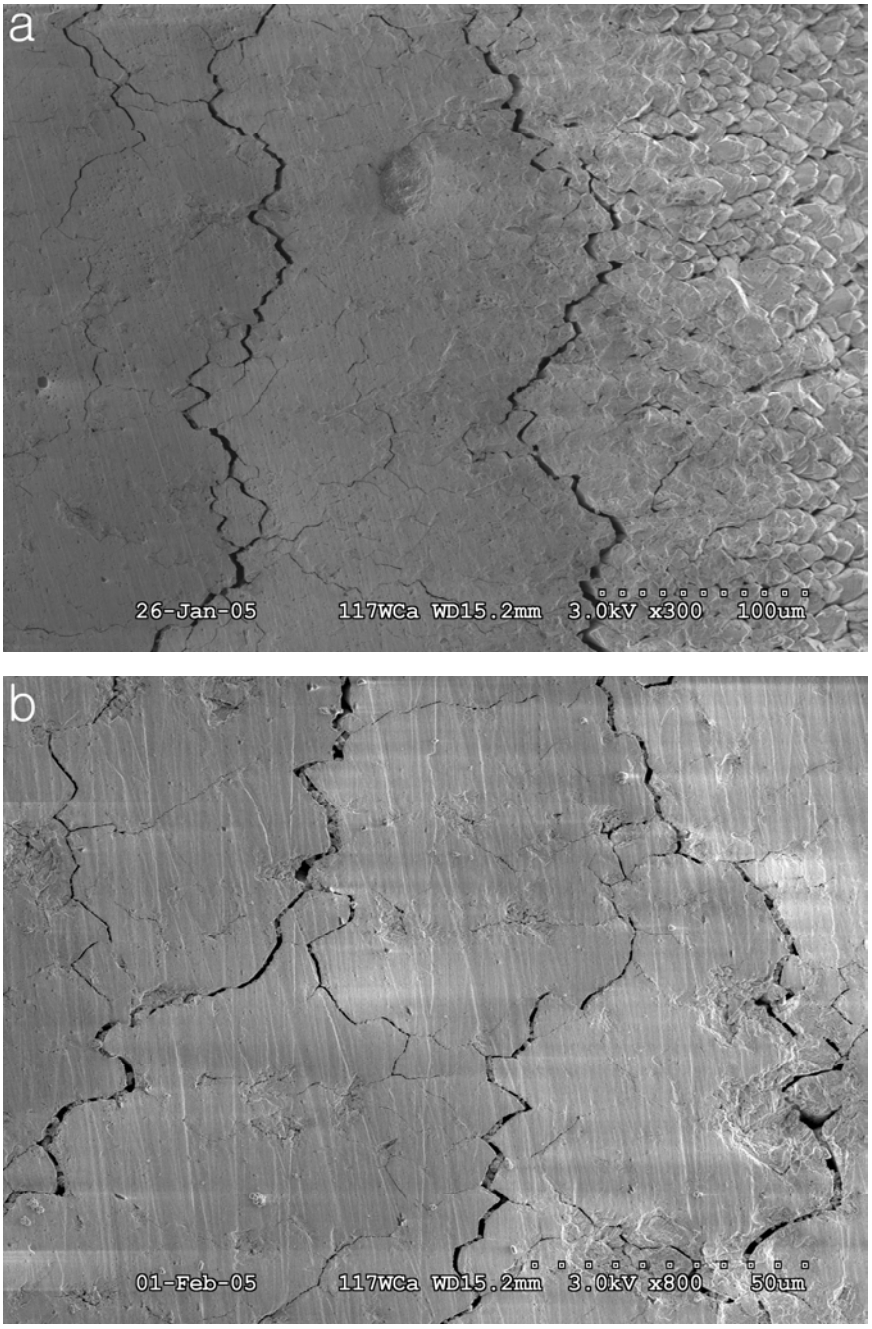

Figure 6.8: Circumferential edge crack formation after (a) 300, (b) 500, and (c) 634 cycles.

Figure 6.8 continued

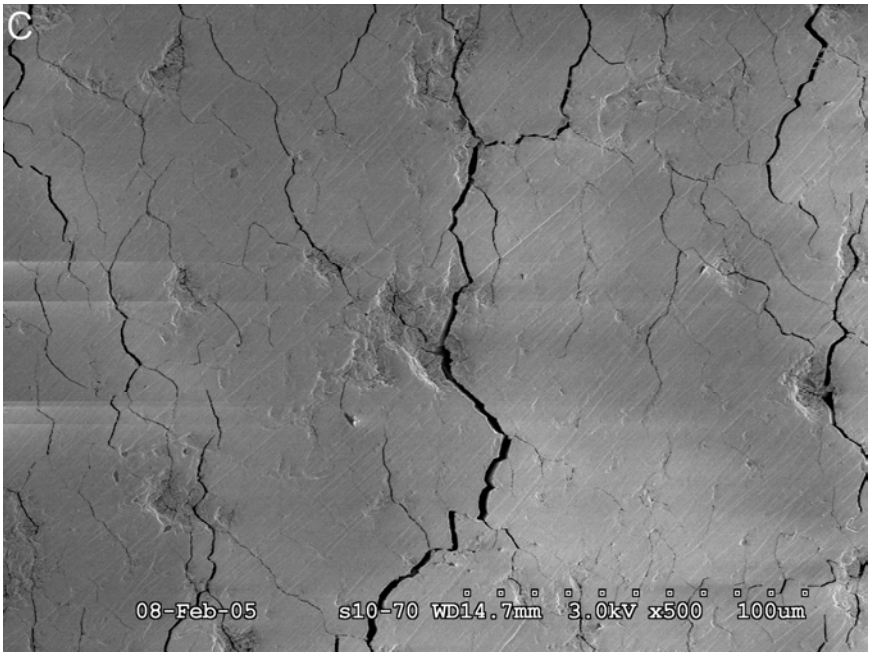

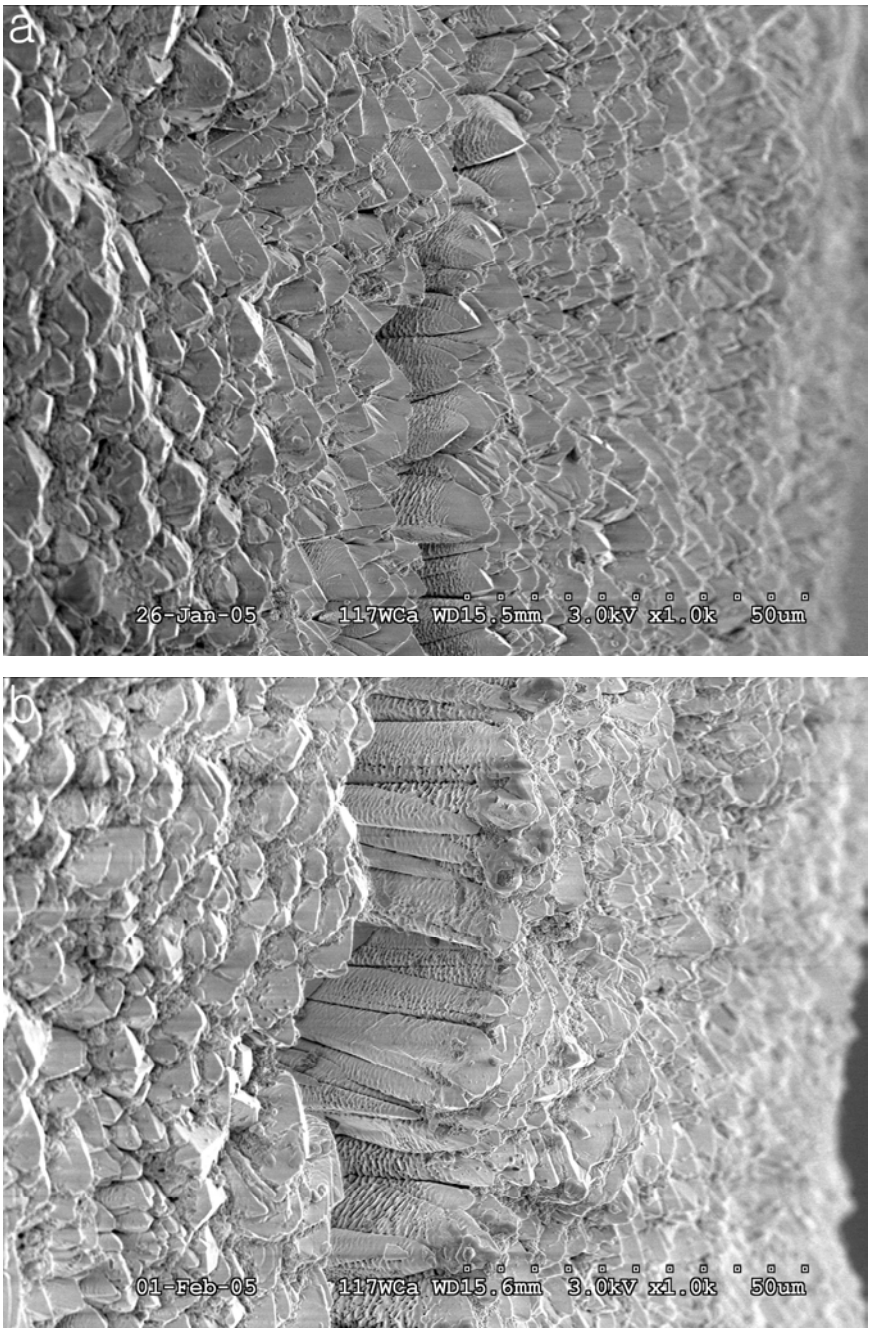

Figure 6.9: Magnified view of the 120 μm inner radius cracks after (a) 300 cycles and (b) 500 cycles.

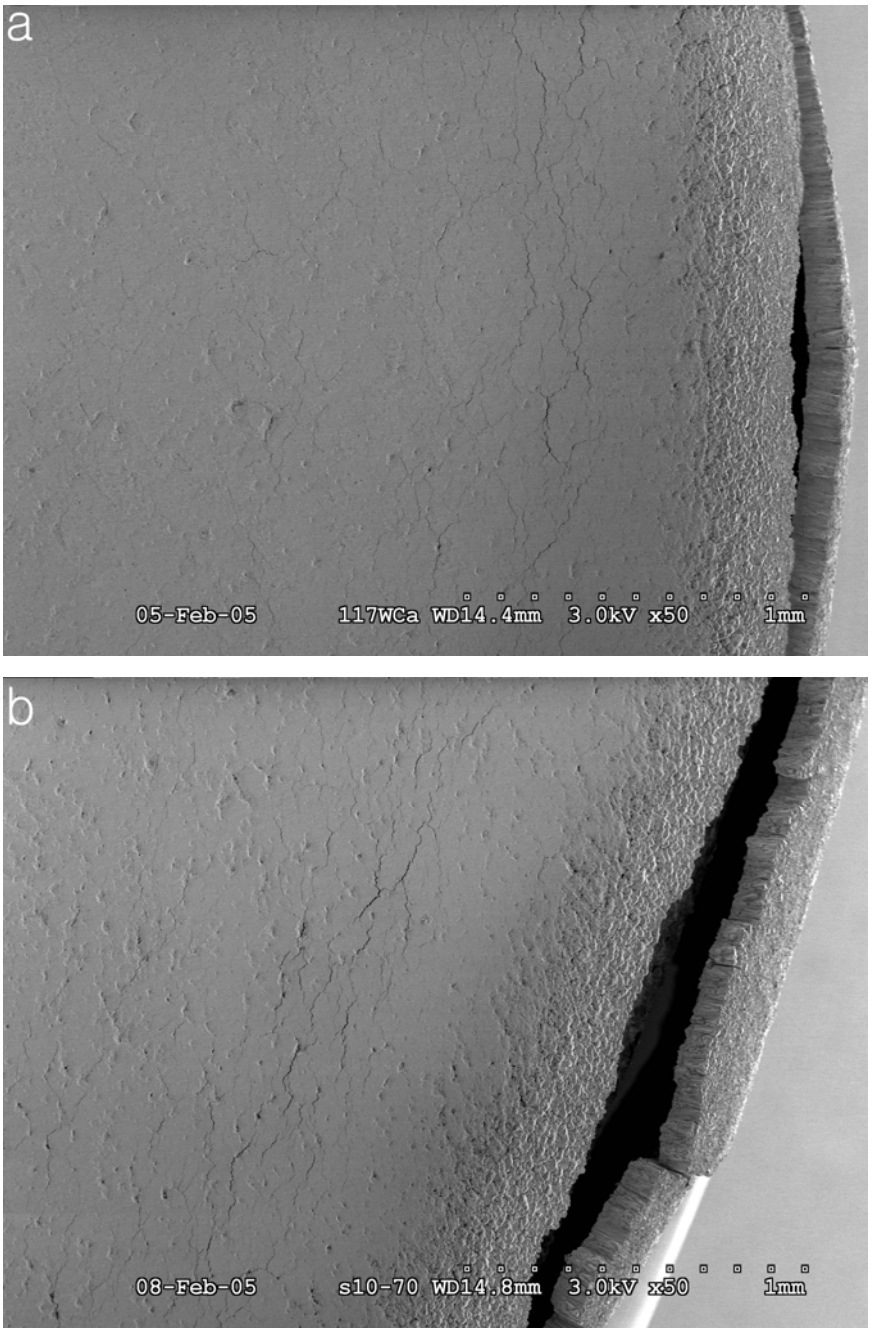

Figure 6.10: Buckling of the 120 μm inner radius cracks after (a) 550 cycles and (b) 634 cycles.

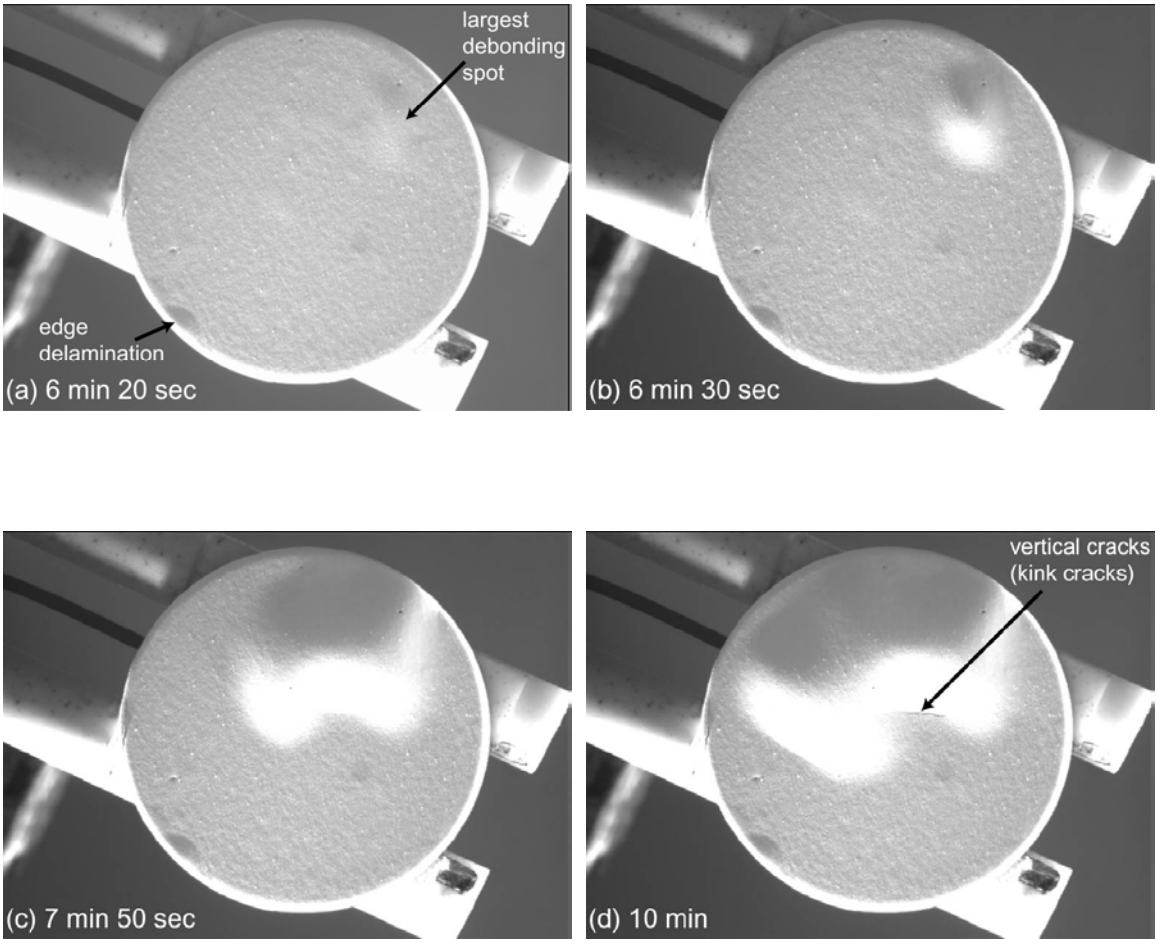

Figure 6.11: Successive AE3 cooling images of spallation with time elapsed after the initiation of the cooling: (a) the largest debonding spot, (b) initiation of the first buckle, (c) first buckle propagation (d) first buckle arrest (e) second buckle progress, and (f) final stage of the buckling failure.

Figure 6.11 continued

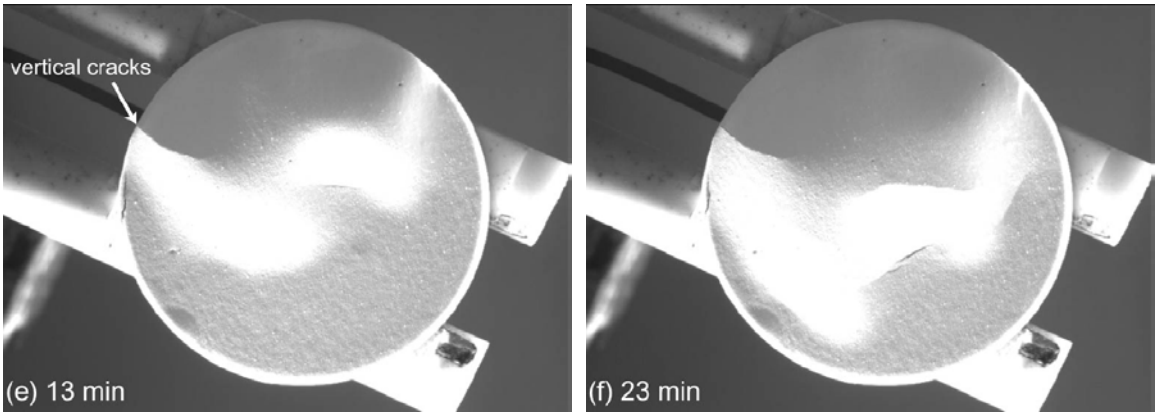

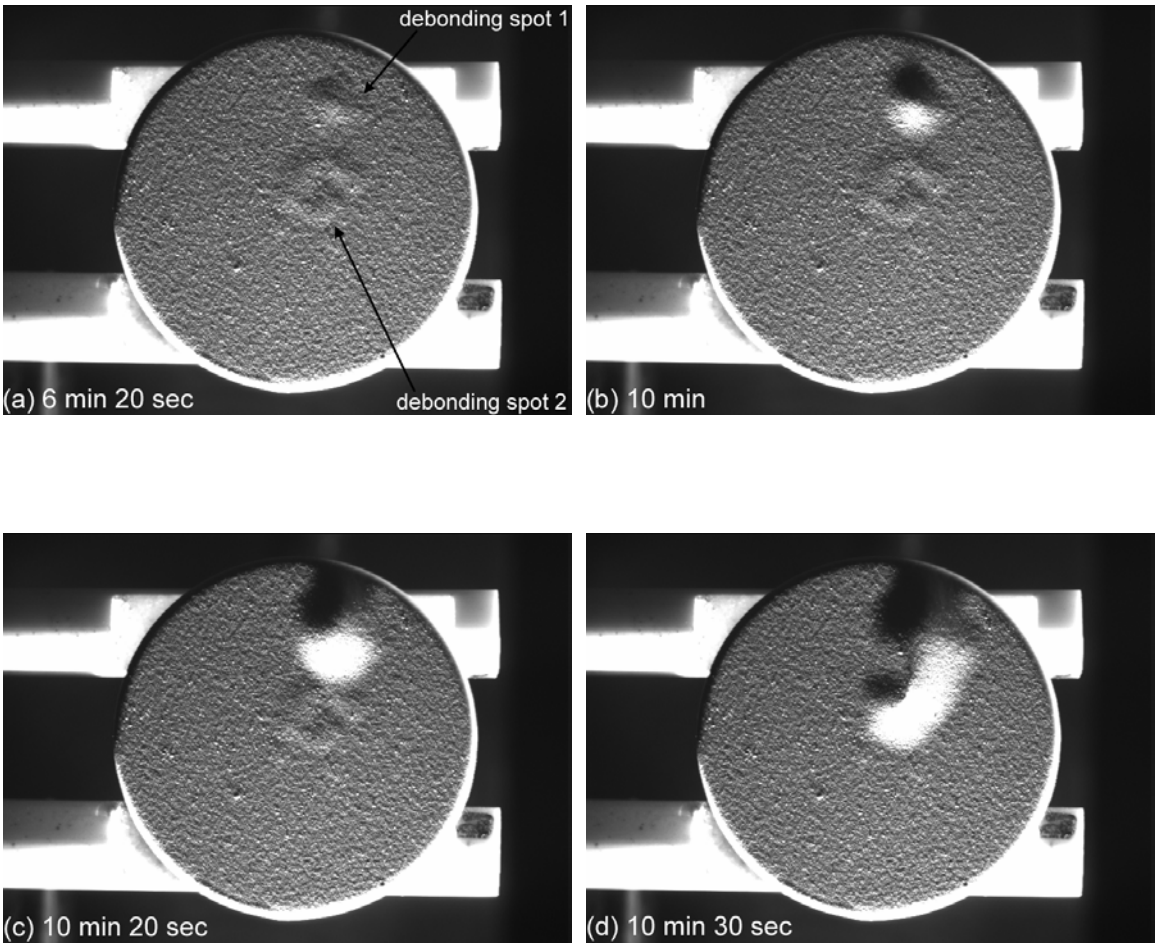

Figure 6.12: Successive N-AE3 cooling images of spallation with time elapsed after the initiation of the cooling: (a) initiation of the first buckle from debonding spot 1, (b) first buckle arrest, (c) first buckle resume (d) connection between the first buckle and the debonding spot 2 (e) completion of creating one debonding spot, and (f) end of the spallation cycle.

Figure 6.12 continued

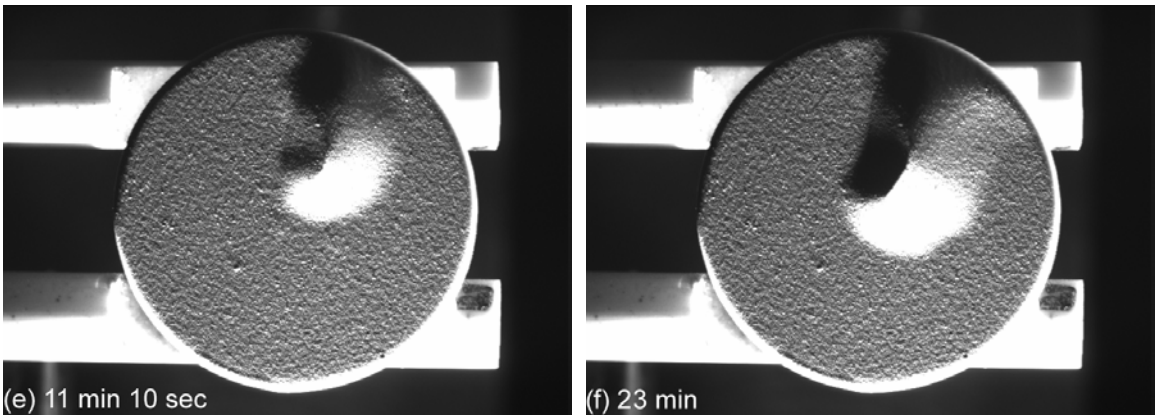

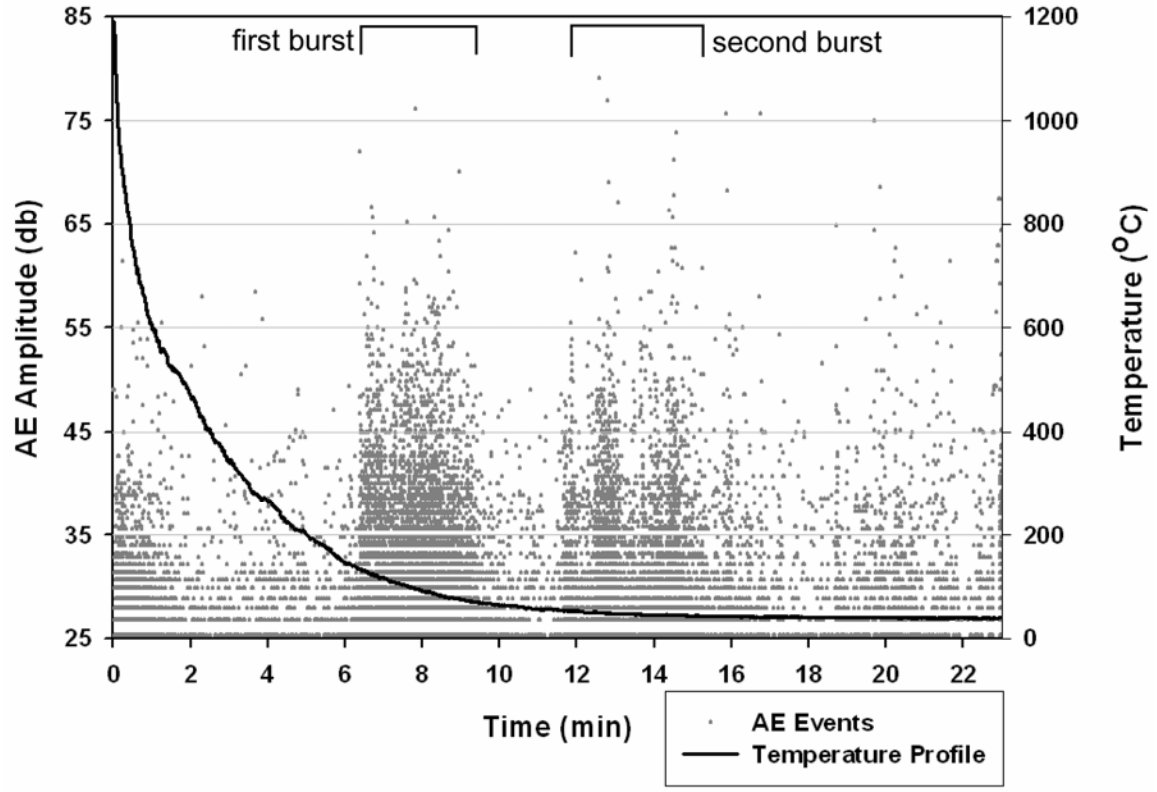

Figure 6.13: AE events during the spallation cooling cycle of the AE3 specimen (See Fig. 6.11).

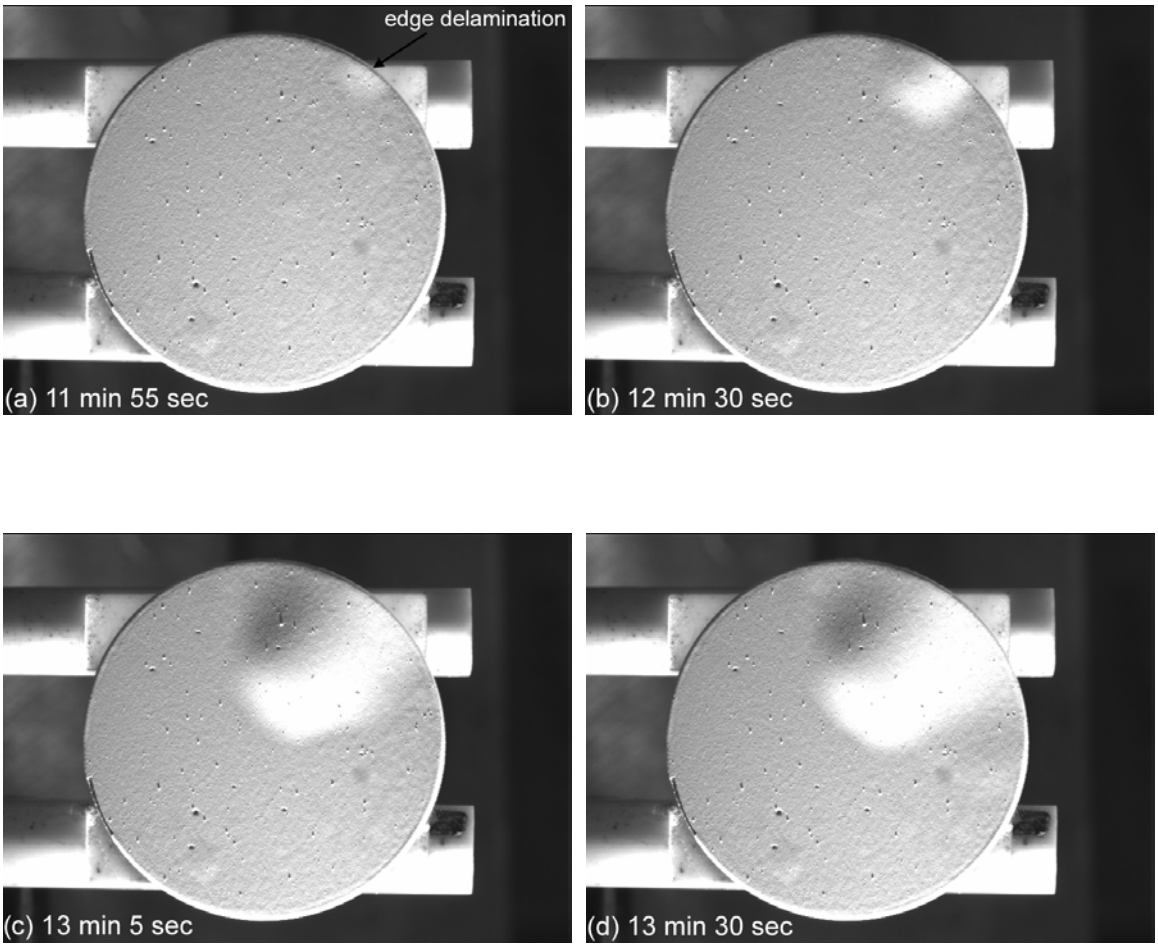

Figure 6.14: Successive N-AE1 cooling images of spallation with time elapsed after the initiation of the cooling: (a) interface crack propagation from the edge delamination spot, (b) initiation of the first buckle, (c) propagation of the first buckle, (d) maximum size of the first buckle, (e) advancing of the delamination, (f) creation of the second buckle, (g) arrest of both buckles and (h) completion of the spallation cycle.

Figure 6.14 continued

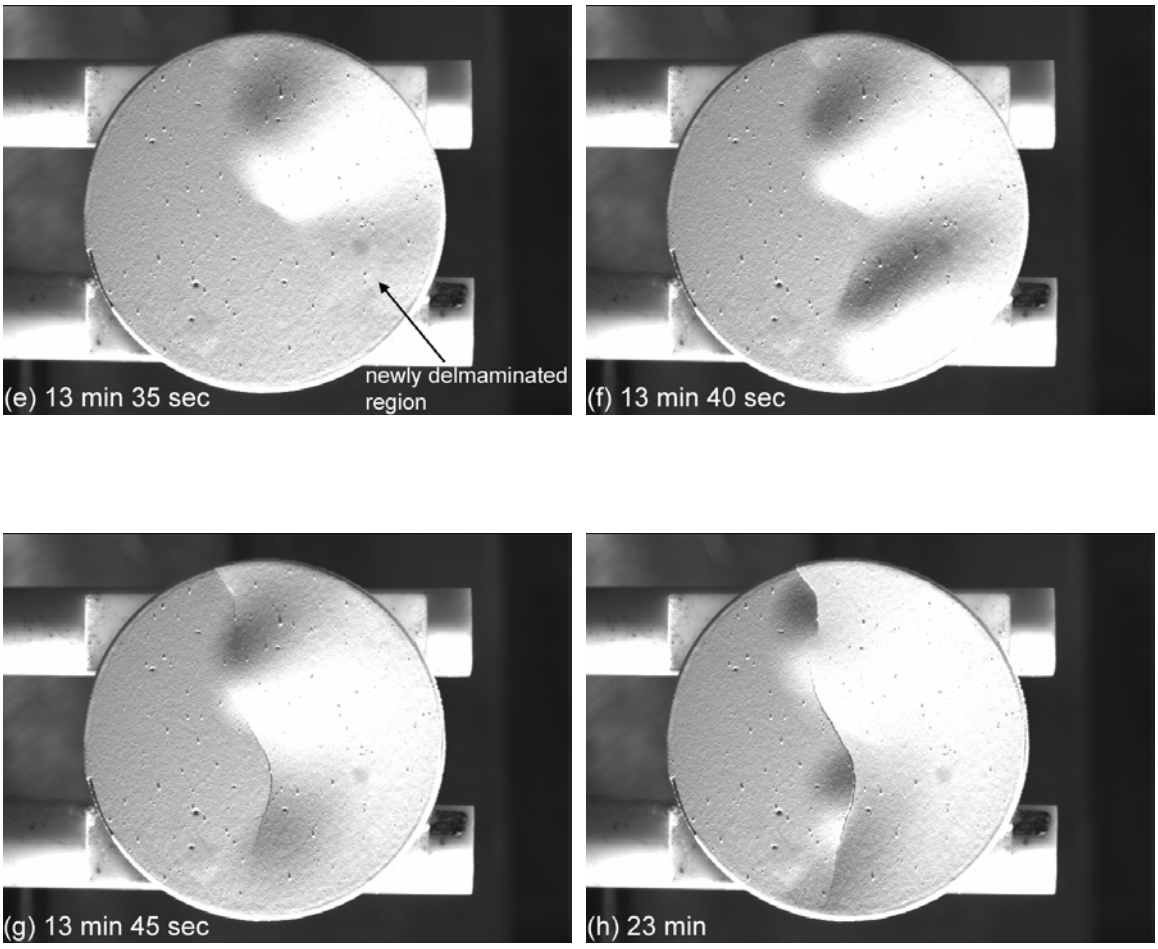

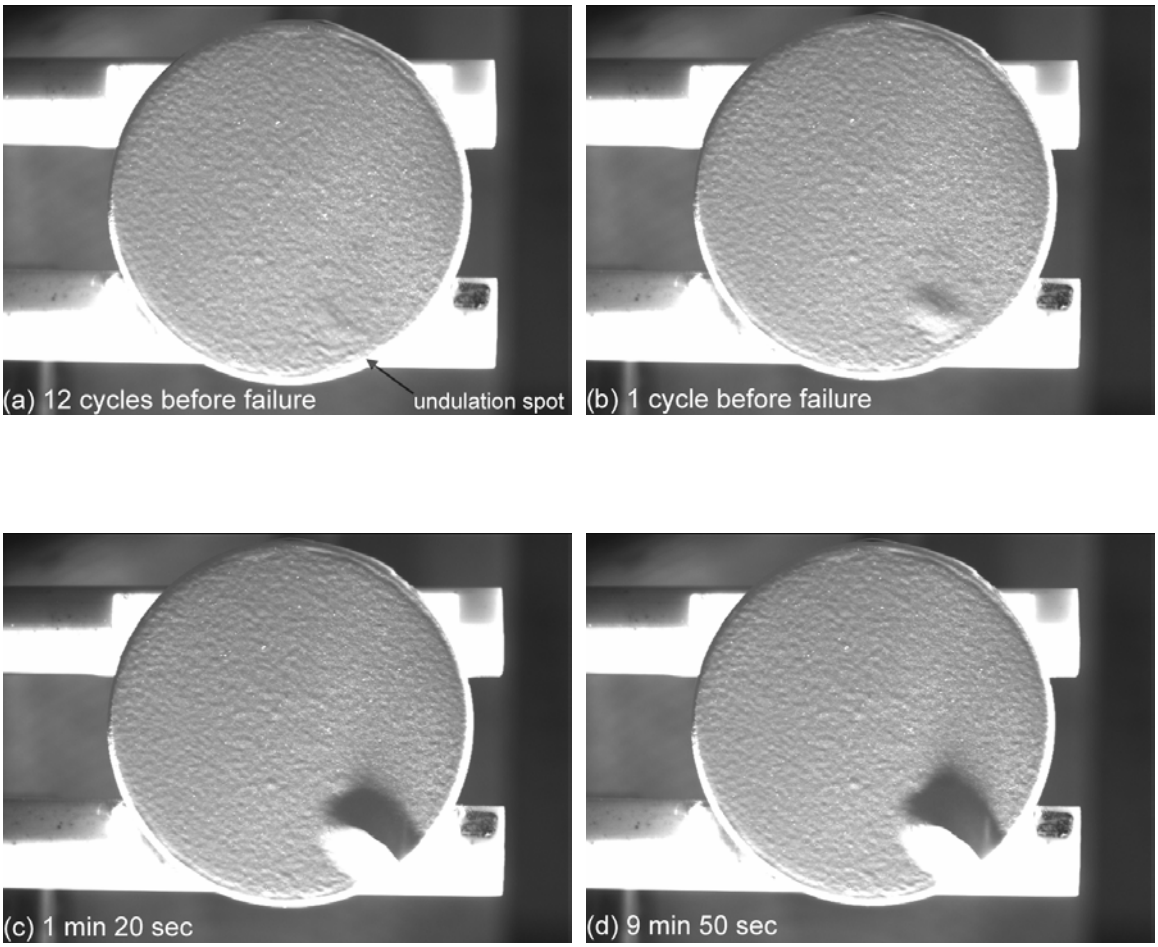

Figure 6.15: Successive P-AE1 cooling images of spallation with time elapsed after the initiation of the cooling: (a) image of 12 cycles before the spallation cycle, (b) last image of 1 cycle before the spallation cycle (c) image of post buckling and edge delamination, (d) initiation of the buckle, (e) buckle arrest and maximum propagation of the buckle, and (f) completion of the buckle with further cycling.

Figure 6.15 continued

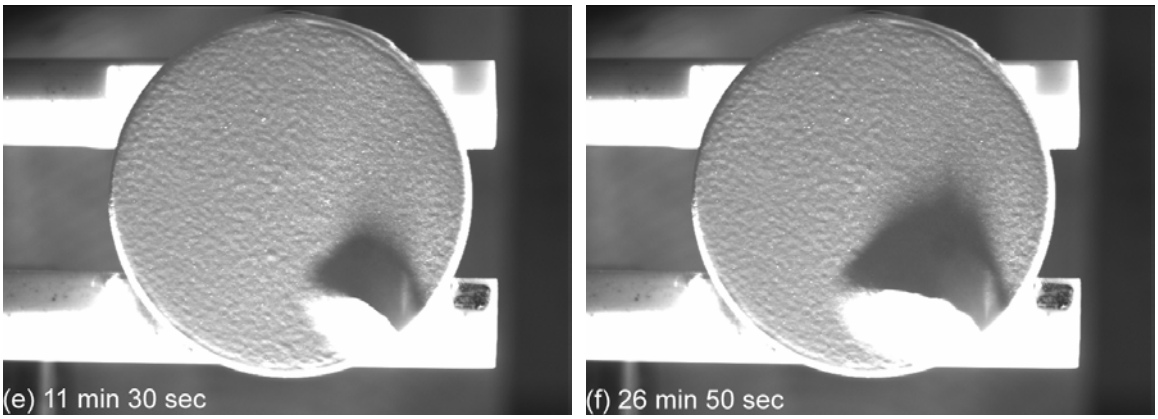

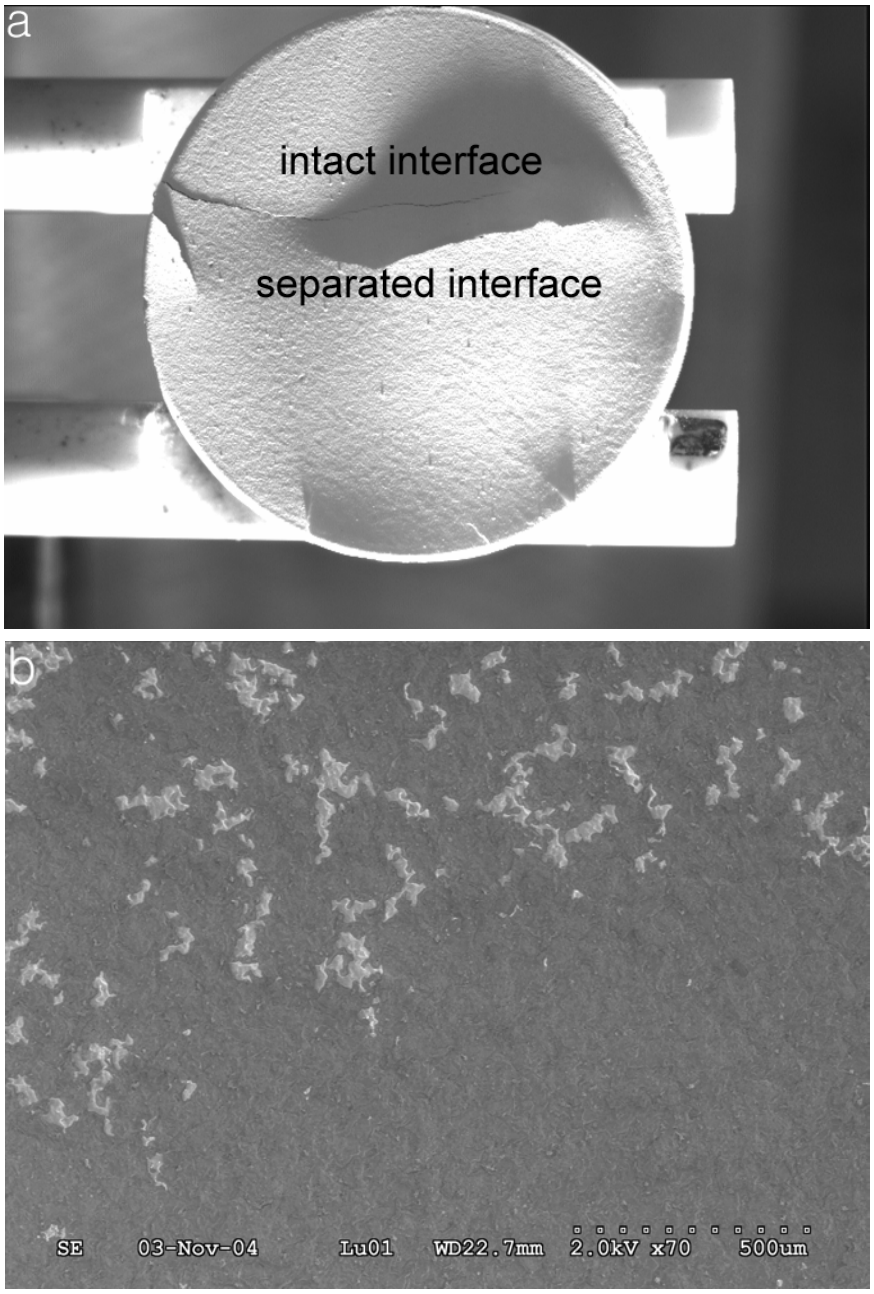

Figure 6.16: Post spallation images of the N-AE2 specimen (a) CCD image with the top coat layer just after the spallation cycle (b) SEM image after complete (including delayed) spallation.

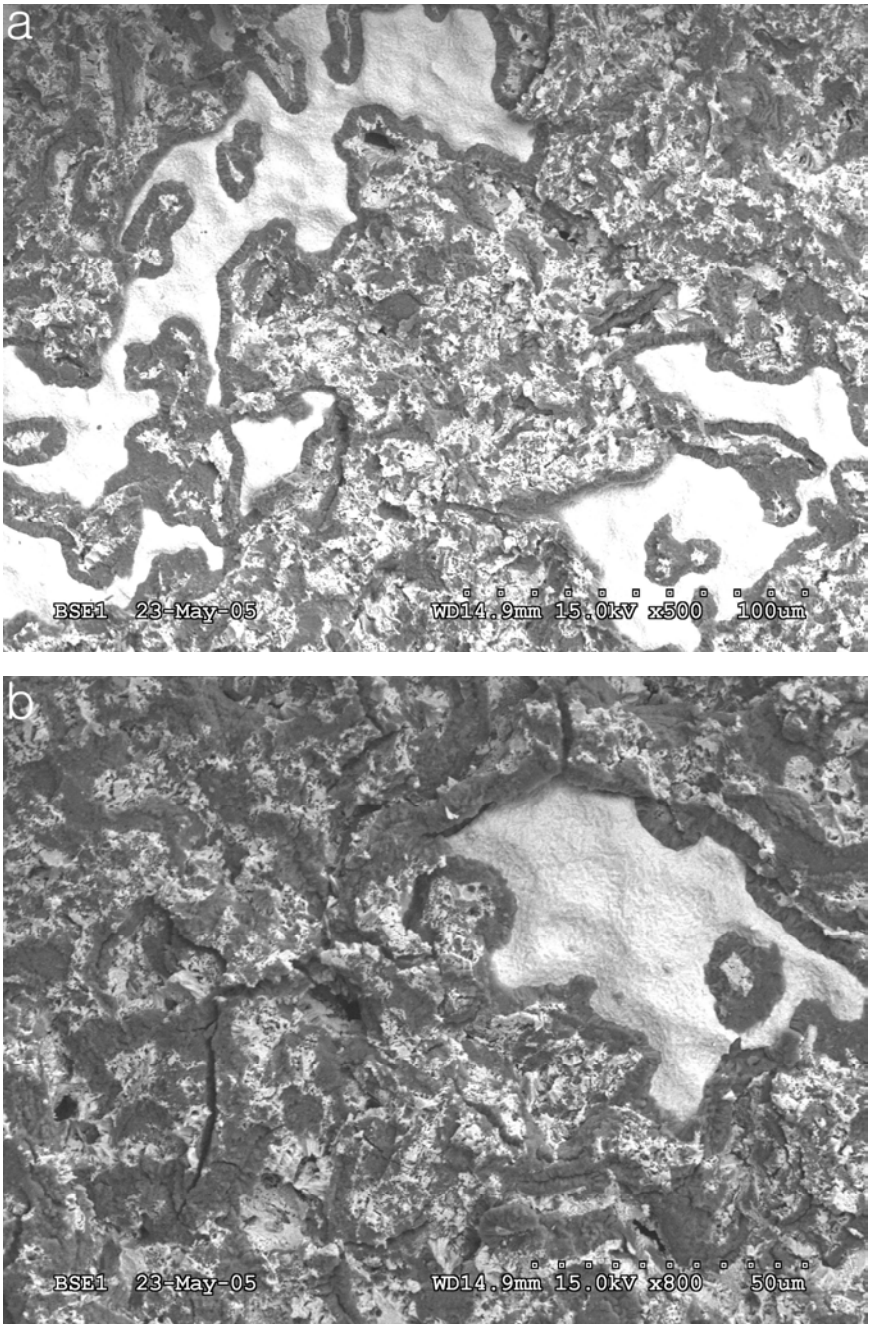

Figure 6.17: Backscattered electron SEM micrographs of post spallation (a) with lower magnification and (b) higher magnification.

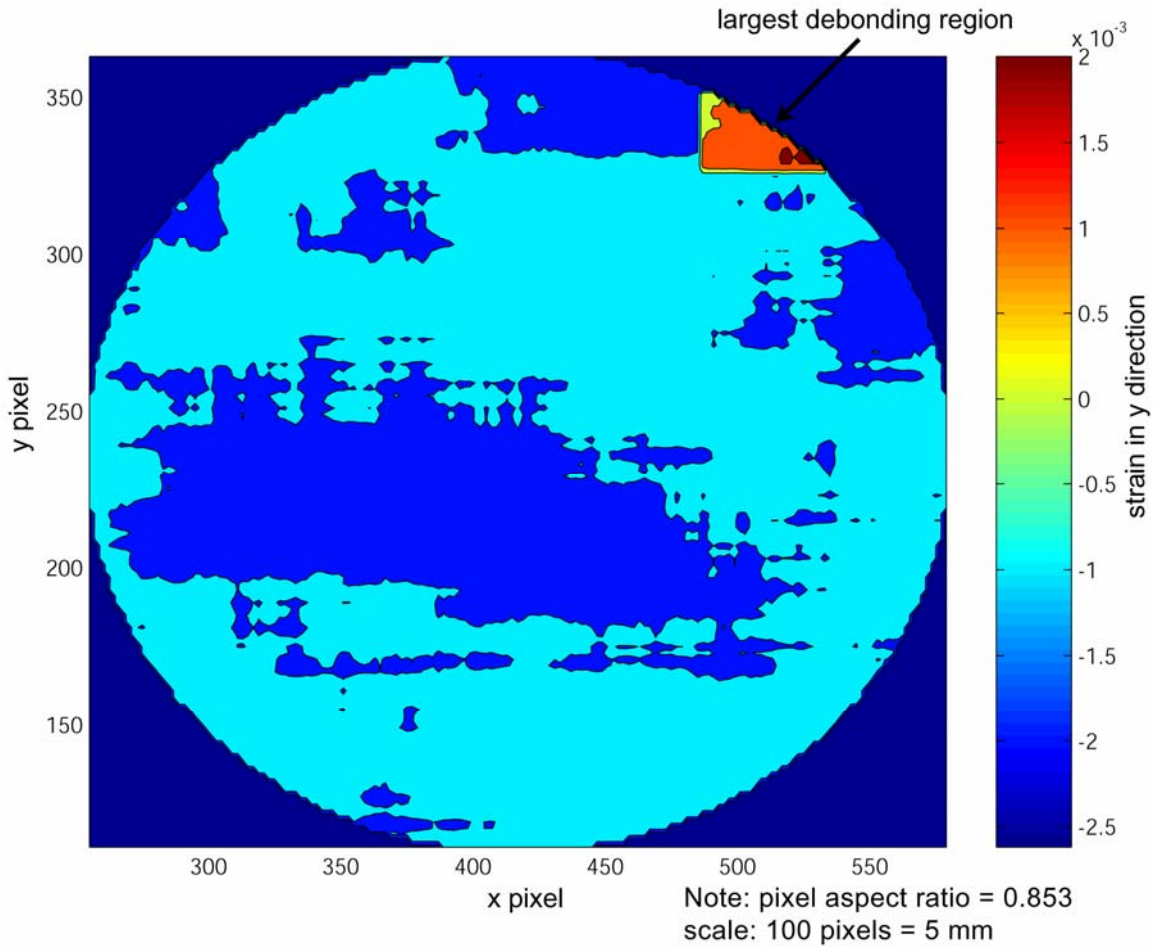

Figure 6.18: The contour map of the DIC y-direction strain calculations on the top coat layer during the cooling from 200 °C to 40 °C.

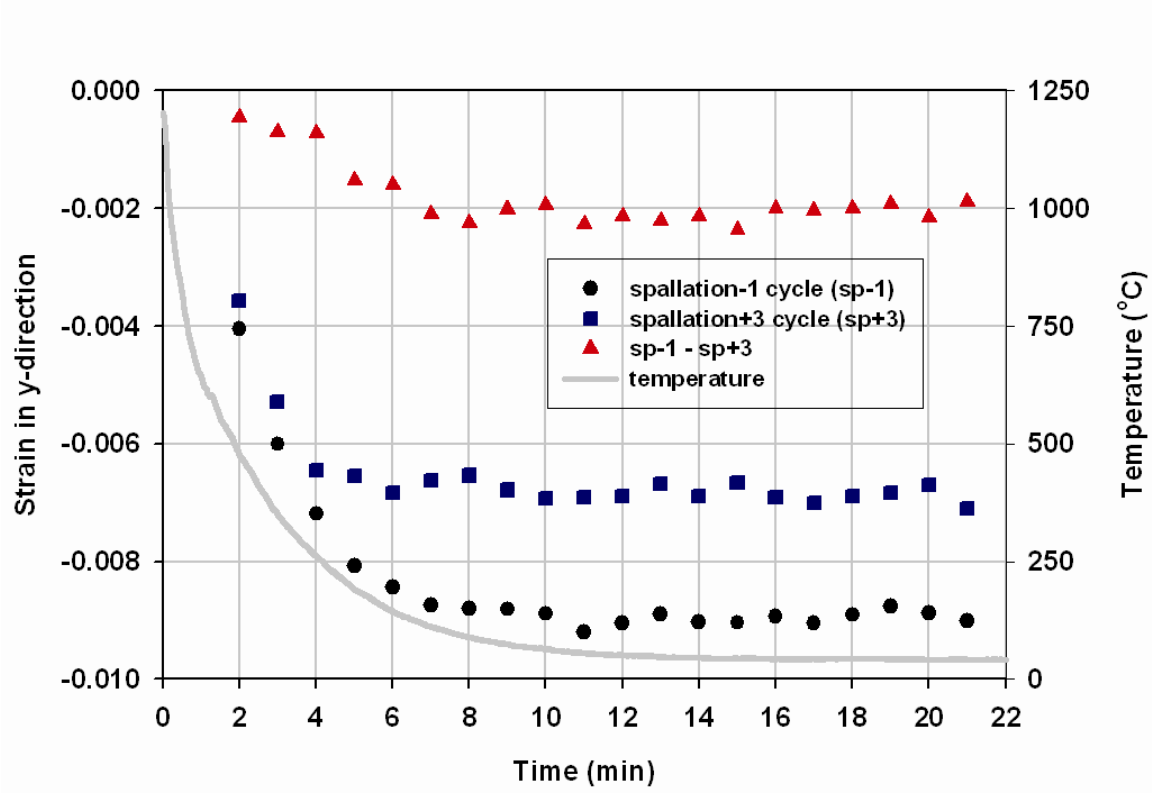

Figure 6.19: Top coat strain due CTE misfit calculated by DIC using the successive top coat images during the cooling cycles from 1200 ºC.

CHAPTER 7

CONCLUSIONS

1. SUMMARY

To better understand and predict thermal barrier coating (TBC) failure, comprehensive research into the mechanisms associated with the loss of TBC durability was performed. In this research cyclic heating to 1200 ºC was applied to TBC buttons with and without the top coat. New apparatus was developed to fully automate rapid cycling. It was found that microstructural evolution of the PtAl (platinum modified aluminide) bond coat, thermally grown oxide (TGO), and substrate depends on the type of thermal exposure and the presence of TGO. The most significant difference between the differently cycled TBC specimens was the amount of γ'-(Ni_3Al) formation. This is important since γ'-(Ni_3Al) is believed to promote TGO waviness during thermal cycling, and TGO waviness is believed to initiate interface cracking. The PtAl bond coat was analyzed by scanning electron microscopy (SEM) and instrumented indentation. From

the cyclic and quasi-isothermal heating test results, it was found that cooling and heating induces stresses that influence microstructural evolution.

The cycling apparatus developed for bond coat only experiments was modified to enable automated collection of acoustic emission (AE) signals. Monitoring AE gave valuable temporal information about damage accumulation in TBCs. It was found that there are 4 distinct regions of AE activity during the life of a TBC. In conjunction with AE data collection, images of the top coat under darkfield-type lighting conditions were collected throughout the cooling portion for every cycle. It was shown that digital image correlation (DIC) can be used to identify regions with interfacial damage. Finally, cycling of an additional specimen was interrupted periodically for analysis with optical profilometry and SEM. The analysis of all the images collected *in situ* and during interrupted experiments made it possible to postulate which failure mechanisms were active in each of the 4 regions with different AE signatures.

Table 7.1 shows the percent of TBC life range for each AE region. The starting points of Regions 3 and 4 match well with the percent life values for initiation of crack nucleation (~34%) and crack extension (~76%) that are given in the literature. It is concluded that Regions 1 and 2 have stable microstructural evolution and damage and the

coating maintains its protective function in these regions. Improving TBC life requires extending Regions 1 and 2. Once a TBC system is in Region 3, unstable damage may form and catastrophic spallation would occur once the damage coalesces. Understanding the damage occurring in Region 3 may help materials scientists and engineers develop ways to extend Regions 1 and 2.

By employing a non-destructive technique to monitor when a TBC system is in Region 3, it would be possible to develop more effective maintenance and replacement schedules. Monitoring AE signals could represent one way to determine when a TBC system is in Region 3. It may also be possible to employ the same DIC techniques used in this dissertation work to actual TBC systems in the field.

2. FUTURE WORK

There are several ways in which the current experiments could be improved. The AE signals were analyzed by the hardware to yield traditional AE results such as hits, counts, amplitude, risetime, *etc*. The hardware currently used also has the ability to capture transient signals which contain the complete signal. This signal could be analyzed for frequency content or it could be compared to other signals. In this way it is

possible to obtain more discriminatory information about AE events, and it might then be possible to quantify the formation of various types of damage.

The DIC technique was successfully used to detect interface delamination. However, TBC sub-critical crack formation/growth detection is still a difficult task. Due to the size of cracks, the spatial resolution is most critical in detecting the cracks. It might be possible to improve upon the current methods by using a camera with more pixels and thereby improving the displacement and strain resolution.

Alternative techniques using thermal imaging to investigate interfacial defects have been attempted. When heat flux from a laser or flash lamp is applied to the substrate side of the TBCs, heat is transferred across interfaces by conduction and/or radiation. The presence of interface cracks alters the heat transmission through the thickness of the TBC specimens appreciably. These thermal conductivity differences between adherent sites and non-adherent sites interfaces result in temperature differences on the ceramic top coat side. The difficulty for most off-the-shelve thermal cameras is again related to the camera's spatial resolution. A better approach would be to use a single infrared sensor that is focused to a point on the specimen together with a high resolution scanning stage. With a very repeatable, flashing heat source (*i.e.*, a laser), it

would be possible to get time dependent temperature profiles at every point on the surface.

Another technique to monitor temperature distributions relies on liquid crystal thermography (LCT). This technique is used to look at defects in microeletronics and should have adequate spatial and temperature resolution to detect the small interface cracks. LCT with the aid of a microscope can provide about 2-4 μm spatial resolution and 0.1 K temperature resolution.

Most of the TBC related maintenance procedures involve "over-engineering" because TBC failure especially in turbine jet engines could lead to catastrophe. Dependable TBC life prediction is essential. The few available life prediction models are based on empirical data with little mechanistic understanding. Due to the brittle nature of the ceramic top coat, the strength of the top coat should be dealt with probabilistically. An existing probabilistic life prediction code, the NASA Ceramic Analysis and Reliability Evaluation of Structures/Life (CARES/Life) could be incorporated with the new mechanistic understanding to predict TBC life. The results found in this dissertation will be utilized to support the simulation.

AE event regions	Region 1	Region 2	Region 3	Region 4
% of TBC life range	0%~19%	19%~32%	32%~75%	75%~100%

Table 7.1: The ranges of percent TBC life for each AE event region.

APPENDIX 1

An illustration of the waveguide rod frame and mechanism is provided in Figure A.1. When the specimen is moving in or out of the furnace and during the heating part of the cycle, the switch trigger closes the switch (Phase 1). During Phase 1, the waveguide rod is positioned about a half a millimeter lower than the bottom of the TBC specimen and the specimen loading rod. After the TBC specimen is driven by the specimen loading rod and positioned above the waveguide rod, voltage is applied to relay to rotate the switch trigger just long enough to open the switch (phase 2). No further voltage is applied to the relay, and the switch trigger rotates until the switch trigger closes the switch at 180º of rotation (phase 3).

Figure A.2 shows the motor and CCD camera control circuit diagram. The circuit is controlled by a Panther motion control system which gives output signals to trigger the DC motor and CCD camera. The Panther controller also controls the specimen loading rod. The Panther system is operated by an indexer program that is directly fed to the serial port using the PC's hyper terminal program. Program 1 gives the

indexer program used in this research. Each line has an address number, command letter, and data input. The first three lines of Program 1 are commands for stepper motor control which drive the specimen in and out of the furnace. The command F is for finding the home position, command W gives the wait time, command J is a "go to" command, and command A reads or writes to a port.

By using command F and W along with two limit switches, complete control of the motion in and out of the furnace (for heating, holding, and cooling) was achieved. The number of cycles was controlled with command J. Automating the acquisition of CCD camera images was made possible by using command A which provides access to the general purpose inputs and two transistor-transistor-logic (TTL) circuits. A special camera cable (IMAQ D100) was used to trigger the CCD camera with TTL signals.

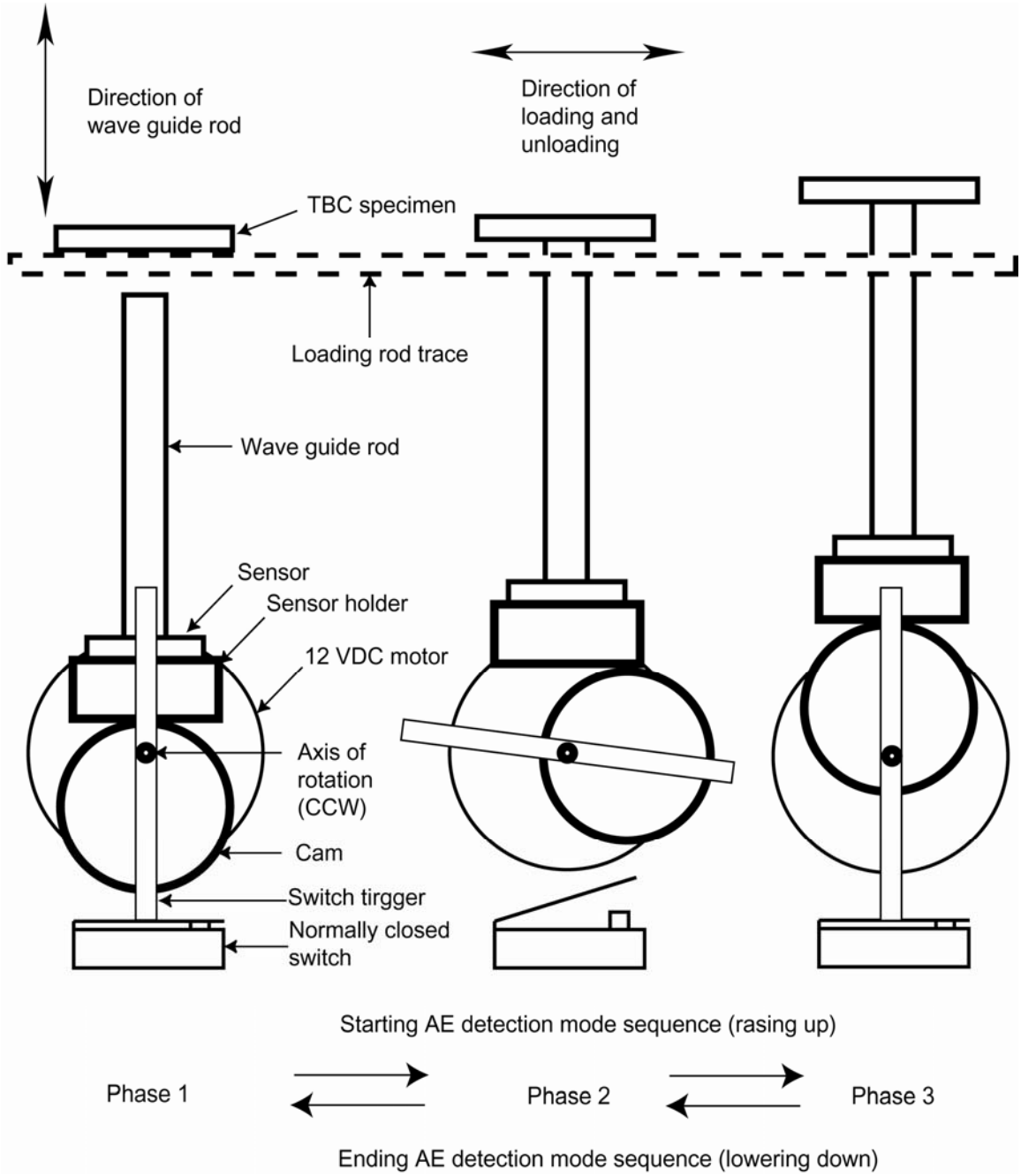

Figure A.1: Schematics of the waveguide rod frame and mechanism. Three positions of the waveguide rod are shown.

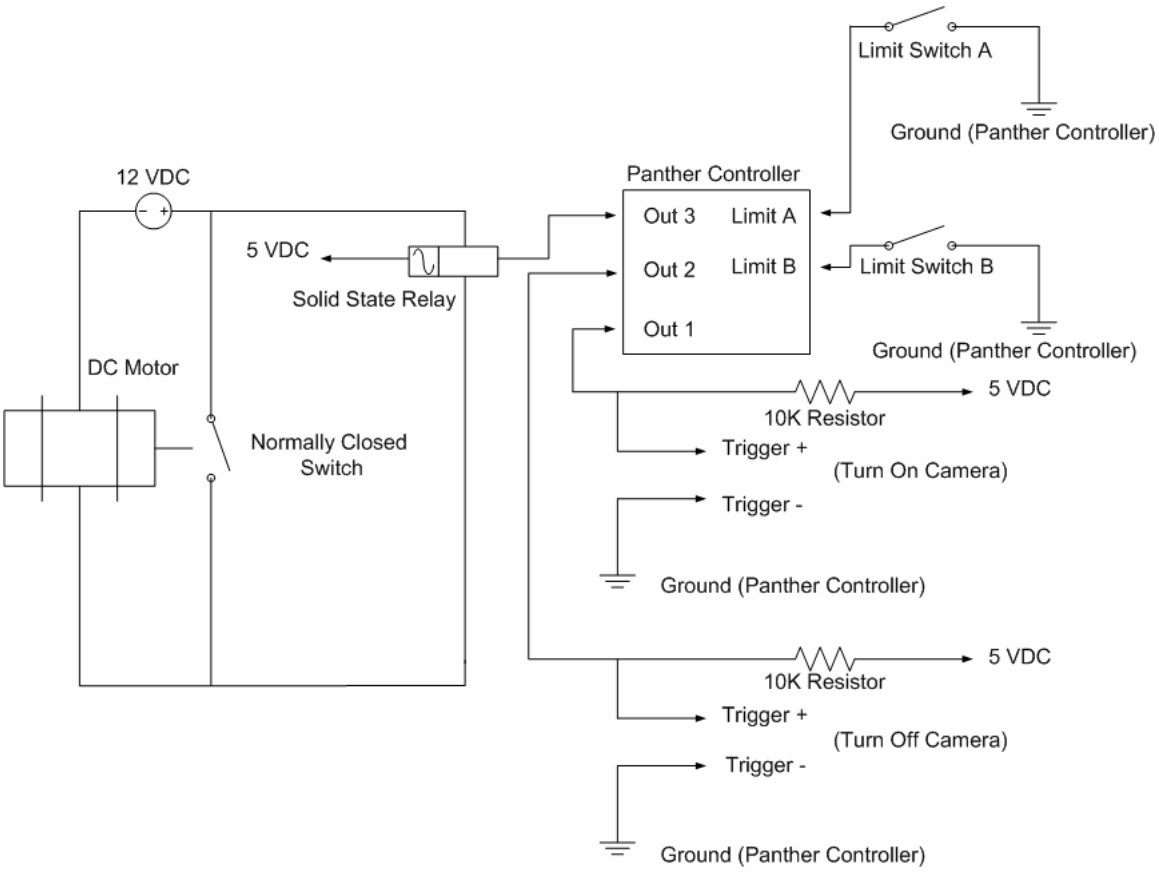

Figure A.2: Schematic of the electronics for the waveguide rod and CCD camera automation. Integration with the Panther motion controller is also shown.

```
0 H       0
2 D       3
4 Y    0  50
7 F    1000 -
10 W      0
13 W     100
16 F    1000 +
19 W      0
22 W   60000
25 W   60000
28 W      0
31 F    1000 -
34 W      0
37 W     100
40 A      8
42 A      0
44 W     100
47 A     32
49 W   60000
52 W   60000
55 W   14000
58 A     16
60 A      0
62 W     100
65 A     32
67 W     100
70 J     16  199
74
```

Program A.1: Hyper terminal indexer program for 200 20 min. heating and 23 min. cooling cycles with automatic CCD camera turn on/off.

BIBLIOGRAPHY

1. **McConnell, V.P., *Aviation maintenance.* Aviation Today, 2001.**
2. **Boss, S. and Demasi-Marcin, J., *Thermal barrier coating experience in gas turbine engines at Pratt & Whitney.* JTTEE5, 1997. 6: p. 99-104.**
3. **Mumm, D.R., Evans, A.G., and Spitsberg, I.T., *Characterization of a cyclic displacement instability for a thermally grown oxide in a thermal barrier system.* Acta Mater., 2001. 49: p. 2329-2340.**
4. **Tolpygo, V.K., Clarke, D.R., and Murphy, K.S., *Oxidation-induced failure of EB-PVD thermal barrier coatings.* Surf. Coat., 2001. 146-147: p. 124-131.**
5. **Miller, R.A., *Thermal barrier coatings for aircraft engines: history and directions.* JTTEE5, 1997. 6(1): p. 35-42.**
6. **Evans, A.G., Mumm, D.R., Hutchinson, J.W., Meier, G.H., and Pettit, F.S., *Mechanism controlling the durability of thermal barrier coatings.* Prog. Mat. Sci., 2001. 46: p. 505-553.**
7. **Maricocchi, A., Bartz, A., and Wortman, D., *PVD TBC experience on GE aircraft engines.* JTTEE5, 1997. 6(2): p. 193-198.**
8. **Reinhlod, E., Botzler, P., and Deus, C., *EB-PVD process management for highly productive zirconia thermal barrier coatings of turbine blades.* Surf. Coat., 1999. 120-121: p. 77-83.**
9. **Meier, S.M. and Gupta, D.K., *The evolution of thermal barrier coatings in gas turbine engine applications.* Journal of engineering for gas turbines and power, 1994. 116: p. 250-257.**
10. **Gell, M., Vaidyanathan, K., Barber, B., Chen, J., and Jordan, E., *Mechanism of spallation in platinum aluminide/electron beam physical vapor-deposition thermal barrier coatings.* Metall and Mater Trans., 1999. 30(A): p. 427-435.**

11. **Busso, E.P., Lin, J., Sakurai, S., and Nakayama, M., *Mechanistic study of oxidation-induced degradation in a plasma-sprayed thermal barrier coating system. part 1: model formulation.* Acta Mater., 2001. 49: p. 1515-1528.**
12. **Xiang, Z.D., Burnell-Gary, J.S., and Datta, P.K., *Aluminide coating formation on nickel-base superalloys by pack cementation process.* J. Mat. Sci., 2001. 36: p. 5673-5682.**
13. **Chen, J.H. and Little, J.A., *Degradation of the platinum aluminide coating on CMSX4 at 1100^{o}C.* Surf. Coat., 1997. 92: p. 69-77.**
14. **Monceau, D., Crabos, F., Malié, A., and Pieraggi, B., *Effect of bond-coat preoxidation and surface finish on isothermal and cyclic oxidation high temperature corrosion and thermal shock resistance of TBC systems.* Material Science Forum, 2001. 369-372: p. 607-614.**
15. **Stiger, M.J., Yanar, N.M., Topping, M.G., Pettit, F.S., and Meier, G.H., *Thermal barrier coatings for the 21st century.* Z. Metallkd., 1999. 90(12): p. 1069-1078.**
16. **Nicholls, J.R., Deakin, M.J., and Rickerby, D.S., *A comparison between the erosion behavior of thermal spray and electron beam physical vapor deposition thermal barrier coatings.* Wear, 1999. 233-235: p. 352-361.**
17. **Chen, X., Wang, R., Yao, N., Evans, A.G., Hutchinson, J.W., and Bruce, R.W., *Foreign object damage in a thermal barrier system: mechanisms and simulations.* Mater. Sci. Eng. A, 2003. 352: p. 221-231.**
18. **Evans, A.G., He, M.Y., and Hutchinson, J.W., *Mechanics-based scaling laws for the durability of thermal barrier coatings.* Prog. Mat. Sci., 2001. 46: p. 249-271.**
19. **Wright, P.K. and Evans, A.G., *Mechanisms governing the performance of thermal barrier coatings.* Current opinion in solid state and material science, 1999. 4: p. 255-265.**
20. **Tolpygo, V.K. and Clarke, D.R., *Surface rumpling of a (Ni, Pt) Al bond coat induced by cyclic oxidation.* Acta Mater., 2000. 48: p. 3283-3293.**
21. **Yanar, N.M., Kim, G., Hamano, S., Pettit, F.S., and Meier, G.H., *Microstructural characterization of the failures of thermal barrier coatings on Ni-base superalloys.* Materials at High Temperatures, 2003. 20(4): p. 459-506.**
22. **Gell, M., Jordan, E., Vaidyanathan, K., McCarron, K., Barber, B., Sohn, Y., and Tolpygo, V.K., *Bond strength, bond stress and spallation mechanisms of thermal barrier coatings.* Surf. Coat., 1999. 120-121: p. 53-60.**

23. **Mumm, D.R. and Evans, A.G., *On the role of imperfections in the failure of a thermal barrier coating made by electron beam deposition.* Acta Mater., 2000. 48: p. 1815-1827.**
24. **Glynn, M.L., Chen, M.W., Ramesh, K.T., and Hemker, K.J., *The influence of a martensitic phase transformation on stress development in thermal barrier coating systems.* METALLURGICAL AND MATERIALS TRANSACTIONS, 2004. 35A(8): p. 2279-2286.**
25. **Chen, M.W., Livi, K.J.T., Wright, P.K., and Hemker, K.J., *Microstructural characterization of a platinum-modified diffusion aluminide bond coat for thermal barrier coatings.* METALLURGICAL AND MATERIALS TRANSACTIONS, 2003. 34A(10): p. 2289-2299.**
26. **Pan, D., Chen, M.W., Wright, P.K., and Hemker, K.J., *Evolution of a diffusion aluminide bond coat for thermal barrier coatings during thermal cycling.* Acta Mater., 2003. 51(8): p. 2205-2217.**
27. **Walter, M.E., Onipede, B., Soboyejo, W., and Mercer, C., *Microstructural features resulting from isothermal and thermocyclic exposure of a thermal barrier coating.* Journal of engineering materials and technology, 2000. 122: p. 333-337.**
28. **Chang, T., Mercer, C., Walter, M.E., and Soboyejo, W.O., *An investigation of the effects of isothermal exposure on microstructural evolution and oxidation in a thermal barrier coating.* DURABLE SURFACES KEY ENGINEERING MATERIALS, 2001. 197: p. 185-198.**
29. **Tomimatsu, T., Zhu, S., and Kagawa, Y., *Effect of thermal exposure on stress distribution in TGO layer of EB-PVD TBC.* Acta Mater., 2003. 51: p. 2397-2405.**
30. **Johnson, C.A., Ruud, J.A., Bruce, R., and Wortman, D., *Relationships between residual stress, microstructure and mechanical properties of electron beam-physical vapor deposition thermal barrier coatings.* Surf. Coat., 1998. 108-109: p. 80-85.**
31. **Tawancy, H.M., Sridhar, N., and Abbas, M., *Comparative performance of selected bond coats in advanced thermal barrier coating systems.* J. Mat. Sci., 2000. 35: p. 3615-3629.**
32. **Holmes, J.W. and McClintock, F.A., *The chemical and mechanical processes of thermal fatigue degradation of an aluminide coating.* Metall Trans., 1990. 21A: p. 1209-1222.**

33. **He, M.Y., Evans, A.G., and Hutchinson, J.W.,** ***The ratcheting of compressed thermally grown thin films on ductile substrates.*** **Acta Mater., 2000. 48(10): p. 2593-2601.**

34. **Chen, M.W., Ott, R.T., Hufnagel, T.C., Wright, P.K., and Hemker, K.J.,** ***Microstructural evolution of platinum modified nickel aluminide bond coat during thermal cycling.*** **Surf. Coat., 2003. 163(25-30).**

35. **Balint, D.S. and Hutchinson, J.W.,** ***An analytical model of rumpling in thermal barrier coatings.*** **JOURNAL OF THE MECHANICS AND PHYSICS OF SOLIDS, 2005. 53(4): p. 949-973.**

36. **Vaidyanathan, K., Gell, M., and Jordan, E.,** ***Mechanisms of spallation of electron beam physical vapor deposited thermal barrier coatings with and without platinum aluminide bond coat ridges.*** **Surf. Coat., 2000. 133-134: p. 28-34.**

37. **He, M.Y., Mumm, D.R., and Evans, A.G.,** ***Criteria for the delamination of thennal barrier coatings: with application to thermal gradients.*** **Surf. Coat., 2004. 185(2-3): p. 184-193.**

38. **Leyens, C., Schulz, U., Pint, B., A., and Wright, I.G.,** ***Influence of electron beam physical vapor deposited thermal barrier coating microstructure on thermal barrier coating system performance under cyclic oxidation conditions.*** **Surf. Coat., 1999. 120-121: p. 68-76.**

39. **Zhu, D. and Miller, R.A.,** ***Thermal conductivity and elastic modulus evolution of thermal barrier coatings under high heat flux conditions.*** **Nasa/tm, 1999. 209069: p. 1-16.**

40. **Matsumoto, M., Yamaguchi, N., and Matsubara, H.,** ***Low thermal conductivity and high temperature stability of ZrO_2-Y_2O_3-La_2O_3 coatings produced by electron beam PVD.*** **Scripta mater., 2003. 50: p. 867-871.**

41. **Lughi, V., Tolpygo, V.K., and Clarke, D.R.,** ***Microstructural aspect of the sintering of thermal barrier coatings.*** **Mater. Sci. Eng. A, 2004. 368: p. 212-221.**

42. **Spitsberg, I.T., Mumm, D.R., and Evans, A.G.,** ***On the failure mechanisms of thermal barrier coatings with diffusion aluminide bond coatings.*** **mater. Sci. Eng. A, 2005. 394(1-2): p. 176-191.**

43. **Xu, T., He, M.Y., and Evans, A.G.,** ***A numerical assessment of the durability of thermal barrier systems that fail by ratcheting of the thermally grown oxide.*** **Acta Mater., 2003. 51: p. 3807-3820.**

44. **Xu, T., He, M.Y., and Evans, A.G., *A numerical assessment of the propagation and coalescence of delamination cracks in thermal barrier systems.* Interface Science, 2003. 11: p. 349-358.**

45. **Hutchinson, J.W. and Evans, A.G., *On the delamination of thermal barrier coatings in a thermal gradient.* Surf. Coat., 2002. 149: p. 179-184.**

46. **Zhu, D., Miller, R.A., Nagaraj, B.A., and Bruce, R.W., *Thermal conductivity of EB-PVD thermal barrier coatings evaluated by a steady-state laser heat flux technique.* Surf. Coat., 2001. 138: p. 1-8.**

47. **Cheng, J., Jordan, E.H., Barber, B., and Gell, M., *Thermal/residual stress in an electron beam physical vapor deposited thermal barrier coating system.* Acta Mater., 1998. 46(16): p. 5839-5850.**

48. **Nissley, D.M., *Thermal barrier coating life modeling in aircraft gas turbine engines.* Journal of Thermal Spray Technology, 1997. 6(1): p. 91-98.**

49. **Nusier, S.Q., Newaz, G.M., and Chaudhury, Z.A., *Experimental and analytical evaluation of damage processes in thermal barrier coatings.* International Journal of solid and structures, 2000. 37: p. 2495-2506.**

50. **Busso, E.P., Lin, J., and Sakurai, S., *A mechanistic study of oxidation-induced degradation in a plasma-sprayed thermal barrier coating system. Part 2: life prediction model.* Acta Mater., 2001. 49: p. 1529-1536.**

51. **DeMasi, J.T., Ortiz, M., and Sheffler, K.D., *Thermal barrier coating life prediction model development.* NASA CR, 1989. 182230.**

52. **Meier, S.M., Nissley, D.M., Sheffler, K.D., and Cruse, T.A., *Thermal barrier coating life prediction model development.* Transactions of the ASME, 1992. 111: p. 258-263.**

53. **Chan, K.S., Cheruvu, N.S., and Leverant, G.R., *Coating life prediction for combustion turbine blades.* Journal of engineering for gas turbines and power, 1999. 121(484-488).**

54. **Yanar, N.M., Stiger, M.J., Maris-Sida, M., Pettit, F.S., and Meier, G.H., *The effect of high temperature exposure on the durability of thermal barrier coatings.* Key Engineering Materials, 2001. 197: p. 145-164.**

55. **Nemeth, N.N., Powers, L.M., Janosik, L.A., and Gyekenyesi, J.P., *Durability evaluation of ceramic components using CARES/LIFE.* Transactions of the ASME, 1996. 118: p. 150-158.**

56. **Doerner, M.F. and Nix, W.D., *A method for interpreting the data from depth-sensing indentation instruments.* J. Mater. Res., 1986. 1(4): p. 601-609.**

57. **Pharr, G.M., Oliver, W.C., and Brotzen, F.R., *On the generality of the relationship among contact stiffness, contact area, and elastic modulus during indentation.* J. Mater. Res., 1992. 7(3): p. 613-617.**

58. **Ellingson, W.A., Rothermel, S.A., and Simpson, J.F., *Nondestructive characterization of ceramic composites used as combustor liners in advanced gas turbines.* Transactions of the ASME, 1996. 118: p. 486-490.**

59. **Ellingson, W.A., Koehl, E.R., Sun, J.G., Deemer, C., Lee, H., and Spohnholtz, T., *Development of nondestructive evaluation methods for hot gas filters.* Materials at High Temperatures, 1999. 16(4): p. 213-218.**

60. **Ferber, M.K., Wereszczak, A.A., Lance, M.J., and Haynes, J.A., *Application of infrared imaging to the study of controlled failure of thermal barrier coatings.* J. Mat. Sci., 2000. 35: p. 2643-2651.**

61. **Chaudhury, Z.A., Newaz, G.M., Nusier, S.Q., Ahmed, T., and Thomas, R.L., *Chronological evaluation of interfacial damage in TBC due to thermal cycling.* J. Mat. Sci., 1999. 34: p. 2475-2481.**

62. **Hellier, C., *Handbook of nondestructive evaluation*. 2001: McGraw-Hill.**

63. **Frommeyer, G. and Wolitz, K., *Schallemissionsanalyse der martensitischen γ Transformation von Fe 30 Ni, Zeits.* Metallkunde, 1980. 71(9): p. 613-616.**

64. **Minozzi, M., Caldarelli, G., Pietronero, L., and Zapperi, S., *Dynamic fracture model for acoustic emission.* The European Physical Journal B, 2003. 36: p. 203-207.**

65. **Stebut, J.v., Lapostolle, F., Bucsa, M., and Vallen, H., *Acoustic emission monitoring of single cracking events and associated damage mechanism analysis in indentation and scratch testing.* Surf. Coat., 1999. 116-119: p. 160-171.**

66. **Kucuk, A., Berndt, C.C., Senturk, U., and Lima, R.S., *Influence of plasma spray parameters on mechanical properties of yttria stabilized zirconia coatings. II: Acoustic emission response.* Mater. Sci. Eng. A, 2000. 284(1-2): p. 41-50.**

67. **Voyer, J., Gitzhofer, F., and Boulos, M.I., *Study of the performance of TBC under thermal cycling conditions using an acoustic emission rig.* JTTEE5, 1998. 7(2): p. 181-190.**

68. **Fu, L., Khor, K.A., Ng, H.W., and Teo, T.N., *Non-destructive evaluation of plasma sprayed functionally graded thermal barrier coatings.* Surf. Coat., 2000. 130: p. 233-239.**

69. **Zhou, Y.C. and Hashida, T., *Thermal fatigue failure induced by delamination in thermal barrier coating.* International Journal of Fatigue, 2002. 24: p. 407-417.**
70. **Freund, L.B. and Suresh, S., *Thin film materials.* 2003.**
71. **Stoney, G.G., *The tension of metallic films deposited by electrolysis.* Proceedings of the Royal Society (London), 1909. A82: p. 172-175.**
72. **Tolpygo, V.K. and Clarke, D.R., *Morphological evolution of thermal barrier coatings induced by cyclic oxidation.* Surf. Coat., 2003. 163-164: p. 81-86.**
73. **Chu, T.C., Ranson, W.F., Sutton, M.A., and Peters, W.H., *Application of digital-image-correlation techniques to experimental mechanics.* Experimental Mechanics, 1985: p. 232-344.**
74. **Lyons, J.S., Liu, J., and Sutton, M.A., *High-temperature deformation measurements using digital-image correlation.* Experimental Mechanics, 1996: p. 64-70.**
75. **Bruck, H.A., McNeill, S.R., Sutton, M.A., and Peters, W.H., *Digital image correlation using Newton-Raphson method of partial differential correlation.* Experimental Mechanics, 1989: p. 261-267.**
76. **Xi, Y., Bergstrom, T.B., and Jennings, H.M., *Image intensity matching technique: Application to the environmental scanning electron microscopy.* Computational Material Science, 1994. 2: p. 249-260.**
77. **Sun, Z., Lyons, J.S., and McNeill, S.R., *Measuring microscopic deformations with digital image correlation.* Optics and Lasers in Engineering, 1997. 27: p. 409-428.**
78. **Vendroux, G. and Knauss, W.G., *Submicron deformation field measurements: Part 2. Improved digital image correlation.* Experimental Mechanics, 1998. 38(2): p. 86-92.**
79. **Field, J.S. and Swain, M.V., *Determining the mechanical properties of small volumes of material from submicrometer spherical indentations.* J. Mater. Res., 1995. 10(1): p. 101-112.**
80. **Swain, M.V., *Mechanical property characterization of small volumes of brittle materials with spherical tipped indenters.* Mater. Sci. Eng. A, 1998. 253: p. 160-166.**
81. **Suresh, S. and Giannakopoulos, A.E., *A new method for estimating residual stresses by instrumented sharp indentation.* Acta Mater., 1998. 46(16): p. 5755-5767.**

82. **Giannakopoulos, A.E. and Suresh, S., *Determination of elastoplastic properties by instrumented sharp indentation.* Scripta mater., 1999. 40(10): p. 1191-1198.**
83. **Venkatesh, T.A., Van Vliet, K.J., Giannakopoulos, A.E., and Suresh, S., *Determination of elasto-plastic properties by instrumented sharp indentation: Guidelines for property extraction.* Scripta mater., 2000. 42: p. 833-839.**
84. **Begley, M.R., Evans, A.G., and Hutchinson, J.W., *Spherical impression of thin elastic films on elastic-plastic substrates.* International Journal of Solids and Structures, 1999. 36: p. 2773-2788.**
85. **Begley, M.R., Mumm, D.R., Evans, A.G., and Hutchinson, J.W., *Analysis of a wedge impression test for measuring the interface toughness between films/coatings and ductile substrates.* Acta Mater., 2000. 48: p. 3211-3220.**
86. **Bressers, J., Arrell, D.J., Ostolaza, K., and Vallés, J.L., *Effect of an aluminide coating on precipitate rafting in superalloys.* Mater. Sci. Eng. A, 1996. 220: p. 147-154.**
87. **Angenete, J. and Stiller, K., *A comparative study of two inward grown Pt modified Al diffusion coatings on a single crystal Ni base superalloy.* Mater. Sci. Eng. A, 2001. 316: p. 182-194.**
88. **Zhang, Y.H., Knowles, D.M., and Withers, P.J., *Microstructural development in Pt-aluminide coating on CMSX-4 superalloy during TMF.* Surf. Coat., 1998. 107: p. 76-83.**
89. **Miracle, D.B., *The physical and mechanical properties of NiAl.* Acta Metall. Mater., 1993. 41(3): p. 649-684.**
90. **Epishin, A., Link, T., Portella, P.D., and Brückner, U., *Evolution of the γ/γ' microstructure during high-temperature creep of a nickel-base superalloy.* Acta Mater., 2000. 48: p. 4169-4117.**
91. **Kamaraj, M., Serin, K., Kolbe, M., and Eggeler, G., *Influence of stress state on the kinetics of γ–channel widening during high temperature and low stress creep of the single crystal superalloy CMSX-4.* Mater. Sci. Eng. A, 2001. 319-321: p. 796-799.**
92. **Véron, M., Bréchet, Y., and Louchet, F., *Directional coarsening of Ni-based superalloys: computer simulation at the mesoscopic level.* Acta Mater., 1996. 44(9): p. 3633-3641.**

93. **Clarke, D.R., Christensen, R.J., and Tolpygo, V.K., *The evolution of oxidation stresses in zirconia thermal barrier coated superalloy leading to spalling failure.* Surf. Coat., 1997. 94-5(1-3): p. 89-93.**

94. **Bhatnagar, H., Ghosh, S., and Walter, M.E., *Parametric studies of failure mechanisms in elastic EB-PVD thermal barrier coatings using FEM.* International Journal of Solids and Structures, 2005.**

95. **Tolpygo, V.K. and Clarke, D.R., *Wrinkling of α-alumina films grown by thermal oxidation-2. Oxide separation and failure.* Acta Mater., 1998. 46(14): p. 5167-5174.**

96. **Christensen, R.J., Lipkin, D.M., Clarke, D.R., and Murphy, K., *Nondestructive evaluation of the oxidation stresses through thermal barrier coatings using Cr^{3+} piezospectroscopy.* Appl. Phys. Lett., 1996. 69(24): p. 3754-3756.**

97. **Sohn, Y., Vaidyanathan, K., Ronski, M., Jordan, E., and Gell, M., *Thermal cycling of EB-PVD/MCrAlY thermal barrier coatings:2. Evolution of photo-stimulated luminescence.* Surf. Coat., 2001. 146-147: p. 102-109.**

98. **Tomimatsu, T., Zhu, S.J., and Kagawa, Y., *Local stress distribution in thermally-grown-oxide layer by near-field optical microscopy.* Scripta mater., 2004. 50: p. 137-141.**

99. **Kesler, O., Matejicek, J., Sampath, S., Suresh, S., Gnaeupel-Herold, T., Brand, P.C., and Prask, H.J., *Measurement of residual stress in plasma-sprayed metallic, ceramic and composite coatings.* Mater. Sci. Eng. A, 1998. 257: p. 215-224.**

100. **Godoy, C., Souza, E.A., Lima, M.M., and Batista, J.C.A., *Correlation between residual stresses and adhesion of plasma sprayed coatings: effects of a post-annealing treatment.* Thin Solid Films, 2002. 420-421: p. 438-445.**

101. **Matejicek, J. and Sampath, S., *In situ measurement of residual stresses and elastic moduli in thermal sprayed coatings Part1: apparatus and analysis.* Acta Mater., 2003. 51: p. 863-872.**

102. **Freborg, A.M., Ferguson, B.L., J., B.W., and Petrus, G.J., *Modeling oxidation induced stresses in thermal barrier coatings.* Mater. Sci. Eng. A, 1998. 245(2): p. 182-190.**

103. **Rosler, J., Baker, M., and Volgmann, M., *Stress state and failure mechanisms of thermal barrier coatings: Role of creep in thermally grown oxide.* Acta Mater., 2001. 49(18): p. 3659-3670.**

104. **Rosler, J., Baker, M., and Aufzug, K., *A parametric study of the stress state of thermal barrier coatings - Part I: creep relaxation.* Acta Mater., 2004. 52(16): p. 4809-4817.**
105. **Baker, M., Rosler, J., and Heinze, G., *A parametric study of the stress state of thermal barrier coatings Part II: cooling stresses.* Acta Mater., 2005. 53(2): p. 469-476.**
106. **Chen, M.W., Glynn, M.L., Ott, R.T., Hufnagel, T.C., and Hemker, K.J., *Characterization and modeling of a martensitic transformation in a platinum modified diffusion aluminide bond coat for thermal barrier coatings.* Acta Mater., 2003. 51(14): p. 4279-4294.**
107. **Water, M.E., Onipede, B., Soboyejo, W., and Mercer, C., *Microstructural features resulting from isothermal and thermocyclic exposure of a thermal barrier coating.* Journal of engineering materials and technology, 2000. 122: p. 333-337.**
108. **Hsueh, C. and Fuller, E., *Residual stresses in thermal barrier coatings: effects of interface asperity curvature/height and oxide thickness.* Mater. Sci. Eng. A, 2000. 283: p. 46-55.**
109. **Newaz, G.M. and Chen, X., *Progressive damage assessment in thermal barrier coatings using thermal wave imaging technique.* Surf. Coat., 2005. 190.**
110. **Scard, P., Leoni, M., Bertamini, L., and Marchese, M., *Residual stress in plasma sprayed Y_2O_3-PSZ coatings on piston heads.* Surf. Coat., 1996. 86(1-3): p. 109-115.**
111. **Li, M.H., Zhang, Z.Y., F., S.X., Guan, H.R., Y., H.W., and Hu, Z.Q., *Oxidation and degradation of EB-PVD thermal-barrier coatings.* OXIDATION OF METALS, 2002. 58(5-6): p. 499-512.**
112. **Agrawal, D.C. and RAJ, R., *Measurement of the ultimate shear-strength of a metal ceramic interface.* Acta Mater., 1989. 37(4): p. 1265-1270.**
113. **Choi, S.R., Hutchinson, J.W., and Evans, A.G., *Delamination of multilayer thermal barrier coatings.* Mechanics of Materials, 1999. 31: p. 431-447.**
114. **He, M.Y., Evans, A.G., and Hutchinson, J.W., *Effects of morphology on the decohesion of compressed thin film.* Mater. Sci. Eng. A, 1998. 245: p. 168-181.**
115. **Kempshall, B.W., Sohn, Y.H., Jha, S.K., Laxman, S., Vanfleet, R.R., and Kimmel, J., *A microstructural observation of near-failure thermal barrier coating: a study by photostimulated luminescence spectroscopy and transmission electron microscopy.* Thin Solid Films, 2004. 466: p. 128-136.**

116. Sridharan, S., Xie, L., Jordan, E.H., Gell, M., and Murphy, K.S., *Damage evolution in an electron beam physical vapor deposition thermal barrier coating as a function of cycle temperature and time.* Mater. Sci. Eng. A, 2005. 393: p. 51-62.